UNIVERSITY OF LONDON THESIS

Degree PhD Year 2007 Name of Author PALGRAVE, Robert

Chemical Vapour Deposition of Nanoparticulate and Nanocomposite Thin Films

This thesis is submitted in partial fulfilment of the requirements for the Degree of Doctor of Philosophy (Chemistry)

Robert Palgrave

UCL

2007

ProQuest LLC
789 East Eisenhower Parkway
P.O. Box 1346
Ann Arbor, MI 48106-1346

I, Robert Palgrave, confirm that the work presented in this thesis is my own. Where information has been derived from other sources, I confirm that this has been indicated in the thesis.

This thesis is dedicated to
Sobia, my Parents and Grandparents

Abstract

Gold nanoparticle and gold / semiconductor nanocomposite thin films have been deposited using aerosol assisted chemical vapour deposition. Two gold precursors have been investigated which would be unsuitable for use with conventional atmospheric pressure chemical vapour deposition. [$HAuCl_4$] was used in methanol solution to deposit films at substrate temperatures of 350 - 500°C. Powder X-ray diffraction and X-ray photoelectron spectroscopy revealed that these films consisted of metallic gold. The optical properties of these films corresponded to nanoscale gold particles, specifically displaying surface plasmon resonance (SPR) absorption. The wavelength of the SPR absorption maximum varied with precursor concentration and substrate temperature from 1000 – 600 nm. Scanning electron microscopy revealed particles a wide variety of sizes and shapes, as well as regions of island growth morphology. Depositions carried out from solutions of [$HAuCl_4$] and a range of quaternary ammonium ion surfactants led to films of particles with narrow size distributions. The use of tetraoctylammonium bromide (TOAB) led to films of spherical particles, the mean diameter of which could be altered by changing [$HAuCl_4$] : TOAB ratio, deposition temperature and solvent volume. Films with mean particle diameters ranging from 65 nm to 120 nm and arithmetic standard deviations of less than 20% of the mean could be deposited in this way. Toluene solutions of pre-formed gold particles were used to deposit films. These films showed similar optical properties to the original precursor solution. Nanocomposite films were deposited by combining [$HAuCl_4$] or pre-formed gold particles with a conventional CVD precursor in a single precursor solution. [$W(CO)_6$], [$Mo(CO)_6$], [$W(OPh)_6$], [$Ti(O^iPr)_4$] were combined with a gold precursor to deposit metal oxide films with incorporated gold particles. The concentration of gold within the films could be varied by changing the precursor ratios. These films showed SPR peaks that were redshifted compared to gold particles alone.

Acknowledgements

I would like to thank my supervisor, Professor Ivan Parkin, for his encouragement, guidance and advice, and for the opportunities he has given me over the past five years, especially for allowing me to go my own way with this project. Thank you. I am also grateful to Dr. Claire Carmalt, my secondary supervisor, for all her assistance.

I also wish to thank all of the students and postdocs whose time on the third floor of the Christopher Ingold building coincided with mine: those who showed me the ropes, Drs. Chris Blackman, Graham Shaw, Troy Manning, Emily Peters, Russell Binions and Shane O'Neill, those who travelled with me to strange lands, Drs. Jalpa Patel, Siama Basharat, Clara Piccirillo and Miss Uzma Qureshi, those who did *real* chemistry, Drs. Abul Ali, Dina Solanki, Christina Baskaran, Jesus Gil-Tomas, Mr. Stephen Potts and Miss. Caroline Knapp, and those who'll still be messing around with nanoparticles after I leave, Sig. Paolo Melgari, Miss Naima Narband, Miss Gill Walters, and Mr. Kris Page. I would especially like to thank Dr. Geoff Hyett and Dr. Simon Naisbitt for many useful discussions, and Mr. Zahi Sulaiman, Miss Victoria Lees, Mrs. Clare Bishop, Miss Amy Dee, Miss Ayo Afonja for their friendship.

I am, of course, indebted to the staff of the chemistry (and archaeology) departments without whom nothing at all would get done, least of all this thesis. Most especially: Messrs. Kevin Reeves, Dave Knapp, Joe Nolan, Dave Ladd, Dave Morphett, Dick Waymark and Dr. Steve Firth.

In the last four years I have spent many hours demonstrating in the undergraduate labs – I'd like to thank all those who I worked with who helped the time to pass pleasurably, especially Professor Tony Deeming, Professor Paul McMillan, Dr. Graeme Hogarth, Dr. Andrea Sella, Mr. Phil Hayes and Mr. Crosby Medley.

To my parents, who have supported me in every way: I could not have done this, or anything, without you.

Finally, I thank Sobia, for everything. This thesis is for you.

Table of Contents

List of Abbreviations

AACVD	Aerosol assisted chemical vapour deposition
acac	Acetyl acetonate
APCVD	Atmospheric pressure chemical vapour deposition
CTAB	Cetyltrimethyl ammonium bromide
CPS	Counts per second
CVD	Chemical vapour deposition
DSC	Differential scanning calorimetry
hfac	Hexafluoro acetyl acetonate
FWHM	Full width at half maximum
^{i}Pr	Isopropyl
IR	Infra red
LACVD	Laser assisted chemical vapour deposition
Ph	Phenyl
RF	Radio frequency
SEM	Scanning electron microscopy
TEAB	Tetraethyl ammonium bromide
TGA	Thermal gravimetric analysis
TOAB	Tetraoctyl ammonium bromide
UV	Ultraviolet
XRD	X-Ray diffraction
XPS	X-Ray photoelectron spectroscopy

List of Figures

Chapter 1: Introduction

Chapter 2: Experimental Section

Chapter 3: Deposition of Gold Films

Chapter 4: Deposition of Nanocomposite Films

List of Tables

Chapter 1: Introduction

Chapter 3: Deposition of Gold Films

Chapter 4: Deposition of Nanocomposite Films

Chapter 1: Introduction

1.1 General Introduction and Aims

This thesis presents the results of an investigation into the chemical vapour deposition (CVD) of metallic gold containing films from novel precursors. Thin gold films are important technologically in a variety of areas. Because of their chemical inertness and high conductivity, they are used as conducting layers in microelectronics, especially as contacts and interconnects.[1] Other properties emerge in nanostructured gold films, for example, size dependent optical absorption,[2] catalysis,[3] and enhancement of the Raman effect.[4, 5] Because these properties are dependent on the size of the gold particles, deposition of gold films with controllable nanostructures is desirable, both as an industrial technique and to further the understanding of these nanoscale phenomena. This is one of the principle aims of the work presented here. In order to achieve control over the nanostructure of CVD gold films, methodology was borrowed from solution phase gold nanoparticle synthesis, specifically the use of size and shape directing surfactants. The optical properties of thin gold films are of great research interest, especially the link between film structure and optical properties. It is also a goal of the project to investigate the relationship between structure and optical properties of the gold films produced.

Chemical vapour deposition is an important technique for depositing thin films. CVD proceeds by diffusion of a gas phase precursor to the substrate, where a chemical reaction occurs forming a film.[6] The specific variant of CVD used in this work is aerosol assisted CVD (AACVD). The intricacies of this technique will be discussed elsewhere in this chapter, but the principle difference between AACVD and other CVD techniques is the use of a liquid aerosol to transport the precursor to the substrate. This has the important effect of changing the precursor requirements: volatility is not necessary for AACVD precursors. It is an aim of this work to identify and investigate new AACVD precursors which are involatile, and so unsuitable for conventional CVD, yet result in useful films with desirable properties. In this regard, two involatile gold precursors have been investigated: [$HAuCl_4$] and pre-formed gold nanoparticles. In some significant ways these new precursors are superior to presently used gold CVD precursors.

Nanocomposite materials consist of two or more phases, at least one of which has dimensions on the nano-scale, which is often defined as 1 – 100 nm.[7] Gold nanoparticles encased in a semiconductor matrix are an example of a nanostructured material that has been investigated intensively. They are of interest as encasing in a semiconductor is a convenient way of immobilising gold nanoparticles, which may be necessary for their use in solid state devices. Incorporation of gold particles can also enhance catalysis and chromic properties of the semiconductor matrix. Gold / transition metal oxide nanocomposites have been produced in this work by single step CVD processes, utilising the precursors developed for the deposition of gold films. The methods developed to deposit gold films by CVD were extended to produce nanocomposite films in a single step.

In this introductory chapter, the process of CVD and the properties of gold nanoparticles and films will be discussed. Previous reports of the deposition of gold films by CVD will be reviewed, followed by a discussion of gold / semiconductor nanocomposite films and their deposition.

1.2 Principles of Chemical Vapour Deposition

CVD is the deposition of a solid film from the gas phase via a chemical reaction.[8] It is the chemical reaction that distinguishes CVD from other deposition mechanisms such as evaporation, sputtering and vapour transport, which are examples of physical vapour deposition (PVD). All types of CVD involve three basic processes: introduction of precursor to the gas stream, transport of precursor to the substrate and application of energy to cause a reaction. A wide range of deposition techniques fall under the definition of CVD, and these differ in one or more of the following parameters:

- **Pressure.** CVD can be carried out at atmospheric pressure of under reduced pressure.
- **Precursor activation.** The chemical reaction of the precursors can be initiated by heat, light, RF plasma or another method.
- **Number of precursors.** Depositions can be made from a single precursor or multiple precursors (single, dual or multiple source CVD).

- **Precursor transport.** The precursor can be introduced to the gas phase by thermal vapourisation, liquid injection or through aerosol formation.
- **Type of reactor.** The reactor where the deposition takes place may be hot wall, or cold wall, and have a horizontal, vertical or rotating substrate.

The depositions reported in this thesis have been carried out at atmospheric pressure, using a heated substrate in a reactor with unheated walls (a cold wall reactor). A liquid aerosol was used to transport the precursors to the substrate, and depositions were carried out using single and multiple precursors.

Figure 1.1 shows a schematic of a horizontal bed cold wall CVD reactor, which is the type of reactor used in this work. The substrate lies horizontally on top of a heater. Gas enters the reactor and flows parallel to the substrate. At some point within the reactor, precursors react and form a film on the substrate.

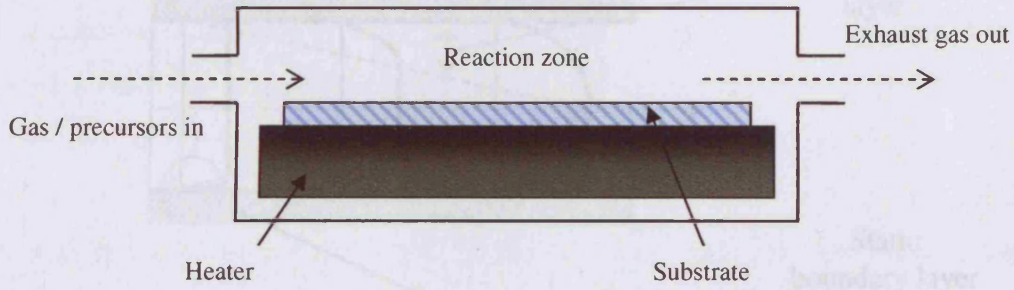

Figure 1.1 A schematic of a horizontal bed cold wall CVD reactor.

Since only the substrate is directly heated, a temperature gradient will exist in a cold wall reactor. This has implications for precursor behaviour and will be discussed later in this chapter.

1.2.1 Fluid Dynamics

The behaviour of a gas in motion is described by the equations of fluid dynamics. The motion of gas is an important consideration in CVD as it dictates the transport of reactants to the substrate.[8] The Reynolds number (R_e) is a ratio of forces often used to characterise a fluid flow through a pipe. The dimensionless Reynolds number is defined as:

$$R_e = \rho v L / \mu \qquad (1.1)$$

In equation 1.1, ρ = fluid density, v = mean fluid velocity, L = characteristic length of the pipe (typically the pipe diameter) and μ = fluid viscosity.[8] Two flow regimes can be defined: laminar and turbulent flow. In the laminar flow regime, the fluid flows in layers parallel to the direction of flow; in this regime, lateral motion within the fluid occurs only through diffusion. In contrast, turbulent flow is characterised by large scale vortices and eddies that cause significant lateral mixing of the fluid. Low values of R_e, caused by low density, low velocity, small pipe diameter or high fluid viscosity result in laminar flow, while high values of R_e result in turbulent flow. The low densities of the carrier gases and the relatively low flow rates used in most forms of CVD mean that the flow is laminar.

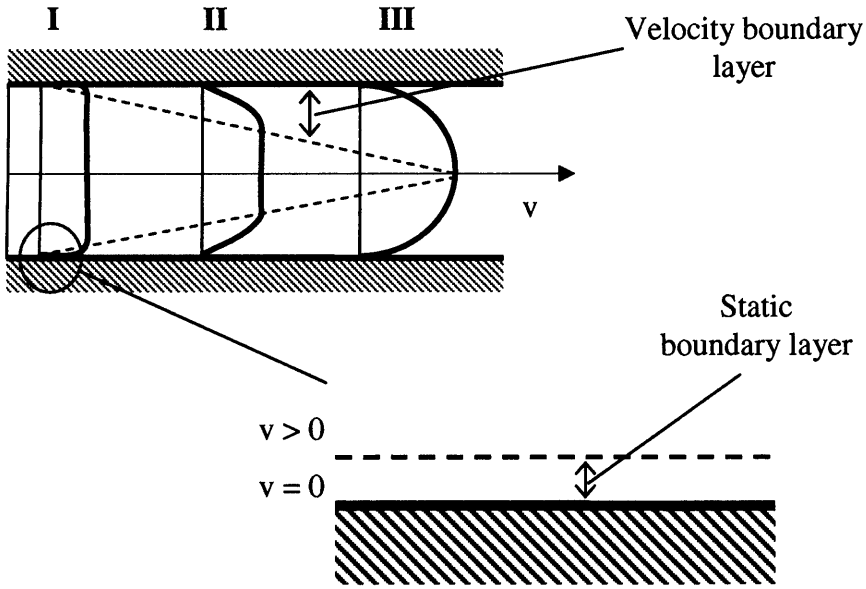

Figure 1.2. Velocity profiles of gas in a laminar flow along a two dimensional pipe. The expanded section shows the static boundary layer next to the pipe wall.[8,9]

Figure 1.2 shows the velocity profile of a gas under laminar flow conditions. The gas enters the pipe at the left of the diagram with a constant velocity profile. Loss of momentum due to collisions with the stationary walls causes the velocity of the gas to decrease. The velocity of the layer of gas directly in contact with the walls is assumed to be zero; this stationary layer is known as the static boundary layer.[9] The layers of gas

above the static layer are also progressively slowed, and the velocity profile becomes less uniform: profile II (figure 1.2) has a central core of uniform velocity, but profile III has no uniform portion. A profile such as III in figure 1.2 is known as fully developed laminar flow. A second boundary layer can be defined between regions of uniform and non-uniform fluid velocity, and is shown by dashed lines in figure 1.2. This velocity boundary layer vanishes at III, although the static boundary layer remains throughout.

1.2.2 Particles within the Reactor

Within the CVD reactor, particles may be present in the gas flow. These may be solid particles present due to gas phase reaction of precursors, or the solid particles themselves may be the precursor. Aerosol droplets, which are essentially suspended liquid particles, are a feature of AACVD. Some specific aspects of liquid particles are discussed further in section 1.3. In general, gas phase particles are subject to a number of forces within the reactor.

Thermophoresis, also known as the Soret effect or thermal diffusion, is a force acting on particles (and also molecules) suspended in a fluid in the presence of a temperature gradient.[9-13] The force can be regarded as arising from non-uniform bombardment of the particle by fluid molecules; this bombardment will be greater on the 'hot' side of the particle, therefore this force is usually found to repel particles from a hotter surface and attract them to a colder surface; the term 'thermophobic force' is used. However, under certain conditions, thermophoresis can act in the opposite direction, driving particles towards a hot surface; this is known as 'thermophilic force'.[14] The switch between thermophobic and thermophilic behaviour is not well understood. One factor that seems to be important is particle concentration. At very high particle concentrations, interactions between particles influence the thermophoretic effect, in some cases causing thermophilic movement of particles.[15, 16] However, it is expected that at lower particle concentrations, as may be found in the gas phase of a CVD reactor, the thermophoretic effect will be thermophobic.

The thermophoretic force is generally dependent on the size of the particle; larger particles experience larger forces.[17] In cold wall CVD reactors, thermophoresis acts to prevent large solid particles being incorporated into the film, increasing film homogeneity and adherence. However, it has been shown that for nano-sized particles

(diameter 50 nm and below) the magnitude of the thermophoretic force depends only very weakly on particle size.[9]

The second force to be considered is diffusion. Particle movement in a fluid, also known as Brownian motion, is an essentially random movement of particles due to instantaneously asymmetric bombardment by the molecules that constitute the fluid. Brownian motion is a significant consideration for nanoparticles suspended in a gas stream.[18] The particle diffusivity in a gas, D, can be expressed as:[9]

$$D = \frac{CkT}{d_p \mu} \tag{1.2}$$

In equation 1.2, k is Boltzmann's constant, T is the absolute temperature, d_p is the particle diameter and μ is the gas viscosity. C is a factor which depends on pressure, and will be approximately constant at pressures close to atmospheric pressure. It can be seen from the above equation that particle diffusion is higher for smaller particles and at higher temperatures.

Particles near to the substrate (or other reactor surface) may experience additional forces. Van der Waals force will be attractive between particle and surface. There may also be Columbic attraction or repulsion, depending whether the particle and surface are charged. Additionally, gas phase particles may be attracted to or repelled from particles already adsorbed onto the substrate, either electrostatically or due to steric factors.[18] Steric repulsion may be caused by capping groups attached to either particle. Figure 1.3 summarises the forces discussed in this section.

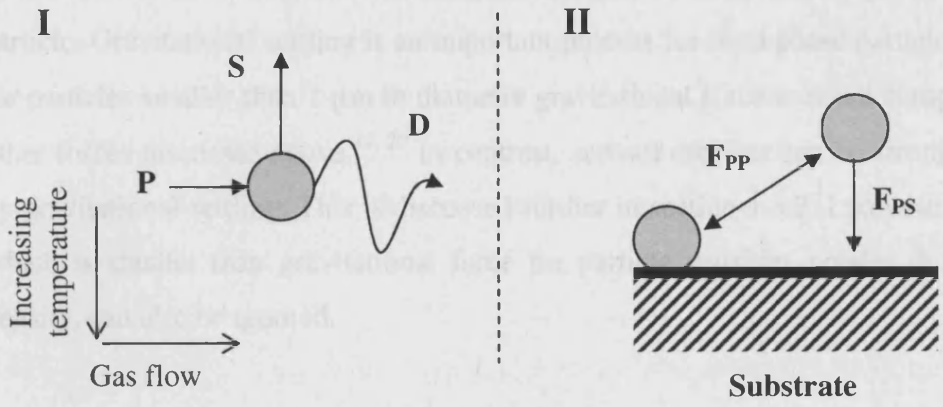

Figure 1.3. Forces acting on particles suspended in the gas phase in a cold wall CVD reactor. Panel I illustrates a particle far from the substrate, and panel II shows a particle close to the substrate. For clarity, the forces shown in panel I are omitted from panel II, although these forces still apply. S is the Soret (thermophoretic) effect acting as the expected thermophobic force, D is diffusion (Brownian motion) and acts in a random direction and varies with time. P is the force due to the flow of gas. F_{PP} is the attractive or repulsive force between two particles. F_{PS} is the attractive force between the particle and the substrate. Some other forces are not shown; see text for details.

As seen in figure 1.3, panel I, when a particle is far from the substrate, the only force that directs it towards the substrate in the laminar flow regime is diffusion. Equation 1.2 shows that diffusion is greater for smaller particles. Additionally the thermophoretic effect, which directs particles away from the hot substrate, is smaller for small particles (although the size dependence is weak for nano-sized particles). Thus smaller particles are more likely to be directed against the temperature gradient and towards the substrate in a cold wall CVD reactor. Close to the substrate (figure 1.3, panel II) there is attraction between the particle and substrate through van der Waals interactions, although the thermophoretic effect will be greater due to a greater temperature gradient close to the substrate. The force between gas phase and adsorbed particles can be attractive or repulsive. In the case of an attractive interparticle force, the resulting film is expected to be composed of aggregates of particles. In the case of a repulsive force, the film will consist of widely spaced particles. At high levels of coverage, these two types of film will become indistinguishable, as the entire substrate will be covered, and spacing between particles will not be measurable.

In addition to the forces shown in figure 1.3, gravity and buoyancy will act on the particle. Gravitational settling is an important process for fluid phase particles, although for particles smaller than 1 μm in diameter gravitational force is small compared to the other forces discussed above.[19, 20] In contrast, aerosol droplets can be strongly affected by gravitational settling. This is discussed further in section 1.3.2. Likewise, buoyancy, which is smaller than gravitational force for particle densities greater than the fluid density, can also be ignored.

In summary, deposition of nanoparticles onto a substrate is governed by competition between the thermophoretic effect, which is expected to be thermophobic, and particle diffusion.[21] Since diffusion is greater and thermophoresis is smaller when the particle diameter is small, it is expected that small particles will migrate to the substrate faster than large particles. Since diffusion is a random process, it is as likely to direct the particles upwards away from the substrate as towards it. Therefore, even in the case where diffusion is much greater than thermophoresis and in an infinitely long two dimensional reactor, a statistical limit of 50% of the gas phase particles will migrate to the substrate. In practical cases, where thermophoresis is significant, the reactor is finite in length, and migration to the reactor walls is possible, the proportion of gas phase particles that reach the substrate will be much lower.

1.2.3 Molecular Precursors within the Reactor

Molecular precursors undergo essentially the same forces as descried for gas phase particles in the previous section. However, the thermophoretic effect is very small for gas phase molecules,[17] and gravitational settling is negligible. In contrast, diffusion is much more rapid for molecular precursors compared to large gas phase particles. This leaves diffusion as the main driving force behind lateral movement (*i.e.* perpendicular to the direction of gas flow) of molecular precursors in the CVD reactor. The increased diffusion and decreased thermophobic force means that in general molecular precursors reach the substrate more quickly than larger particles.

It was originally assumed that molecular precursors arrived at the substrate individually, and that the film was deposited atom by atom. Crystalline films were thought to grow when adsorbed precursors had enough surface mobility to locate low energy sites, thus building the crystal lattice. Recently it has been suggested that formation of gas phase

charged clusters may play a significant role in film formation from molecular precursors.[22, 23] It is thought that charged clusters form around ionized gas molecules which are produced at the hot substrate surface. Charged clusters have been detected in several CVD and PVD processes, including the deposition of gold films by thermal evaporation, where 2 nm diameter positively charged clusters were collected from the gas phase.[22]

Molecular precursors may react in the gas phase to produce large solid particles,[21, 24, 25] the subsequent behaviour of which is described above. Molecular precursors may also react to form intermediate species, which themselves go on to form the film. In this way, the formation of the film may be a multi-step process.[26] Figure 1.4 summarises the molecular processes discussed.

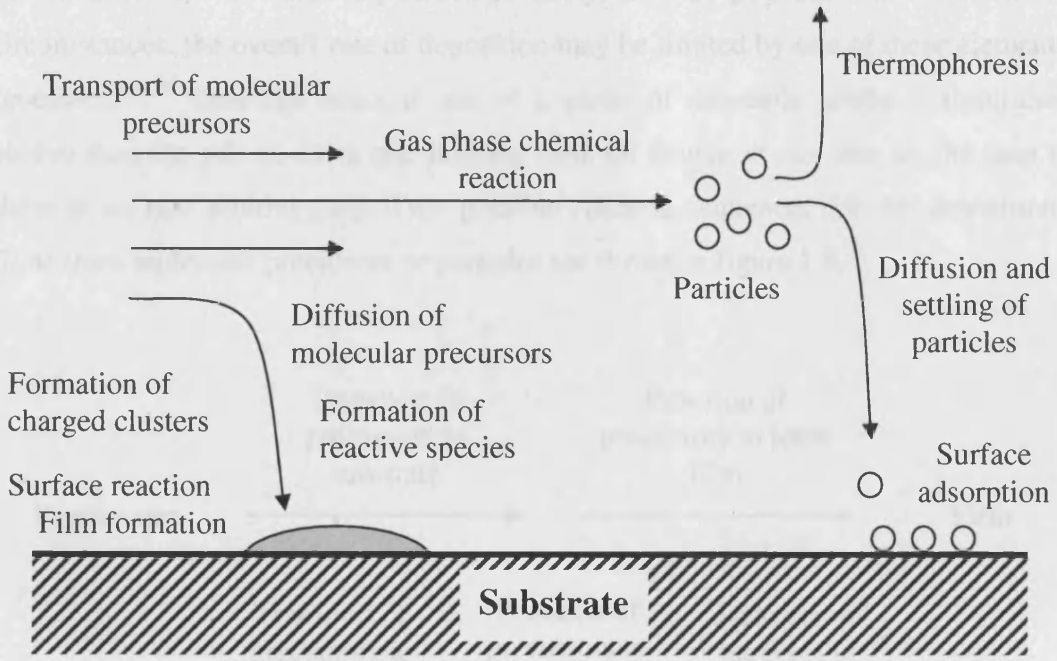

Figure 1.4. Molecular precursor processes within the CVD reactor.

1.2.4 Simultaneous Particle / Vapour Deposition

Simultaneous deposition of a film from gas phase particles and vapour phase molecular precursors has been studied as a way of increasing the deposition rate in CVD (sometimes called particle assisted CVD).[19, 24, 27, 28] In some cases a hot wall reactor is

used with the substrate at a slightly lower temperature, allowing thermophoresis to drive particle deposition onto the substrate.[27]

1.2.5 CVD Reaction Kinetics

CVD is a non-equilibrium process; it is controlled by mass transport and irreversible surface and gas phase reactions, rather than an equilibrium process, where the system comes to thermodynamic equilibrium over time.[8, 26] The rate of a CVD deposition is an important characteristic, which can provide insight into mechanism and determine usefulness for industrial applications. Clearly, in CVD the deposition process is not an elementary reaction; kinetically, it can be said that CVD is a complex process which is a combination of several sequential and possibly concurrent elementary reactions and transport processes. Determination of these elementary processes and their rate constants for a real world deposition is rarely, if ever, possible. However, in some circumstances, the overall rate of deposition may be limited by one of these elementary processes.[26, 29] This can occur if one of a series of sequential steps is significantly slower than the others, *i.e.* a rate limiting step. Of course, it can also be the case that there is no rate limiting step. Two possible reaction sequences for the deposition of films from molecular precursors or particles are shown in figure 1.5.

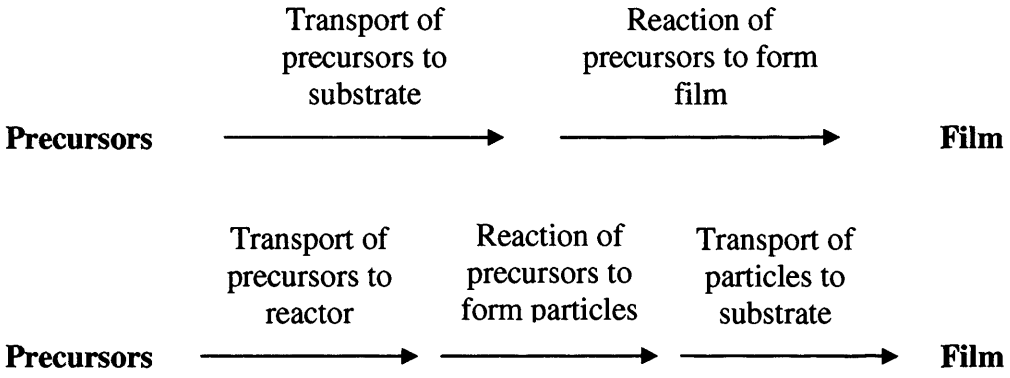

Figure 1.5. Steps in the deposition of CVD films.

CVD reactions are sometimes characterised as transport limited or reaction limited. This is illustrated by the top scheme in figure 1.5, which shows transport and reaction as the two main steps in the deposition. The lower scheme shows steps in the deposition of a film through gas phase particle nucleation and subsequent particle migration to the

substrate. As discussed above, the diffusion of nanoparticles to the precursor will be slower than diffusion of molecular precursors, due to the effects of thermophoresis and the slower diffusion of large particles. It is expected, therefore that deposition of particles will be slower than deposition from molecular precursors, especially if there is also an additional gas phase particle formation step.

Kinetics of precursor transport

As already discussed, transport of molecular precursors to the substrate is driven by diffusion. The rate of diffusion across a concentration gradient is given by Fick's Law:[30]

$$J = -D\frac{dC}{dx} \tag{1.3}$$

In equation 1.3, J is the precursor flux, or the rate of precursor transport. D is the diffusivity constant, C is the precursor concentration, and x is the distance, therefore dC/dx is the concentration gradient. The negative sign shows that the diffusion is from a point of high concentration to a point of low concentration. Figure 1.6 shows the precursor concentration gradient present close to the substrate in a CVD reactor. Assuming rapid, irreversible adsorption and reaction of the precursor at the substrate surface, in other words, that the desorption rate from the surface is zero, then the concentration of gas phase precursor at the substrate will be zero. The concentration in the bulk gas phase, [A], will be a finite value dependent on the concentration of precursor used, the flow rate, distance along the reactor and other parameters. There will be a concentration gradient between the bulk gas phase and the substrate surface, *i.e.* there exists a concentration boundary layer, analogous to the velocity boundary layer discussed in section 1.2.1.

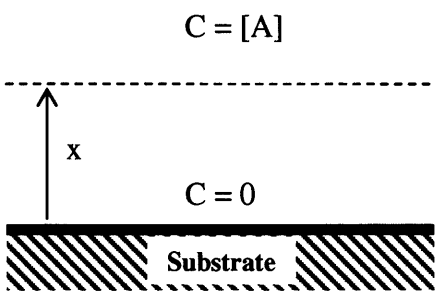

Figure 1.6. Precursor concentration gradient above the substrate in a CVD reactor.

The flux of precursor molecules across the concentration boundary layer is given by equation 1.3. The concentration gradient shown in figure 1.6 is given by:

$$\frac{dC}{dx} = 0 - [A] = -[A] \qquad (1.4)$$

Substituting into equation 1.3 gives the rate equation for diffusion across the boundary layer:

$$J = D[A] \qquad (1.5)$$

This is a first order rate equation with respect to [A], and the rate constant is the temperature dependent diffusion coefficient. Therefore the diffusion of molecular precursors is a first order process, and if the diffusion is the rate limiting step, then the deposition as a whole will be first order with respect to the precursor concentration. As a first order process, the gas phase precursor concentration, [A], will decrease exponentially with time. Therefore in a diffusion limited deposition, the deposition rate will decrease exponentially along the length of the reactor.

Kinetics of precursor surface reactions

The kinetics of precursor surface reactions is more difficult to generalise. Rates of absorption and desorption of gas phase precursors, surface migration and surface reaction may all be significant. A kinetic treatment of these processes is possible, although it usually requires *in situ* measurements taken during the deposition.[31] Since

this type of analysis was not performed in this work, it is not possible to accurately adapt kinetic models to the surface reactions of the depositions reported here.

1.3 Aerosol Assisted CVD

Aerosol assisted CVD is a variant of CVD in which the precursor is transported to the substrate by an aerosol mist. The precursor can either be dissolved in a solvent, from which an aerosol is formed, or the precursor can be a liquid. Within this definition a further division is sometimes made between spray pyrolysis and 'true' AACVD; this will be discussed later in the section. An aerosol can be generated from a solution or liquid precursor by ultrasonic atomisation or spraying through a nozzle. Because of the method of transport used, and in contrast to almost all other forms of CVD, AACVD precursors do not need to be volatile.[32] The lifting of the requirement for volatility opens up a large range of precursors for use in CVD that would otherwise be unsuitable. This section summarises literature reports of AACVD and the processes which are important when using an aerosol as a transport medium.

1.3.1 Ultrasonic Generation of Aerosols

An aerosol mist can be generated from the surface of a liquid by the application of high-frequency sound waves. This process is known as ultrasonic atomisation.[33] The size of aerosol droplets created in this manner is given by Lang's equation, which is based on earlier work by Rayleigh.[32-34]

$$d = 0.34\left(\frac{2\pi\sigma}{\rho f^2}\right)^{1/3} \qquad (1.6)$$

In equation 1.6, d is the droplet size, σ is the liquid surface tension, ρ is the liquid density and f is the frequency of the sound waves. It can be seen that high frequency sound leads to small droplet size, as does high density and low surface tension of the liquid. Table 1.1 shows the physical constants used in equation 1.6 for a range of solvents,[35] and the calculated aerosol droplet size using a 20 kHz excitation frequency, which is the frequency of the ultrasonic generator used in this work.

Solvent	Density (25°C) / kg L^{-1}	Surface tension (25°C) / N m^{-1}	Lang droplet diameter (20 kHz) / µm
Toluene	0.867	2.85×10^{-2}	59.3
Water	0.996	7.28×10^{-2}	77.4
Methanol	0.791	2.26×10^{-2}	56.6
Acetone	0.784	2.37×10^{-2}	57.6

Table 1.1: Droplet sizes formed from various solvents upon 20 kHz ultrasonic excitation, calculated from equation 1.6.

1.3.2 Aerosol Droplets within the Reactor

In addition to the processes outlined for solid particles, liquid aerosol droplets also undergo evaporation, and the solute within them can undergo precipitation or reaction. The thermal processing of solute containing aerosols to produce solid particles is known as spray pyrolysis and has been studied extensively.[36] Some authors consider AACVD to be a variant of spray pyrolysis,[37] although this assessment neglects the 'true' CVD characteristics demonstrated by AACVD, such as conformal coating.[29, 32] Because particle nucleation is a vital step in the process, previous work on spray pyrolysis will be reviewed in section 1.5, after the necessary theories of particle nucleation have been discussed. What follows in this section is a brief discussion of other aerosol processes within the reactor, including the motion of aerosol particles in a laminar flow.

Within a cold wall CVD reactor, liquid aerosol particles are subject to the same forces as previously described for solid particles. However, the larger size of the aerosol particles will cause important differences in behaviour. As shown in table 1.1, the typical size of aerosol particles produced using a 20 kHz ultrasonic vibration, as used in this work, is 55 – 80 µm. Figure 1.7 shows the variation in gravitational, thermophoretic and diffusion velocities with particle size.[30] The particle density, temperature and temperature gradient used to calculate these results is shown in the figure caption. In the nano-size regime the velocities are in the order diffusion > thermophoresis > settling. In the micron regime the situation is reversed, with settling >> thermophoresis > diffusion. For the particle sizes derived above it can be seen that gravitational settling will be the most important factor in aerosol droplet migration within the reactor.

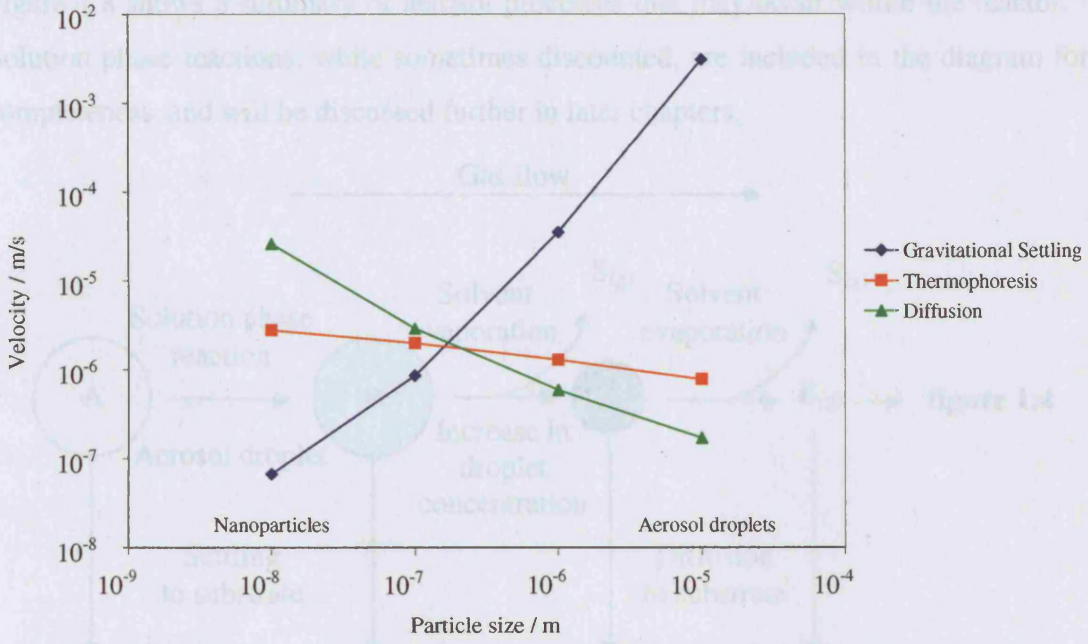

Figure 1.7: Terminal velocities of gravitational settling (particle density 1 g L^{-1}), thermophoresis (temperature gradient 100 K m^{-1}) and Brownian diffusion (temperature 20°C) for spherical particles of various sizes suspended in air.[30] Note the log-log scale.

It is sometimes stated that in AACVD evaporation of the solvent occurs before chemical reaction of the dissolved precursors,[32] although it appears that no direct evidence of this has been reported. Certainly the evaporation to dryness of aerosol droplets occurs very rapidly. Their high surface area and the high temperatures found within the CVD reactor mean that droplet lifetimes can be of the order of milliseconds.[30, 38] The evaporation of aerosol droplets and the formation of particles from their involatile contents will be discussed further in section 1.5.

The lifetime of an aerosol droplet undergoing evaporation is determined by the initial size, the vapour pressure of the liquid, the partial pressure of the corresponding vapour in the surrounding atmosphere and the temperature of the droplet.[30] The vapour pressure will be affected by dissolution of a solute within the droplet; Raoult's Law states that for a non-volatile solute, the vapour pressure will decrease linearly with increasing mole fraction of the solute. As evaporation ensues, the solute concentration will increase, decreasing the liquid vapour pressure and slowing further evaporation.

Figure 1.8 shows a summary of aerosol processes that may occur within the reactor.[39] Solution phase reactions, while sometimes discounted, are included in the diagram for completeness, and will be discussed further in later chapters.

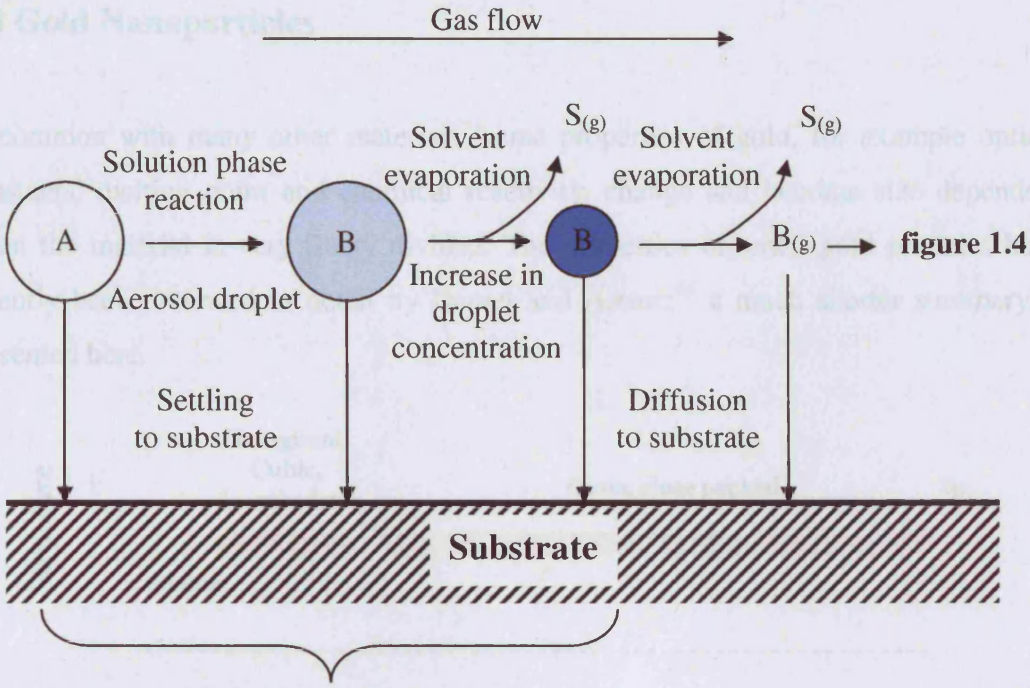

Figure 1.8: Aerosol processes within the CVD reactor. A, and B are chemical species or particles, S is the solvent. If no solution phase reaction occurs then A = B. Once gas phase solvent evaporation has occurred, the precursor, $B_{(g)}$, acts as a gas phase molecular precursor or particle – see figure 1.4 for details of further processes at this point.

Aerosol deposition techniques are categorised by some authors based on the manner of the migration of the precursors to the substrate. Techniques where the aerosol droplet directly impacts onto the substrate *by design* are sometimes, confusingly, labelled 'spray pyrolysis', although the original report by Chamberlin *et al.* did not use this term.[40] This is despite the fact that the term 'spray pyrolysis', as already indicated, usually refers to the gas phase formation of solid particles from an aerosol, rather than film formation from the impaction of an aerosol on a solid substrate.[36, 37] Other terms, such as the Pyrosol process, spray CVD and AACVD all usually refer to techniques where the aerosol is expected to evaporate before it reaches the substrate.[32, 41-44] The distinction is drawn as the latter case, the precursors are vaporised and diffuse to the substrate in the gas phase, in common with other forms of CVD, while in so called spray pyrolysis,

precursors reach the substrate through ballistic motion of the aerosol droplets, which bears more similarity to a line-of-sight PVD process.

1.4 Gold Nanoparticles

In common with many other materials, some properties of gold, for example optical constants, melting point and chemical reactivity, change and become size dependent when the material is very finely divided. The properties of small gold particles have recently been reviewed in detail by Daniel and Astruc;[45] a much shorter summary is presented here.

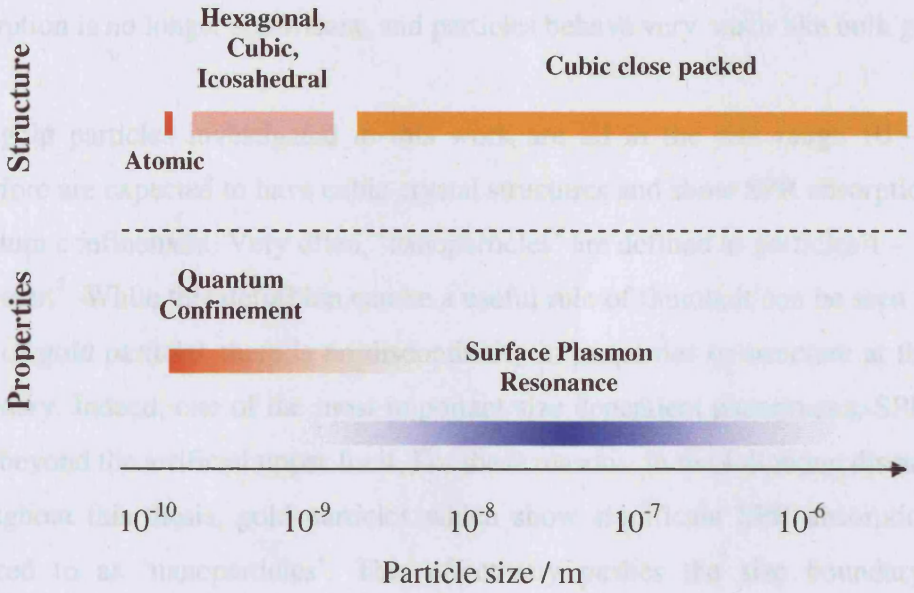

Figure 1.9. Summary of structure and size dependent properties of gold at small particle sizes.

Figure 1.9 shows some of the important properties of gold at different length scales, and the structures that the material adopts at those scales. A gold atom is approximately 2.7 × 10^{-10} m in diameter.[35] Particles from this size up to around 10^{-9} m show strong quantum confinement, *i.e.* the quantisation of electronic energy levels, and can be usefully thought of as clusters of metal atoms.[46-48] Clusters around 10^{-9} m in size have countable numbers of atoms, and certain 'magic numbers' of atoms lead to stable clusters. Clusters with 13, 54, 55, 57, 147, 154 and 187 gold atoms are particularly stable, and each of these clusters has a preferred geometrical structure: hexagonal, cubic, icosahedral, and others.[49] Most of these structures are based on concentric

spherical shells of 12-coordinate gold atoms. Above around 3×10^{-9} m, quantum confinement ceases, and the electronic structure of the material becomes much like the band structure of the bulk solid. At this point, the number of atoms in each particle becomes large, and not easily countable. The crystal structure becomes cubic close packed, as found in the bulk solid, and each particle may be made up of more than one crystallite. This point is sometimes considered the boundary between gold clusters and gold colloids.[45] In the size interval 3×10^{-9} m to around 5×10^{-7} m, the optical properties of gold particles are dominated by surface plasmon resonance (SPR),[2] which will be discussed at length in the following section. Particle shapes can vary widely, and are determined by particle growth processes rather than gold atom packing. A very wide range of shapes can be produced. Above around 5×10^{-7} m in diameter, the SPR absorption is no longer significant, and particles behave very much like bulk gold.

The gold particles investigated in this work are all in the size range 10 – 200 nm, therefore are expected to have cubic crystal structures and show SPR absorption, but not quantum confinement. Very often, 'nanoparticles' are defined as particles 1 – 100 nm in diameter.[7] While this definition can be a useful rule of thumb, it can be seen that in the case of gold particles there is no discontinuity in properties or structure at the 100 nm boundary. Indeed, one of the most important size dependent phenomena, SPR, extends well beyond the artificial upper limit. For these reasons, in the following discussion, and throughout this thesis, gold particles which show significant SPR absorption will be referred to as 'nanoparticles'. This effectively pushes the size boundary of gold nanoparticles to around 500 nm, which is thought to be a delineation more rooted in the relevant size dependent phenomena rather than somewhat arbitrary multiples of SI units.

1.4.1 Surface Plasmon Resonance

It was established in the previous section that the most prominent nanoscale property of gold in the size interval investigated in this work is surface plasmon resonance (SPR). A surface plasmon (SP) is a coherent and collective oscillation of free electrons at the boundary between a metal and an insulator.[50-52] It is a multi-electron rather than a single-electron excitation involving all the free electrons at the metal surface. When no boundary conditions are imposed, and in the case of a perfect, defect-free metal, the oscillation frequency of the SP depends only on the dielectric properties of the two materials. When boundary conditions are imposed, the size and shape of the metal phase

increasingly affect the SP frequency. Electromagnetic radiation can couple to the SP of a metal when the electric field of light oscillates at the resonant frequency of the SP. This phenomenon is known as Surface Plasmon Resonance (SPR), and results in strong absorption of light at the resonant frequency.

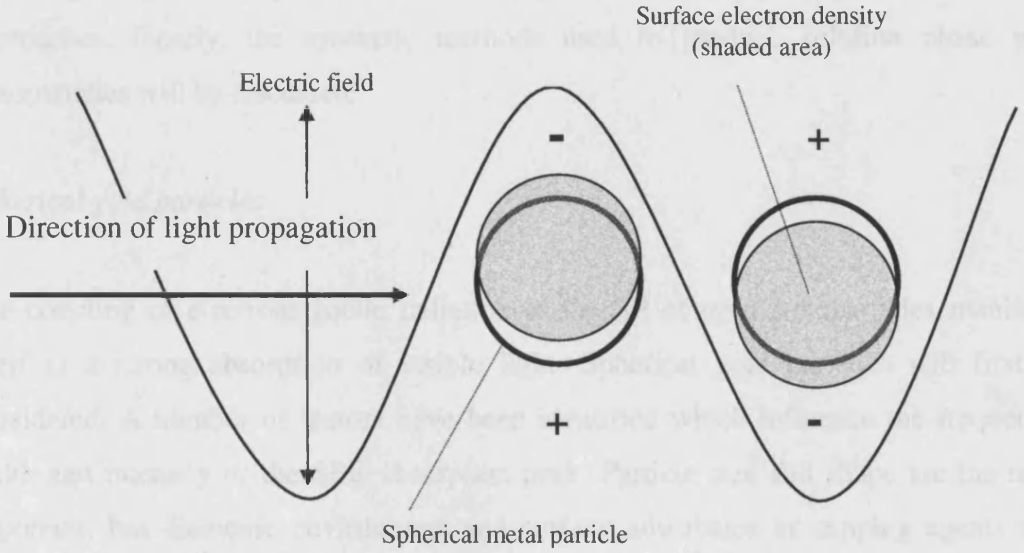

Figure 1.10. Scheme to illustrate the excitation of a dipolar surface electron oscillation, or SPR, by the electric field of incoming light. The grey shading represents surface electron density. The frequency of the oscillation is equal to the frequency of the resonant light. The particle is much smaller than the wavelength of the incoming light, so is homogeneously polarised.[53]

Figure 1.10 shows the interaction of the electric field of light with a metal sphere. The oscillating electric field induces a resonant oscillation of the surface free electrons in the particle. The SPR shown in figure 1.10 is dipolar as the oscillation is one-dimensional.[53] Dipolar SP oscillations are induced when the particle size is much smaller than the wavelength of the exciting radiation, as in this case the particle experiences a near homogeneous polarisation. Quadropolar and higher order SPs can be supported by larger particles where the field is non-homogeneous; this is discussed further below.[54] The frequency of SP oscillation corresponds to visible light for group 11 (coinage) metals and alkali metals in the sub-micron size regime. The optical properties of group 11 and alkali-metal nanoparticles above 10 nm in diameter are dominated by absorption caused by SPR, as other size-dependent effects, such as quantum confinement, are negligible in metal particles of this size. The extinction coefficients of these SPR absorptions are in some cases several orders of magnitude greater than the strongest

known organic dyes.[53] The extremely high reactivity of finely divided alkali metal particles has prevented detailed study of their optical properties; conversely, the chemical robustness of group 11 nanoparticles, especially gold particles, has allowed their extensive investigation.[45, 55] The experimental results will first be summarised, focussing on gold nanoparticles, followed by a discussion of the various theoretical approaches. Finally, the synthetic methods used to produce solution phase gold nanoparticles will be discussed.

Spherical gold particles

The coupling of electromagnetic radiation to the SP of gold nanoparticles manifests itself as a strong absorption of visible light. Spherical gold particles will first be considered. A number of factors have been identified which influence the frequency, width and intensity of the SPR absorption peak. Particle size and shape are the most important, but dielectric environment and surface adsorbates or capping agents also have an effect.

Visible light absorption spectroscopy has been carried out on individual spherical gold particles[56] and dilute solutions of spherical gold nanoparticles in water, which behave as individual particles.[2, 57, 58] Figure 1.11 shows published data from several groups on the SPR of aqueous spherical gold nanoparticles of various diameters. The greater concentration of data points for small particle diameters reflects the easier synthesis of smaller particles (as discussed in the following section). Three size regimes can be identified; in the first, for particles below approximately 40 nm in diameter, the SPR absorption peak is centred around λ = 530 nm, and the peak position is only slightly affected by particle size. The shift in SPR peak maximum is only 10 nm (a change of 0.05 eV) moving from a particle diameter of 9 to 41 nm. The bandwidth of the absorption, however, is strongly size dependent and increases with decreasing particle size.[2] In the second size regime, with diameters between approximately 40 nm and 140 nm, the position of the SPR absorption red-shifts with increasing particle size, from λ = 530 nm at d = 40 nm to λ = 632 nm at d = 140 nm.[54] In this size regime, the absorption bandwidth (full width at half maximum (FWHM)) increases with increasing size from around $\Delta\lambda$ = 80 nm for d = 40 nm to $\Delta\lambda$ = 160 for d = 100 nm. As the particle diameter increases above 100 nm, a shoulder appears on the blue side of the absorption peak. In

the third size regime (particles over 140 nm) the shoulder evolves into a distinct absorption maximum. Both peaks continue to red shift and broaden with increasing size.

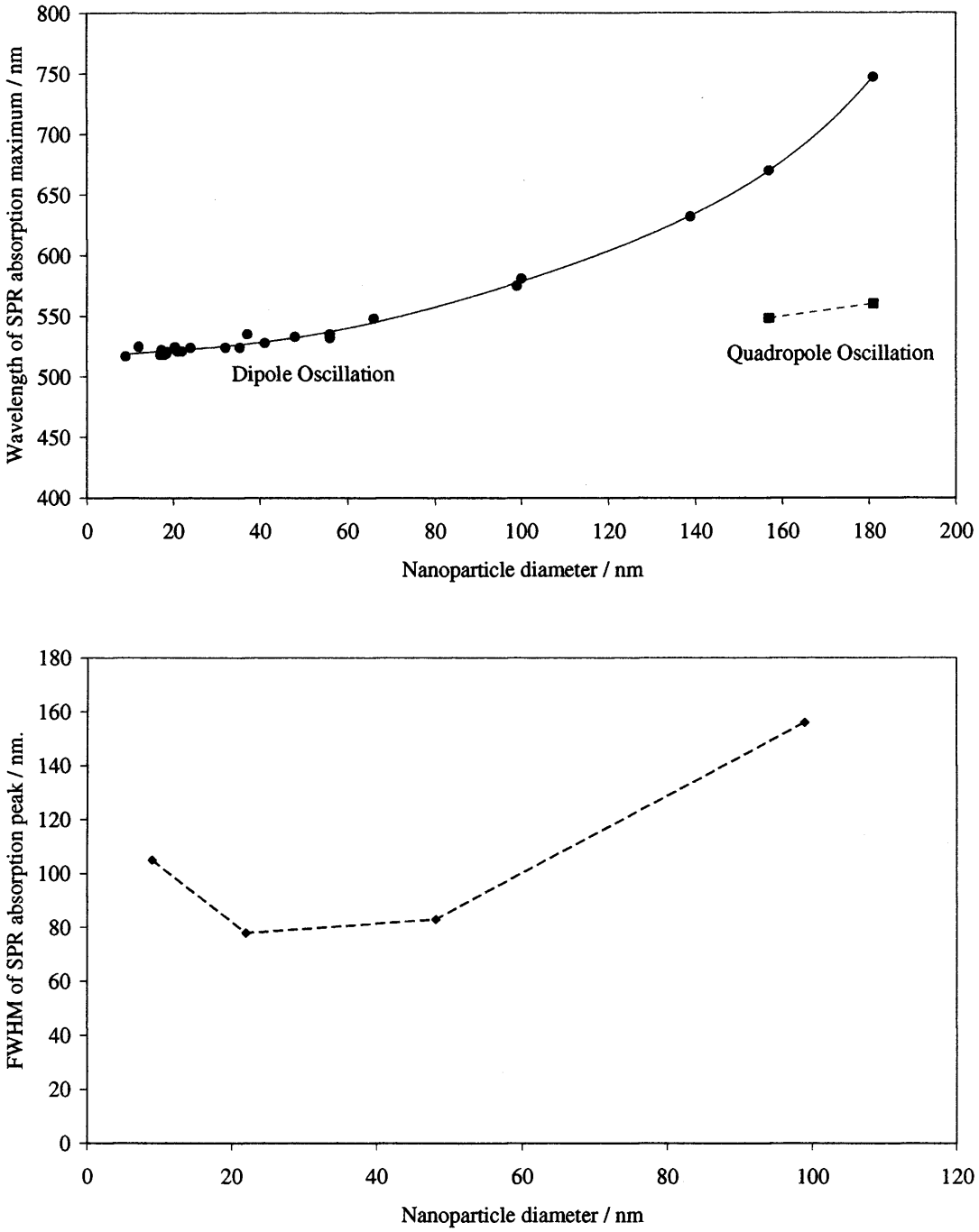

Figure 1.11. ***Top*****: Experimentally observed relationship between SPR absorption peak position and nanoparticle diameter. All samples were spherical citrate-stabilised gold particles in water.[2, 54, 57-59] Both dipolar (circles) and quadropolar (squares) oscillations are observed. The dashed curves are arbitrary and act as a guide to the eye.** ***Bottom*****: Experimentally observed relationship between FWHM of the SPR absorption peak and nanoparticle diameter.**

The dielectric environment of the particles was investigated by dissolving gold colloids in various solvents and solvent mixtures with different refractive indices (n).[60] In each case the size of the gold particles was 16 nm. When dissolved in water (n = 1.33) the SPR peak appears at λ = 520 nm. The peak is red-shifted in a medium of higher refractive index, reaching λ = 546 nm when dissolved in CS_2 (n = 1.6); the relationship appears roughly linear in the range investigated (figure 1.12).

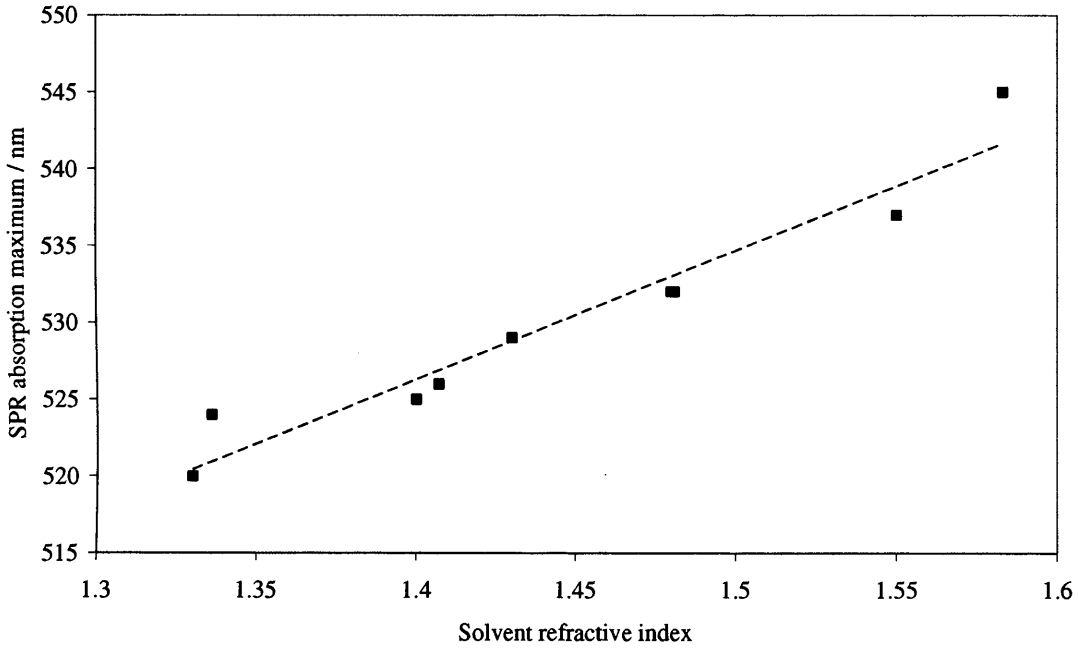

Figure 1.12. Experimentally observed SPR absorption maximum of 16 nm diameter gold particles dissolved in solvents of various refractive index.[60, 61] The dashed line is a guide to the eye.

Non-spherical gold particles

The SPR frequency in nano-scale gold is also strongly affected by the shape of the particle.[50, 53] Nanorods, *i.e.* particles with one long axis and two short axes, display two SPR absorption peaks, assigned to a transverse and a longitudinal oscillation.[62] The longitudinal SPR peak occurs at longer wavelengths, and is highly sensitive to the particle aspect ratio (the length ratio of the long axis to the short axis). Figure 1.13 shows the SPR absorption peak positions obtained by several groups for the transverse and longitudinal oscillations of aqueous surfactant-stabilised gold nanorods of various aspect ratios. The longitudinal SPR peak is strongly dependent on the aspect ratio,

varying from λ = 610 nm at aspect ratio 2.1 to λ = 1040 nm at an aspect ratio of 6.0. The relationship between SPR peak and aspect ratio appears linear over this range. The wavelength of the transverse SPR peak is included where reported in the literature. This peak appears invariant with aspect ratio.

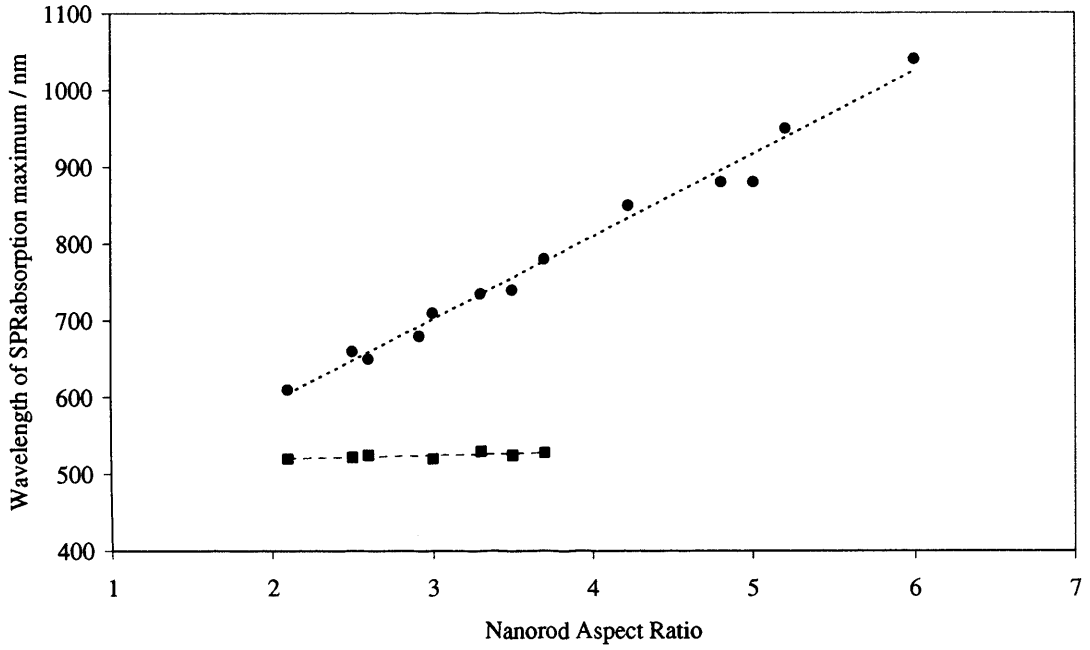

Figure 1.13. Experimentally observed relationship between SPR absorption maximum and nanorod aspect ratio for aqueous gold nanorods stabilised by various surfactants.[63-66] Longitudinal (circles) and transverse (squares) SPR absorptions are observed. Transverse SPR peaks were not reported for all samples. The dashed lines are a guide to the eye.

Thin films of gold

At small separations, gold nanoparticles show changes in their SPR behaviour. In dilute solution, the SPR absorption of gold nanoparticles is identical to that of individual gold particles, all other factors being equal,[2, 56] indicating that the is no interaction between particles in these solutions. At small particle separations, which can occur in thin films of gold, the SPR absorption is red-shifted compared to the isolated nanoparticles.

Thermal evaporation has been extensively investigated as a method for depositing thin films of gold. Discontinuous gold films show a SPR absorption that is highly sensitive to dielectric environment, film thickness, morphology and surface roughness.[67-71] Films

grown by physical and chemical techniques tend to show island growth morphology. Such films can be characterised by the island width, island separation and island thickness, although a typical sample will have a wide distribution of each attribute. It is also difficult to control these attributes independently, and therefore it is hard to assign changes in the SPR absorption to one factor in particular. In general, films of small, thin, well separated islands give narrow SPR absorption peaks at short wavelengths as might be expected of a solution phase sample of gold nanoparticles.[71] A film made up of large, thick, closely spaced islands has a significantly red-shifted and broadened peak SPR absorption peak. The precise optical attributes are highly dependent on the sample preparation method, and in addition, the optical properties are significantly altered by heating[71] or exposure to organic solvents in either liquid or vapour phase,[68] which is thought to alter the surface roughness of the film. If the islands are large enough to form a continuous film, then the plasmon properties are lost, and the film behaves optically as bulk gold.[69]

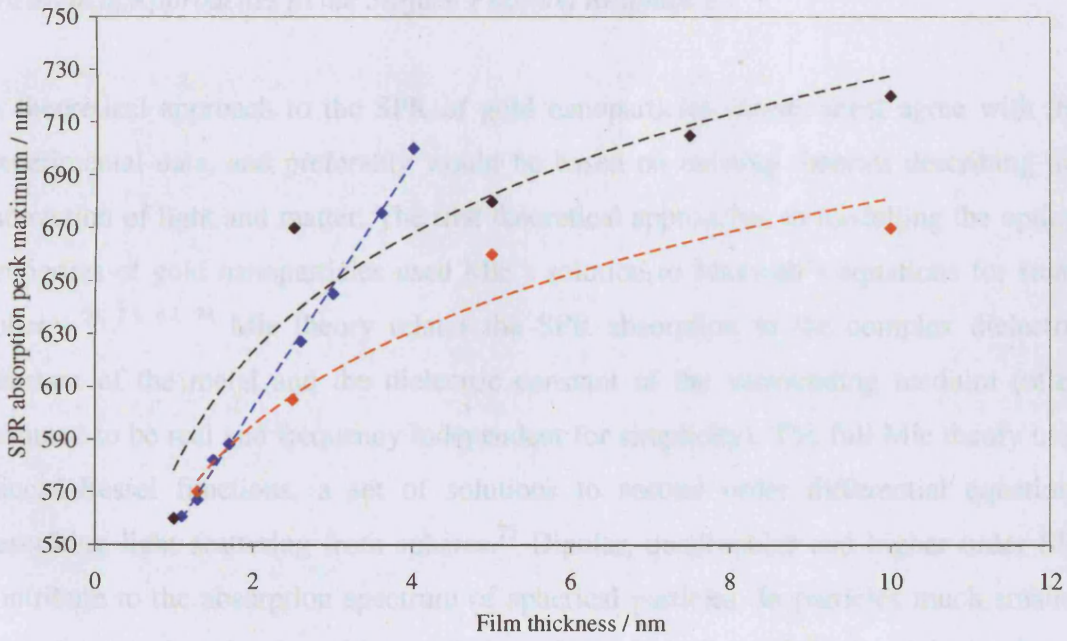

Figure 1.14. Relationship between film thickness and SPR absorption peak maximum, taken from three separate literature studies of discontinuous gold films deposited by a variety of methods.[71-73] Data from the three separate studies are shown in red, blue and black. Dashed lines act as a guide to the eye.

In one study, thin gold films made up of small islands with average diameter 11 nm showed SPR absorption maxima around $\lambda = 570$ nm, while increasing the island size to an average diameter of 40 nm caused a red-shift of the SPR peak to $\lambda = 650$ nm,

accompanied by a broadening of the SPR peak.[72] This red-shift is significantly greater than is observed in spherical solution phase particles of the same diameters. The limit to this process is the merger of the islands to create a continuous gold film, which displays bulk metal-like absorption rather than a distinct a SPR peak.[71] Annealing the films at high temperature causes a significant change in the SPR absorption. Annealing was found to affect the morphology of the gold films in several ways. The average size of the metal islands increased, and the separation between islands also significantly increased. These changes caused a blue shift of the SPR peak to a value of approximately λ = 540 nm, regardless of the original SPR position. Figure 1.14 shows results from three studies on the SPR wavelength of gold films of different thickness. It can be seen that there is some variation in the SPR wavelength at specific thicknesses in these different studies, showing that the SPR is strongly dependent on the film morphology and not just the thickness[71-73]

Theoretical Approaches to the Surface Plasmon Resonance

A theoretical approach to the SPR of gold nanoparticles clearly must agree with the experimental data, and preferably would be based on existing theories describing the interaction of light and matter. The first theoretical approaches to modelling the optical properties of gold nanoparticles used Mie's solution to Maxwell's equations for small spheres.[50, 53, 62, 74] Mie theory relates the SPR absorption to the complex dielectric constant of the metal and the dielectric constant of the surrounding medium (often assumed to be real and frequency independent for simplicity). The full Mie theory uses Riccati-Bessel functions, a set of solutions to second order differential equations describing light scattering from spheres.[75] Dipolar, quadropolar and higher order SPs contribute to the absorption spectrum of spherical particles. In particles much smaller than the wavelength of exciting radiation, the polarisation of the particle is almost homogeneous, so only dipolar SPs excited (see figure 1.10). A simplification of the Mie solution which considers only dipolar SPs is known as the dipole or quasi-static approximation, as in this approximation the SPR frequency is size-independent. The Mie equation for dipolar SPR absorption is as follows:[2, 76]

$$\sigma_{ext} = 9\frac{\omega}{c}\varepsilon_m^{3/2}\frac{\varepsilon'(\omega)}{(\varepsilon'(\omega) + 2\varepsilon_m)^2 + \varepsilon''(\omega)^2} \qquad (1.7)$$

where σ_{ext} is the extinction coefficient, ω is the frequency of the electromagnetic radiation, ε_m is the real part of the dielectric constant of the surrounding medium, $\varepsilon'(\omega)$ and $\varepsilon''(\omega)$ are the real and imaginary parts respectively of the frequency dependent dielectric function of gold and c is the speed of light. The imaginary part of the dielectric function of the surrounding medium is assumed to equal zero, which is a reasonable approximation for most non-metals at visible frequencies. The size of the particles is not explicitly included in the equation, as the SPR frequency is largely independent of particle size in the dipole-only approximation. However, the dielectric function of gold is size dependent for very small particle sizes,[2, 76] leading to a weak size dependence of the SPR peak, hence the label 'quasi-static'. Size dependent values of $\varepsilon'(\omega)$ and $\varepsilon''(\omega)$ can be calculated using the Drude model. From equation 1.7, the extinction coefficient passes through a maximum when:

$$\varepsilon'(\omega) = -2\varepsilon_m \qquad (1.8)$$

This is the resonance condition for the dipole approximation of Mie theory.

The bandwidth of the SPR, and hence the breath of the optical absorption peak is not described in equation 1.7, but is dependent on the lifetime of the SP oscillation. The decay of SP oscillations typically occurs through non-radiative pathways, such as scattering from the metal surface, electron-phonon and electron-electron scattering or transfer of energy from the collective electron oscillation to individual electron excited states,[77] although radiative decay (electron-photon decay) also occurs.[56]

1.4.2 Synthesis of Gold Nanoparticles in Solution

Gold nanoparticles have been manufactured, albeit unknowingly, since ancient times and used to colour materials, such as glass, for decorative purposes.[78] Faraday reported the first systematic study of the synthesis of gold colloids, and was the first to relate the various colours of the particles to their size.[79] He synthesised aqueous gold particles by reduction of $AuCl_3$ by phosphorous. Subsequently, the solution phase synthesis of gold particles has been almost universally achieved by the reduction of hydrogen tetrachloroaurate:

$$[HAuCl_4] + 3e^- \rightarrow Au^0 + H^+ + 4Cl^-$$

Hydrogen tetrachloroaurate is a strong oxidising agent ($E° = +1.002$ V)[80] therefore relatively mild reducing agents can be used. The development of electron microscopy has allowed direct measurement of particle size, and since then, a variety of methodologies have been reported using different reducing agents, stabilizing agents and solvating media. Efforts have been made to control the mean size, shape and size distribution of the gold particles, and in this regard, landmark contributions have been made by Turkevich, who first synthesised gold particles by citrate reduction and measured their size distributions,[81] Brust *et al.*, who first reported the stabilisation of gold particles in a non-polar solvent through thiol capping,[82] and Murphy *et al.*, who first reported the seeded growth of gold nanorods of controlled aspect ratio using a shape directing surfactant.[77] These methods have been extended by very many others. The key methods of solution phase spherical gold nanoparticle synthesis are summarised in Table 1.2.

Role of reducing agents and stabilising agents

As can be seen in table 1.2, many gold nanoparticle syntheses have been developed using different reducing agents, stabilising agents and solvents. The reducing agent is the substance used to reduce Au^{3+} to Au^0. Since $[HAuCl_4]$ is a strong oxidising agent, a wide range of reducing agents can be used. As discussed further below, nanoparticle agglomeration can be an energetically favourable process. While agglomeration can be desirable as a growth mechanism, uncontrolled agglomeration leads to rapid size increase and loss of nano-scale properties. Stabilising agents are used to prevent this. Two types of stabilising agents can be identified: ionic and non-ionic. Ionic stabilising agents, such as the citrate anion, are attracted electrostatically to the gold particle surface. Non-ionic stabilising agents, such as thiols, form a chemical bond with the gold surface. The gold particles are then said to be either charge stabilised or ligand stabilised respectively. Both methods physically prevent contact between particles, and hence prevent agglomeration. Stabilising agents also act to functionalise the nanoparticle surface for compatibility with different solvents. Surfactants, having a polar and non-polar (hydrophilic and lipophilic) are often used for this purpose. For example, long chain alkane thiols have been used to create gold particles soluble in non-polar solvents.[82] In many cases, the reducing agent also acts as the stabilising agent.[81]

Particle size distribution

The size distribution of nanoparticles is an important consideration. Narrow size distributions, *i.e.* low standard deviations, are generally held to be desirable; one reason is that commonly used models of optical or physical properties of nanoparticles assume that all the particles are identical; thus such models are more applicable to samples of particles with narrow size distributions. Some physical phenomena are only observable in arrays of nearly identical particles. While monodispersity – all particles identical in size and shape – is desirable, it is virtually unachievable in macro scale samples of nanoparticles. This strict definition of the term 'monodispersity' is rarely adhered to in the literature, and samples of particles with very narrow size distributions are labelled 'monodisperse'. Samples with standard deviations of below 15% and 9% of the arithmetic mean have been labelled as 'monodisperse' and 'highly monodisperse' respectively by leading authors.[83, 84] Particles with small absolute standard deviations are also called monodisperse, even if the standard deviation is a large percentage of the mean particle size.[85] An alternative definition of monodispersity, although one that is rarely used, is that the particles should be able to form an ordered 2-dimensional hexagonal close packed lattice when dispersed on a TEM grid.[86] This calls for a particle size distribution with standard deviation below 6% of the mean.

Particle size distributions are commonly measured using images recorded by high resolution TEM or SEM. Particle sizes are measured manually or automatically using computer software. Statistical distributions are often used to fit the size distribution data; normal (Gaussian)[87] or log-normal distributions[59, 88, 89] have been used to fit gold particle size distributions.

Particle nucleation and growth mechanisms

Before discussion of the various synthetic strategies used for creating gold particles, the process of solution phase particle formation should be addressed. LaMer *et al.* identified distinct particle nucleation and growth steps that occur in supersaturated solutions.[90] Their work was on particles of sulfur, but their conclusions can be applied to nucleation of any solid particles. Homogeneous nucleation is the homogeneous formation of a small solid particle through precipitation from the solution phase. Heterogeneous growth is a surface reaction which leads to addition of atoms to the nucleated particle,

increasing its size. LaMer *et al.* proposed that a supersaturated solution undergoes a period of rapid homogeneous nucleation, relieving the supersaturation and resulting in very small particles, known as primary particles. This is followed by a slower heterogeneous growth phase in which each of the particles grows through diffusion limited surface reactions. Given a uniform rate of heterogeneous growth, these processes result in monodisperse particles, known as secondary particles.

A problem associated with this explanation is that particles growing spontaneously from solution (homogeneously) need to achieve a critical size before growth is energetically favourable; below this size, the particles spontaneously dissolve. The critical size depends on the material and reaction conditions, but for gold it is thought to be around 20 atoms.[81, 83] LaMer and others have explained the spontaneous formation of particles greater than the critical size by statistical fluctuations.[83, 90] Turkevich preferred an explanation involving chemical interactions between precursor molecules, creating a kind of loosely bound cluster.[81] More recently it has been suggested that true homogeneous nucleation does not occur, or at least is very difficult to achieve, and that particle nuclei form heterogeneously around impurities, gas bubbles or at the reaction vessel surface.[91]

The growth phase of the process may also be more complex than LaMer's model. It has been found in several systems that the final monodispersed particles are made up of many agglomerated primary particles.[89] This suggests that particle agglomeration, as well as heterogeneous surface reaction, is an important growth mechanism. The surface of a material is a region of high energy, and since nanoparticles have a high surface to bulk ratio, agglomeration of particles can be highly energetically favourable. Even after the exhaustion of the solution phase reactant, particles may continue to grow through aggregation. Due to their higher surface areas, smaller particles are more likely to be subsumed by larger particles, so this process leads to a reduction of the population of smaller particles. If unchecked, the agglomeration of particles will lead to continuing particle size increase, usually resulting in loss of 'nano-scale' properties, and precipitation of a fine metal powder. A key aspect of nanoparticle synthesis is therefore the stabilisation of the system with respect to agglomeration. This can be achieved by the binding of a molecule to the surface of the particle, preventing further aggregation. The termination of particle growth is therefore dependent not only on the depletion of reactants but also the effective passivation of the particle surface by a stabilizing agent

in order to prevent agglomeration or further growth. Figure 1.15 summarises the processes described above.

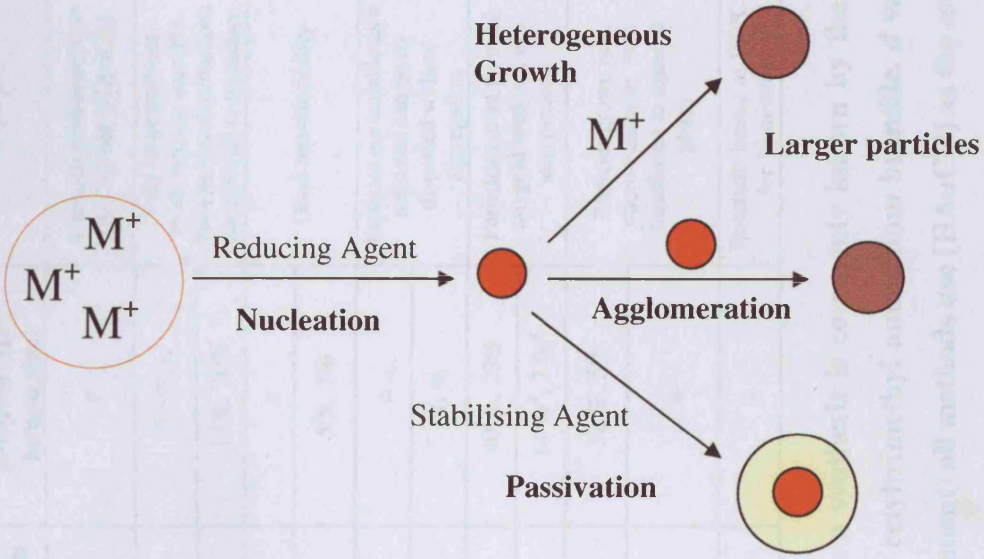

Figure 1.15. Summary of processes that occur in solution phase metal nanoparticle synthesis. M^+ represents metal precursor chemicals.

Gold nanoparticle synthesis techniques

Table 1.2 shows a summary of key gold nanoparticle synthesis techniques. Apart from the first entry, Faraday's synthesis using phosphorous, which is included for historical interest, all of these techniques are in current use. All methods use a reducing agent and stabilising agent, which may be ionic or non-ionic, as previously discussed. Turkevich's original method used sodium citrate as a reducing agent, and the citrate anion produced as a stabilising agent, giving charge stabilised gold particles. The size of the particles could be varied by changing the amount of reducing agent used: a greater amount of reducing agent led to smaller particles.[81] The aqueous synthesis of gold nanoparticles has also been carried out using sodium borohydride, a much stronger reducing agent, and various polymers as stabilising agents.[84] This led to significantly smaller particles.

Method	Solvent	Reducing Agent	Stabilising Agent	Range of particle diameters / nm	Particle diameter standard deviation (smallest size, largest size)	Comments	References
Reduction by Phosphorous (Faraday)	Water	Phosphorous	PCl_3?	*a*	*a*	Synthesis performed with $[AuCl_3]$ **not** $[HAuCl_4]$	79
Aqueous Reduction (Turkevich)	Water	Sodium citrate	Citrate anion	16 - 120	12.5%, *a*	Very large particles (>100nm) are unstable. Particle size distributions are difficult to reproduce	81, 92, 93
		Ascorbic acid	Ascorbate anion	10 - 97	13%, 20%		92
		Poly(sodium acetate)	Poly(sodium acetate)	13	*a*	Good reproducibility	94
		Sodium borohydride	Poly(acrylic acid), other polymers	1.8 – 5.3	5%, 7%		84
Toluene Reduction (Brust-Schiffrin)	Toluene	Sodium borohydride	Dodecane thiol	0.75 – 8.0	*a*	Particles are isolable as a solid and can be re-dispersed without aggregation	82, 88, 95
			MSA[b]	1.0 – 3.6	26 %		95
Seed Mediated	Water	Seed: Sodium citrate Particles: Ascorbic acid	Ascorbate anion	14 - 48	40 %, 29%	Particles grown from 12 nm gold seed in a two step process	96
			CTAB[c]	66 - 181	14 %[d], 7 %[d]		54
Micro-emulsion	Pentanol / toluene	PEI[e]	PEI[e]	7 - 21	32 %, 5%	Particles grown in a micro-emulsion, then transferred to aqueous phase	97, 98
	Pentanol / hexane / water	Sodium borohydride	CTAB[c]	7	*a*		99
Solvothermal Synthesis	Toluene	Oleylamine	Oleylamine	2 - 3	*a*	Reactants heated at 160°C for 30 minutes	100

Table 1.2. Synthetic routes to solution phase spherical gold nanoparticles. Where a synthesis is commonly known by the name of the discoverer, this is noted. Notes: *a*, value not reported. *b*, mercaptosuccinic acid. *c* cetyltrimethyl ammonium bromide. *d* value reported after a purification step. *e* Poly(ethyleneimine). Except for the first method (see comment) all methods use [HAuCl4] as the source of gold.

Brust *et al.* first reported the controlled synthesis of gold particles in an organic solvent, toluene.[82] They used a phase transfer agent, tetraoctylammonium bromide (TOAB) to transfer the $AuCl_4^-$ anions to the toluene phase. The phase transfer occurs through association of the $AuCl_4^-$ and the phase transfer agent. In the organic phase, it is thought that the formation of an inverse micelle may occur.[77] Figure 1.16 shows cross section of the micellar structure. At the hydrophilic centre is $AuCl_4^-$ surrounded by the polar ends of the TOA^+ surfactant. Some halide exchange occurs between the TOAB and the $AuCl_4^-$, so the gold species present may in fact be $AuBr_4^-$.[101] The hydrophobic alkane chains of the quaternary ammonium ions extend into the non-polar solvent. After phase transfer, sodium borohydride is used as a reducing agent, and dodecane thiol as a stabilising agent, yielding ligand stabilised particles under 10 nm in size. In this synthesis, the amount of dodecane thiol influenced the final size of the nanoparticles.

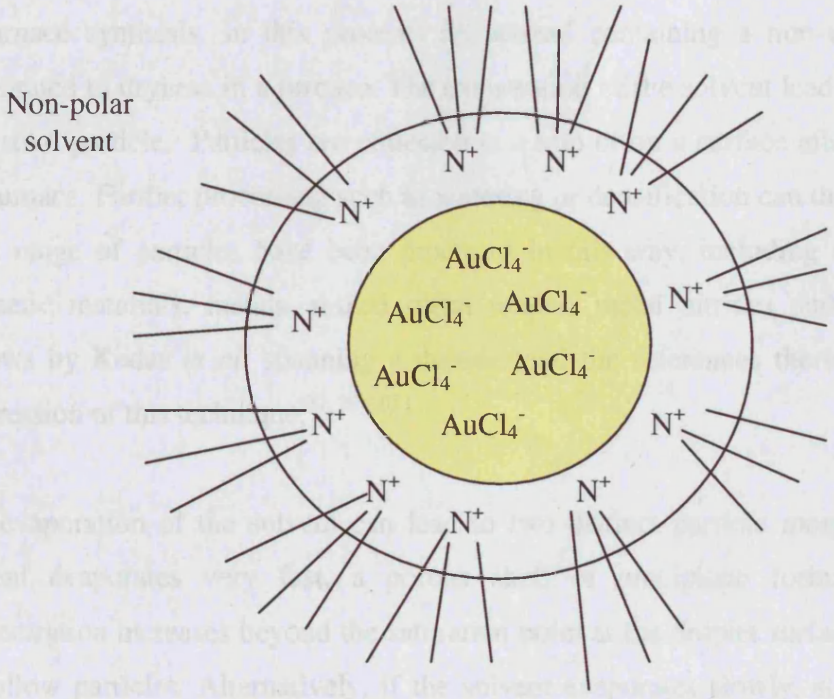

Figure 1.16. Cross section of an inverse micelle that may form between [$HAuCl_4$] and surfactants in a non polar solvent.

Seed mediated syntheses use small pre-formed particles, typically produced by the Turkevich method, as seeds to grow larger gold particles.[96] This type of synthesis

effectively by-passes the nucleation step, as heterogeneous particle growth occurs at the surface of the seeds. This methodology has allowed very large particles (180 nm) to be grown with narrow size distributions.[54]

1.5 Aerosol Synthesis of Nanoparticles

1.5.1 Solution Aerosol Synthesis (SAT)

The thermal synthesis of particles from an aerosol containing a solute is commonly known as spray pyrolysis.[36] However, as indicated in a previous section, this term has also been applied to a method of thin film formation where a precursor containing aerosol is sprayed directly onto a heated substrate. To avoid confusion, the alternative term, solution aerosol thermolysis (SAT), will be used for this process. Many variants of SAT have been investigated, such as flame synthesis, furnace synthesis, gas condensation and laser ablation.[37] The most relevant to the work presented in this thesis is furnace synthesis. In this process, an aerosol containing a non-volatile solute is evaporated to dryness in a furnace. The evaporation of the solvent leads to precipitation of a solid particle. Particles are collected in a trap or on a surface after passing out of the furnace. Further processing such as sintering or densification can then occur. A very wide range of particles have been produced in this way, including superconductors, magnetic materials, metals, mixed metal oxides, metal nitrides and others. Several reviews by Kodas *et al.* spanning a decade (and the references therein) illustrate the progression of this technique.[37, 39, 102]

The evaporation of the solvent can lead to two distinct particle morphologies. If the solvent evaporates very fast, a porous shell of precipitate forms as the solute concentration increases beyond the saturation point at the droplet surface. This can lead to hollow particles. Alternatively, if the solvent evaporates slowly, solute has time to diffuse away from the region of high concentration at the droplet surface. In this scenario, solid particles are thought to form through the nucleation and growth processes outlined previously. The resulting particles may be porous due to the escape of solvent molecules trapped within the growing particle.[102, 103] Parameters such as furnace temperature and solute concentration affect the particle size and size dispersity.

A few reports of gold particle synthesis by SAT are available. Grunwaldt *et al.* used flame synthesis to form gold particles from a solution of $Me_2Au(acac)$.[104] The particles were collected on a pre-formed TiO_2 substrate, and used as CO oxidation catalysts. Particle sizes were in the 2-4 nm region, although detailed particle size distributions were not reported. Okuyama *et al.* produced Au-Pd alloy particles using a SAT technique.[105] $[HAuCl_4]$, $[Au(OH)_3]$, $[H_2PdCl_6]$ and $[Pd(NO_3)_2]$ were used as precursors, dissolved in aqueous solutions of HCl and HNO_3. Spherical particles were produced, when suitable Au : Pd ratios were used, but no size distributions were measured. This is the only literature report of $[HAuCl_4]$ being used as a gold particle precursor in a SAT or other gas phase particle or film formation technique.

1.5.2 Electrospray Deposition

A technique related to SAT is electrospray deposition, or electrospray pyrolysis. In this technique, a precursor solution is sprayed through a nozzle and combined with an inert gas flow.[106] The aerosol droplets produced are charged, and are directed through a drying furnace toward a substrate which may be heated. If a conducting, electrically isolated substrate is used, the current generated by the deposition of charged aerosol droplets can be used as a method for measuring the number of droplets deposited. Electrospray deposition was initially used as a mass spectrometric technique,[107, 108] but has recently been developed into a method for nanoparticle deposition. Early work by Okuyama *et al.* resulted in the first detailed study of deposition of nanoparticles by electrospray deposition.[109] Silica, gold, palladium and polymer particles were deposited using preformed nanoparticle solutions. In the case of gold particles, films with narrow, lognormal particle size distributions were obtained, presumably similar to that of the starting solution, although this is not explicitly stated. The optical properties of these films were not investigated. Subsequent work by a number of researchers extended the method to deposit a variety of other particulate films.[110-112]

1.6 Gold / Semiconductor Nanocomposites

Nanocomposites are materials consisting of two or more separate phases (usually solid), at least one of which is nano-scale in one, two or three spatial dimensions. Hence metal nanoparticles incorporated into a host dielectric matrix is an example of a nanocomposite, and is an arrangement which has been investigated heavily in recent

years. In their detailed review of metal nanoparticle / semiconductor composites, Tondello *et al.* highlighted a distinction between what they termed 'inside cluster' systems, where the metal particles are completely surrounded by the semiconductor matrix, and 'outside cluster' systems, where the metal particles are supported on the semiconductor surface.[101] Mixed systems are also possible, where particles are both inside and on top of the semiconductor phase. The reason for drawing this distinction is to highlight the different potential applications for each arrangement. Inside cluster systems may be useful in optical applications, as the metal nanoparticles can interact with incoming light without being physically separated from their environment by the semiconductor. Outside cluster systems may be used as catalysts, sensors or Raman substrates, as the gold particle can interact chemically with their surroundings.

1.6.1 Properties of Gold / Semiconductor Nanocomposites

The incorporation of gold nanoparticles within a semiconductor matrix can alter the properties of both phases. As can be seen from equation 1.8, the SPR wavelength of a gold nanoparticle is dependent on the dielectric properties of the surrounding matrix. According to this statement of Mie theory, matrices of high refractive index will cause a red shift in the SPR wavelength. This has been observed experimentally.[113, 114] The electronic properties of the semiconductor can also be changed by the incorporation of a metallic phase, and this especially applies to processes which involve photo-excitation of the semiconductor and charge separation.[115] This has been exploited to improve the photocatalysis of TiO_2 films,[116-118] the electrochromism of WO_3,[119-121] and the photochromism of MoO_3 films.[122-125]

1.6.2 Synthesis of Metal / Semiconductor Nanocomposites

A great number of synthetic routes to nanocomposites have been developed. Figure 1.17 categorises nanocomposite syntheses based on the starting materials and the steps involved in the synthesis.

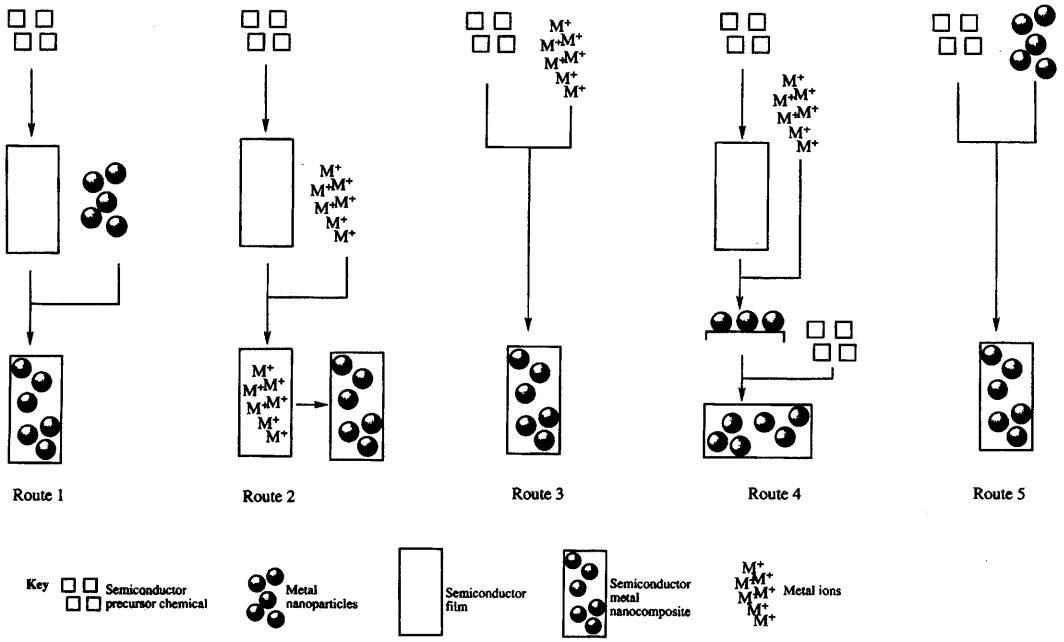

Figure 1.17. Synthetic routes to metal / semiconductor nanocomposite thin films. Each arrow represents a single step process, *e.g.* CVD, spin coating, annealing, sputtering, etc.

Several strategies for production of semiconductor / metal composites have been developed. As shown in figure 1.17, they can be broadly divided into five categories:

- Route 1 is the synthesis of the semiconductor matrix followed by addition of pre-formed nanoparticles in a second step. Examples of this strategy include spin coating or dip coating a semiconductor film with a nanoparticle solution.[115, 119, 120, 126] The nanoparticles are chemically bound to the surface or become trapped within pores in the semiconductor.
- Route 2 is the synthesis of the semiconductor matrix followed by application of metal ions in a second step, leading to formation of metal particles *in situ*, within the film. High energy ion implantation[127-129] and spin coating with a solution of metal ions followed by photocatalytic reduction or heat treatment[130,131] are examples of this strategy.
- Route 3 is the synthesis of the semiconductor matrix and metal particles in a single step. Examples include sol-gel using both semiconductor and nanoparticle precursor,[132-139] the related technique of liquid phase deposition,[140] and multi-target magnetron sputtering deposition.[141, 142] Also, chemical vapour deposition

using a separate precursor for each phase (one of the methods reported in this thesis) falls into this category.[143, 144]

- Route 4 is the layer by layer deposition of metal particles and semiconductor material, for example laser ablation using alternate metal and semiconductor targets.[145]
- Route 5 is the one step deposition of pre-formed particles and semiconductor coating from a precursor chemical. Depositions of this type are described in this thesis.

1.7 CVD of Gold and Nanocomposite Films

CVD of metallic gold films has been carried out using a variety of precursors (see table 1.3). All the precursors shown in table 1.3 are organometallic gold(I) or gold(III) complexes. The majority of these depositions have been carried out at reduced pressure, due to the relatively low volatility of the gold compounds used. Only $MeAuP(Me)_3$ has been used in conventional atmospheric pressure CVD with a heated substrate, although in this case the substrate was pre-coated with a layer of Pd which catalysed the deposition of Au.[146] Carbon contamination can also be a problem with many of the gold precursors shown in table 1.3. This is likely due to the Au-C bond in the majority of these compounds. A third issue with some of these precursors is photosensitivity and thermal instability, which means they have to be stored in the dark at reduced temperatures.

Most investigations into the CVD of gold have been focused on depositing gold for microelectronics applications.[38] For this reason, particular attention has been paid to deposition of films which are patterned on the micron and millimetre scale; laser assisted CVD has been used to create intricate micron scaled patterns of gold.[149, 150, 156]

Precursor	Precursor stability	Precursor vapour pressure (24°C) / Pa	CVD variant	Total reactor pressure / Pa	Deposition temperature / °C	Comments	References
$MeAuP(OMe)_2R$	TU	*a*	LP	100	100 - 125	Needle like and column growth observed	1
$Me_2Au(acac)$	TU	1	LP	70	300	Grainy surface texture, some C contamination	147, 148
			LA	1×10^5	25	Laser power 4.0×10^5 W cm^{-2} used	149, 150
			LP	0.4	200	Gold particles deposited on TiO_2 substrates	148, 151
$Me_2Au(hfac)$	TU	53	LP	70	300	Use of fluorinated ligands leads to lower carbon contamination	147
			LA	50	20	Laser power 0.75W	152
$CF_3AuCNMe$	PS	*a*	LP	1	260	-	153
$MeAuP(Me)_3$	-	*a*	AP	1×10^5	85	Pd coated substrate catalyses low temperature deposition	146
			LP	7×10^{-7}	350	UHV deposition on Si substrates	154
$R^1CO_2AuP(R^2)_3$ $R^1 = C_2F_5, C_3F_7$ R^2 = Me, Et, Ph	-	*a*	LP	400	250	-	155

Table 1.3. Precursors used in the CVD of gold. LP = low pressure, LA = laser assisted, AP = atmospheric pressure, TU = thermally unstable at room temperature, PS = photo-sensitive to visible light. *a*: not reported

Perhaps because of the concentration of gold CVD research on patterned microelectronics, the optical properties of gold films deposited by CVD are rarely reported. Correspondingly, while the structure at the micron and millimetre scale are often reported in detail, the nanostructure of CVD gold films, which will strongly influence the optical properties, has seldom been investigated. One exception is the work of Puddephatt and Au, who deposited gold films onto a substrate pre-coated with polymer spheres, which themselves were coated with a Pd catalyst layer.[146] The polymer templates were removed by pyrolysis, leaving a macroporous gold film. The optical properties of these films were not reported.

While the deposition of gold by CVD has a relatively strong precedence in the literature, as shown by table 1.3, there are very few reports of the use of CVD to deposit gold / semiconductor nanocomposites. The closest to a precedent is the work of Feurer and Suhr, who used plasma enhanced CVD to deposit coatings of gold within an organic polymer matrix.[157] They used $Me_2Au(acac)$ and propylene as precursors under reduced pressure. In some cases the films were reported as blue in colour, suggesting a SPR absorption, although this was not directly measured. Gold oxide films could also be produced by the addition of O_2 to the reactor. All reports of the deposition of a metal / semiconductor composite use a two step process. For example, D. H. Kim *et al.* reported the deposition of Au : TiO_2 films by first spin coating a gold precursor onto a substrate, followed by APCVD using $TiCl_4$ to deposit TiO_2.[158] The CVD process simultaneously converted the gold precursors to gold particles. Kodas *et al.* used CVD to infiltrate preformed layers of nanoparticles, forming a composite film.[159] Silica particles were spin coated onto a substrate, which was then used for the deposition of a Cu film. A variety of particle sizes were investigated; it was found that larger particles, around 500 nm, allowed better infiltration of the CVD vapour leading to a more adherent film. Particles smaller than 180 nm could not be used due to poor infiltration. In a separate study, Okumura *et al.* deposited gold particles onto metal oxide substrates (TiO_2 and SiO_2) via CVD using $Me_2Au(acac)$.[148, 151] These outside cluster composites were used as CO oxidation catalysts. This was the only report that could be found of the CVD of gold where the size distributions of the gold particles were measured. The size distributions had arithmetic means (μ) and standard deviations (σ) ranging from $\mu = 3.5$ nm, $\sigma = 2.7$ nm to $\mu = 6.6$ nm, $\sigma = 3.8$ nm.

1.8 Conclusions

Gold thin films and nanocomposites are of interest due to their size dependent properties which may lead to important technological applications. These applications will likely require deposition technology that combines good control of the film nanostructure with ability to integrate into existing fabrication technologies and coat a variety of substrates. Gold films have been produced by such techniques as electrospray deposition, sol-gel, sputtering and liquid phase deposition. The dependence of the optical properties of gold films on their structure is complex. Factors such as film thickness, particle size and particle separation are important, although these factors can be difficult to control in most deposition processes. CVD of gold films has been reported, using organo-gold precursors with moderate volatility. Low pressure techniques are generally used for these depositions. These CVD studies have primarily been concerned with depositing films patterned on the micron scale for use in electronics, and hence film purity and conductivity are chief concerns in these works. As such, no detailed study of the optical properties of CVD gold films has been made.

[$HAuCl_4$] has been extensively used to produce gold nanoparticles in solution. It has also been investigated as a SAT precursor to gold particles, formed by the evaporation of aerosol particles in a furnace. It is unsuitable for conventional CVD as it is involatile and decomposes at a relatively low temperature. Very few depositions of gold / semiconductor nanocomposites have been made using CVD, despite the generally high research interest in such materials. None of the previously reported CVD syntheses of gold / semiconductor nanocomposites use a single step process.

The following chapters present the results of the investigation into deposition of gold by AACVD. In Chapter 2 the AACVD experimental setup is described, and the various analytical techniques introduced and discussed. Chapter 3 presents results on the deposition of gold films from [$HAuCl_4$] and pre-formed gold nanoparticles. Chapter 4 presents results on the deposition of gold / semiconductor nanocomposite films from a combination of the novel gold precursors and conventional transition metal oxide CVD precursors.

Chapter 2: Experimental Section

2.1 Introduction

This chapter describes the experimental methods used to deposit coating by AACVD. The analytical techniques used to characterise the films are also described, and their theoretical basis discussed.

2.2 Aerosol Assisted CVD

Aerosol assisted CVD was carried out using a horizontal bed reactor of in-house design. Figure 2.1 shows the main features, which are further described below.

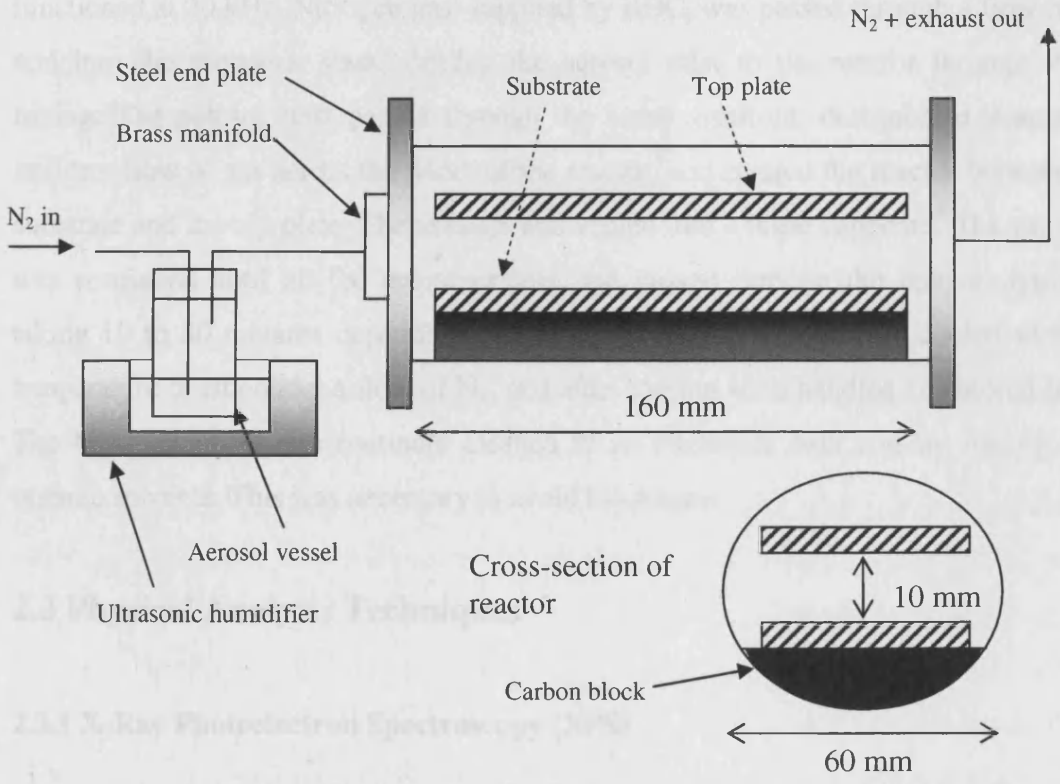

Figure 2.1 Schematic of the apparatus used for aerosol assisted CVD.

The reactor consisted of an open ended quartz cylindrical tube, 60 mm in diameter and 160 mm in length. Within the tube were supports for a top plate and a carbon block containing a heating element and two thermocouples. Each end of the quartz tube was capped with a removable stainless steel end plate. Gas may enter through one of the

plates via brass manifold, and leave at the opposite end via an exhaust port. The substrate was placed on the carbon block, and a top plate was placed parallel to the substrate and 10 mm above it.

Both the substrate and top plate were 150 x 45 x 4 mm sheets of SiO_2 coated float glass cut from larger sheets supplied by Pilkington Glass Plc, which were cleaned using acetone and propan-2-ol and then dried in air prior to use. The substrate was placed on top of the carbon heating block at room temperature. The reactor was then sealed and heated to the desired temperature. Only the substrate was directly heated, hence the reactor is known as a cold wall reactor.

The precursor solution was contained within a glass vessel with a thinned base, which allowed more rapid aerosol generation. A Vicks ultrasonic humidifier was used to generate the aerosol mist. The piezoelectric device contained within the humidifier functioned at 20 kHz. Nitrogen gas, supplied by BOC, was passed through a flow meter and into the precursor flask, driving the aerosol mist to the reactor through PTFE tubing. The aerosol mist passed through the brass manifold, designed to generate a uniform flow of gas across the width of the reactor, and entered the reactor between the substrate and the top plate. The exhaust was vented into a fume cupboard. The gas flow was continued until all the precursor mix had passed through the reactor, typically taking 10 to 30 minutes depending on the gas flow rate. Films were cooled to room temperature *in situ* under a flow of N_2, and after cooling were handled and stored in air. The brass manifold was routinely cleaned in an ultrasonic bath and by rinsing with organic solvents. This was necessary to avoid blockages.

2.3 Physical Analysis Techniques

2.3.1 X-Ray Photoelectron Spectroscopy (XPS)

XPS is an analysis technique in which X-rays are used to eject photoelectrons from a sample, which are then analysed to determine their kinetic energies.[160] The kinetic energies of the electrons can be related to the binding energy of the electron within the original atom by the equation:

$$BE = E - KE - \phi \qquad (2.1)$$

In equation 2.1, *BE* is the binding energy of the electron before ionisation, *E* is the photon energy of the incident light, *KE* is the measured kinetic energy of the photoelectron, and ϕ is the work function of the XPS spectrometer, which is a constant calibrated for each instrument. The photon energies, E, used in XPS are high enough to excite core electrons. Although valence electrons are also excited, XPS is usually used to observe core photoelectrons.

XPS is used to obtain oxidation state, chemical environment information and quantification for elements within a sample. Photoelectron spectra are constructed by plotting the photoelectron binding energy against the measured intensity, and photoelectron peaks are assigned to different core atomic orbitals of different elements depending on their binding energy. Photoelectrons arising from an *s* orbital, *i.e.* an orbital with angular momentum quantum number, $\ell = 0$, give one peak, or a singlet. Photoelectrons arising from any other orbitals, where $\ell > 0$, result in two peaks, or a doublet, due to spin orbit coupling. Because the mean free path of the photoelectrons is very short, only those emanating from near to the surface of the sample escape and are detected. Hence XPS is a highly surface specific technique.

The position of a photoelectron peak is determined by the electron binding energy. This in turn is affected by the chemical environment of the element; for example an element present as a cation will have its photoelectron peaks shifted to higher binding energies than the same element present as an anion. The intensity of a photoelectron peak is dependent on the amount of the element in the analysis area, the ionisation cross section of the atomic orbital and instrumental factors. Elemental quantification is carried out by comparing relative intensities of photoelectron peaks, and as instrumental contributions to peak intensity will be the same for each peak, they can be ignored. In contrast, the ionisation cross section is different for each orbital. Empirically derived sensitivity factors are available for a great many atomic orbitals, and these are used to account for variation in ionisation cross section. Since photoelectrons are excited from quantised atomic orbitals, a simple model would predict photoelectrons at only one energy. In reality, photoelectron peaks with a finite width are observed. The width of photoelectron peaks is determined by the lifetime of the excited atomic energy level, according to the uncertainty principle. This 'natural' peak broadening results in a Lorentzian peak shape. Instrumental factors also cause peak broadening, such as X-ray line shape, thermal

broadening, and instrumental resolution. These result in a Gaussian peak shape. To accommodate these two influences on peak width, photoelectron peaks are usually fitted with a convolution of a Gaussian and Lorentzian function, known as a Gaussian-Lorentzian fit.[160] Because peaks can often overlap, especially where more than one chemical environment of a particular element is present, peak fitting is often required for accurate quantification.

XPS was carried out using an ESCALAB 220i XL instrument. Monochromated Al $K\alpha_1$ X-rays (E = 1486 eV) were used to eject electrons from the samples. X-rays were generated using a cathode voltage of 7.5 kV and a current of 10 mA. Photoelectrons were focussed using a magnetic lens and resolved using a hemispherical analyser equipped with six detector channels. A pass energy of 150 eV was used for low resolution survey scans and 20 eV was used for high resolution, narrow interval scans. The latter were used for all quantification and peak fitting operations. Areas of each sample to be analysed were cut to squares around 10 mm in size and mounted on stainless steel supports. An aluminium mask was placed over the sample, with a circular 3 mm hole through which the analysis was performed. The purpose of the mask was to reduce charging of the sample by forming an electrical contact between the analysed area and the instrument. The analysis area was around 1 mm in diameter. The analysis depth varies with photoelectron energy, but is expected to be around 10 Å.[160] An electron flood gun was used to reduce sample charging. The instrument was controlled and data collected using the Eclipse software suite. Binding energies were referenced to surface elemental carbon 1s peak with binding energy 284.6 eV in order to compensate for the effects of charging. Peak fitting was performed using the CasaXPS software. Quantification was carried out using peak areas and empirically derived elemental sensitivity factors taken from previous studies.[160]

2.3.2 Powder X-Ray Diffraction (XRD)

Light is diffracted from a set of periodic planes according to the Bragg equation. The distance between Miller planes in crystalline materials is of the order of 10^{-10} m, therefore the wavelength of light which is diffracted from these planes corresponds to X-rays. Powder XRD is performed on polycrystalline powders or films, and gives information on the crystalline phases present, preferred orientation of the crystallites and crystallite size.[161] The intensity of a diffraction peak arising from a particular set of

Miller planes of crystalline phase A, $I_A(h,k,l)$ is dependent upon the structure factor of A, $F_A(h,k,l)$, and the molar amount of A present in the illuminated volume, α_A, as shown in equation 2.2.

$$I_A(h,k,l) \propto \alpha_A F_A(h,k,l)^2 \qquad (2.2)$$

Powder XRD was undertaken using a Bruker-Axs D8 (GADDS) diffractometer. This instrument uses a 2D area X-ray detector to record large sections of multiple Debye-Scherrer cones simultaneously. After collection, the data can be integrated to produce a standard one-dimensional diffractogram. The instrument uses a Cu Kα X-ray source which is collimated such that only a small area of the sample (approximately 4 mm^2) is illuminated by the beam at any one time. This allows several small spots on the film to be analysed separately. A motorised computer controlled sample stage allows accurate positioning of the sample, and this was used to record diffraction patterns from points at regular intervals along a sample. To record diffraction peaks from the thin films, a fixed incidence angle of 5° was used.

In this thesis a simple method of quantifying the molar amount of gold present at a particular point in a sample using powder XRD data is used. A diffraction pattern was obtained using identical experimental parameters in each case: incident angle 5°, detector angle 30°, collection time 600 s, cathode current 40 mA, potential difference 40 kV. The Au [111] peak, appearing at a 2θ value of around 38.3°, was then integrated using a linear baseline to obtain the peak intensity. Since the structure factor and experimental parameters are the same in each case, this intensity is dependent only on the molar amount of crystalline gold within the illuminated volume. This technique is based on the assumption that the gold is present in crystallite sizes detectable by powder-XRD. It has been reported that gold crystallites as small as 3.0 nm give well resolved powder XRD peaks, indicating that this method should be applicable to even nanocrystalline gold films.[95] As a reference, a flat ingot of 91 % Au, around 3 mm thick, was subjected to XRD analysis using the parameters stated. The integrated Au [111] peak area of this sample was 40.6 CPS × degrees. This reading represents the upper limit of this XRD quantification technique. None of the films analysed in this work reached above 60% of this maximum value.

2.3.3 UV / visible / near IR Absorption Spectroscopy

The absorption of UV, visible and near infra red light is an important property of nanoscale gold, hence the recording of absorption spectra was an important characterisation technique. Spectra were obtained using a Thermo Helios-α spectrometer with a resolution of 1 nm and a range of 200 – 1100 nm.

2.3.4 Scanning Electron Microscopy (SEM)

SEM is an electron imaging technique used to record high resolution images of the sample surface. A high energy electron beam is focussed onto the sample surface. Electrons emanating from the sample are collected; these can be divided into two types depending on their origin: backscattered electrons and secondary electrons. Backscattered electrons are incident electrons which have undergone elastic or inelastic scattering from the sample surface. The kinetic energy of backscattered electrons is usually lower than that of the incident electron beam due to one or more inelastic scattering events. The intensity of backscattered electrons depends strongly on atomic number, as scattering is more likely to occur from regions of high electron density. Regions with high electron density will backscatter more electrons, and so will appear brighter in backscattered electron images. For this reason, backscattered electron images, also known as compositional images, can be used to distinguish different elements or phases within composite materials.

Secondary electrons are electrons ejected from the sample by the high energy incident electrons. The kinetic energy of secondary electrons is usually much lower than that of backscattered electrons, and this energy difference is the primary method of distinguishing the two types of electron emission. Because of their low kinetic energy, secondary electrons are easily recaptured by ionised atoms within the sample. Therefore secondary electrons escape only from the surface region of the sample. Secondary electron emission is strongly dependent on the surface morphology; highly curved or angled surfaces appear brighter in secondary electron images.

SEM analysis was performed on a JEOL 6301F instrument using voltages between 6 and 15 kV, at 8 μA. Images were recorded and analysed using the SEMAfore software. Samples were coated prior to analysis to enhance conductivity and reduce charging,

which causes image distortion. A coating of gold is usually used for this purpose, but it was found that the application of a gold coating significantly changed the morphology of the gold films being observed. Therefore a carbon coating was applied to the film surface. Additionally, samples were coated with a thick layer of gold on the reverse, using a sputter coater, to achieve a good electrical contact with the sample stage. Samples were placed on a stainless steel stage. For several films, images were recorded at specific intervals along the substrate. To facilitate this, the film was cut into strips approximately 30 mm in length and 5 mm in width. Images were taken at different positions by moving the samples within the instrument; the position could be determined with an accuracy of 0.1 mm in this way.

2.3.5 Thermal Gravimetric Analysis (TGA)

Thermal gravimetric analysis is a technique used to investigate the thermal decomposition of chemicals, and hence is a useful tool for characterising CVD precursors. A sample of the precursor of known mass was placed on a balance and heated in an inert atmosphere. The temperature was increased at a rate of 10 K min^{-1} and changes in mass were recorded. TGA was carried out on [$HAuCl_4$] using a NETZCH STA-449C instrument.

Chapter 3: Deposition of Gold Films

3.1 Introduction

This chapter describes the deposition of thin films of gold and gold nanoparticles and their optical properties. Gold films were deposited using two categories of precursors; firstly, hydrogen tetrachloroaurate, [$HAuCl_4$], as a single source precursor and in conjunction with a variety of surfactants, and secondly, pre-formed gold particles in toluene.

3.2 Precursors

3.2.1 [$HAuCl_4$]

Hydrogen tetracholroaurate, [$HAuCl_4$], also known as chloroauric acid, is an orange solid, which was obtained from Aldrich Chemical Company as the trihydrate ($HAuCl_4.3H_2O$, 99.999%) and used as received. It is soluble in polar solvents, and decomposes on heating at around 175°C according to the following reaction:

$$HAuCl_4 \rightarrow Au + HCl + {}^3/_2Cl_2$$

The decomposition of a molecule to form a desired solid product with only gaseous by-products is a desirable attribute for a CVD precursor. However, the low decomposition temperature makes [$HAuCl_4$] unsuitable for APCVD, where the precursor is thermally vaporised. Its solubility in a wide range of solvents, however, makes it an attractive precursor for AACVD.

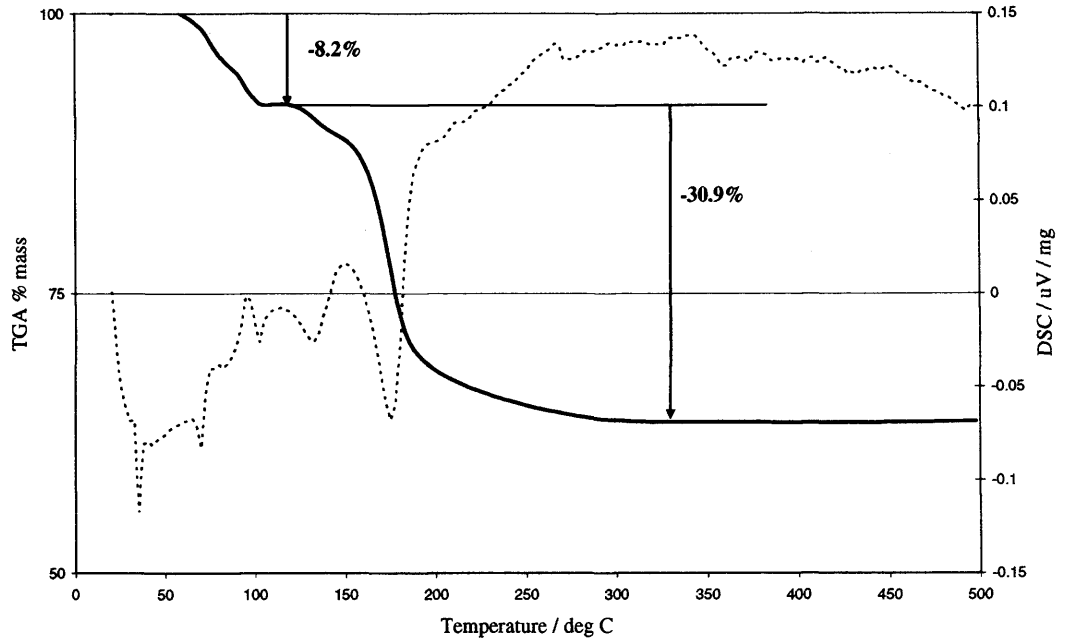

Figure 3.1. Thermal decomposition of [$HAuCl_4$]. The TGA trace (left axis) shows two main mass losses. The DSC trace (right axis) indicates that both mass losses are accompanied by exotherms.

Figure 3.1 shows the TGA/DSC of [$HAuCl_4$]. Two separate steps can be tentatively identified in the decomposition; the first between 60 and 110°C represents a mass loss of 8.2%, close to the expected mass change for the loss of HCl (10.7%). The second step occurred between 150°C and 200°C, and represents a mass loss of 30.9%, very close to the expected change on loss of $^3/_2Cl_2$ (31.3%). The mass was constant after 300°C, and the total mass loss correlates well with the decomposition of the precursor to metallic gold. The complex set of exothermic peaks in the DSC trace accompanying the decomposition suggest that the reaction is more complex than the simple two step process that has been outlined. There is a prominent exotherm at 175°C, corresponding to the final mass loss. The reaction might be broken down into the following steps based on the TGA results:

$$HAuCl_4 \rightarrow AuCl_3 + HCl$$

$$AuCl_3 \rightarrow Au + {}^3/_2Cl_2$$

However, pure $AuCl_3$ decomposes at a considerably higher temperature (420°C), perhaps suggesting a more complex decomposition.

3.2.2 Gold Colloids

Gold colloids were prepared in toluene solution using a modified Brust-Schriffin method.[82] [$HAuCl_4.3H_2O$] (0.17 g, 0.37 mmol) was dissolved in distilled water (15 mL). Tetraoctyl ammonium bromide (TOAB) (1.04 g, 1.9 mmol) was dissolved in toluene (40 mL). The two solutions were added to a beaker and stirred rapidly for 5 minutes. The organic phase became dark orange in colour, while the aqueous phase became colourless, indicating transfer of the Au^{3+} ions to the organic phase. The aqueous phase was discarded. $NaBH_4$ (0.19 g, 50 mmol) was dissolved in distilled water (25 mL) and immediately added dropwise to the organic Au^{3+} solution. The solution was vigorously stirred during the addition. After approximately 5 mL of borohydride solution had been added, the organic solution turned colourless, followed by the slow development of a dark red colour. After the addition of borohydride was complete, the solution was strirred for 10 minutes to ensure completion of the reaction. The aqueous phase was separated and discarded. The dark red organic phase was washed with one portion of dilute aqueous H_2SO_4 (10 mL) followed by three portions of distilled water (50 mL). The organic phase was topped up to 40 mL with toluene, then dried over anhydrous Na_2SO_3 for 1 hour and then filtered. The resulting very dark red solution was placed into glass sample tubes and stored at -18°C. Figure 3.2 shows the UV / visible spectrum of the gold nanoparticles in toluene. In order to take the spectrum, a small sample of the solution was diluted to give a recordable transmission; the undiluted solution absorbed too strongly for a spectrum to be taken.

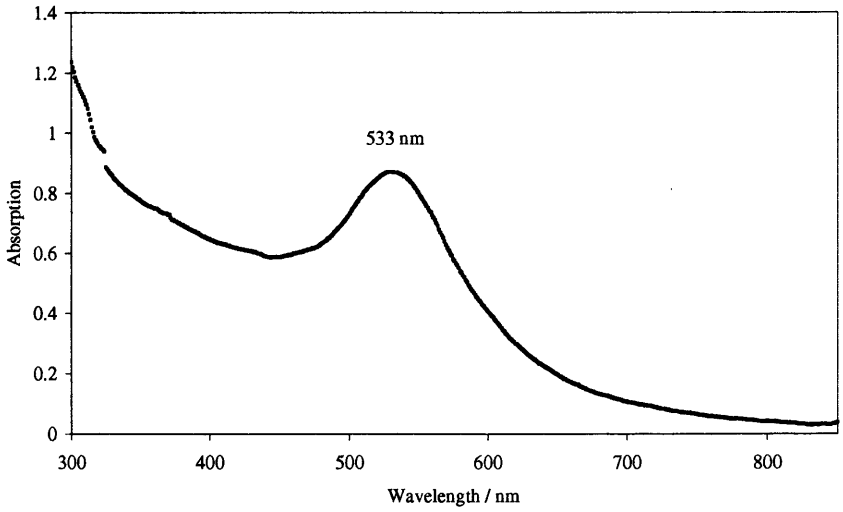

Figure 3.2. UV / visible spectrum of gold nanoparticles produced by a modified Brust-Schriffin synthesis in toluene.

3.3 Depositions using [$HAuCl_4$]

3.3.1 [$HAuCl_4$]

Depositions were carried out with the single source precursor [$HAuCl_4.3H_2O$]. In general, depositions using hydrogen tetrachloroaurate gave reproducible films at a wide range of temperatures and concentrations. Hydrogen tetrachloroaurate appears to be an excellent CVD precursor, which has, until now, been overlooked due to its poor volatility.

Initial investigations identified that good coverage of the substrate could be achieved using a precursor solution made up of [$HAuCl_4.3H_2O$] (0.080 g, 0.2 mmol) in methanol (50 mL) using a substrate temperature of 500°C and a flow rate of 2.0 L min^{-1}. The film deposited under these conditions appeared continuous, smooth, non powdery, and non-hazy. The first 70 – 80 mm of the substrate was coated. The colour of the film appeared to change when viewed in transmitted light (lit from the rear) or reflected light (lit from the front). The film was deep blue in transmission with a gold metallic lustre when viewed in reflected light. The last 5 mm of coating was pale pink in transmission and green in reflection. In the first 10 – 15 mm the coating appeared yellow-gold in colour, similar to bulk gold.

Powder XRD conducted at a glancing angle confirmed the presence of crystalline gold in the film. A typical diffraction pattern is shown in figure 3.3. Diffraction peaks can be seen corresponding to cubic Au [111] and [200] at 2θ values of 38.4° and 44.2° respectively ($\lambda = 1.540 \times 10^{-10}$ m).[133] These are the only cubic gold peaks expected to appear in the angle range that the diffraction patterns were taken. The very broad peak around 25° is due to the underlying amorphous SiO_2 substrate.

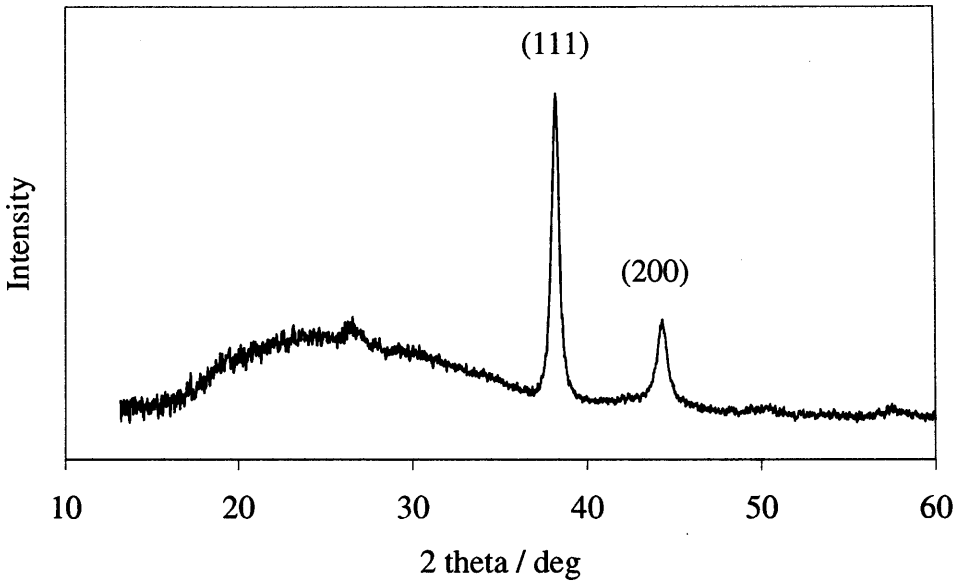

Figure 3.3. XRD pattern obtained from a gold film deposited on glass from [$HAuCl_4$]. The two sharp peaks are assigned to the (111) and (200) planes of cubic Au as indicated. No other diffraction peaks due to cubic Au are expected in the range of angles measured.

The small X-ray spot size and motorised stage associated with the XRD instrument (discussed in Chapter 2) allows powder XRD patterns from regular points along the sample to be taken. This technique has been proved useful in general for investigating the changing structure of CVD films along the length and width of the substrate.[162] In the case of gold films, the position, width and area of the Au [111] peak was measured at regular intervals along the substrate, starting from the end closest to the aerosol inlet. Identical experimental parameters were used for the collection of each diffraction pattern: an X-ray incident angle ($\theta 1$) of 5° and a detector angle ($\theta 2$) of 30° were used. Data was collected for a period of 600 s in each case. The Au [111] peak was integrated using a linear baseline to quantify the amount of crystalline gold present at each point. Since the area of the sample that is irradiated is the same in each case, the integrated peak area is proportional to amount of gold at each position, assuming that all the gold present is crystalline, a reasonable assumption for metallic gold. It has been reported that gold crystallites as small as 3.0 nm give well resolved powder XRD peaks, indicating that this method should be applicable to even nanocrystalline gold films.[95] Figure 3.4 shows the variation in integrated area and full width at half maximum (FWHM) of the Au [111] diffraction peak.

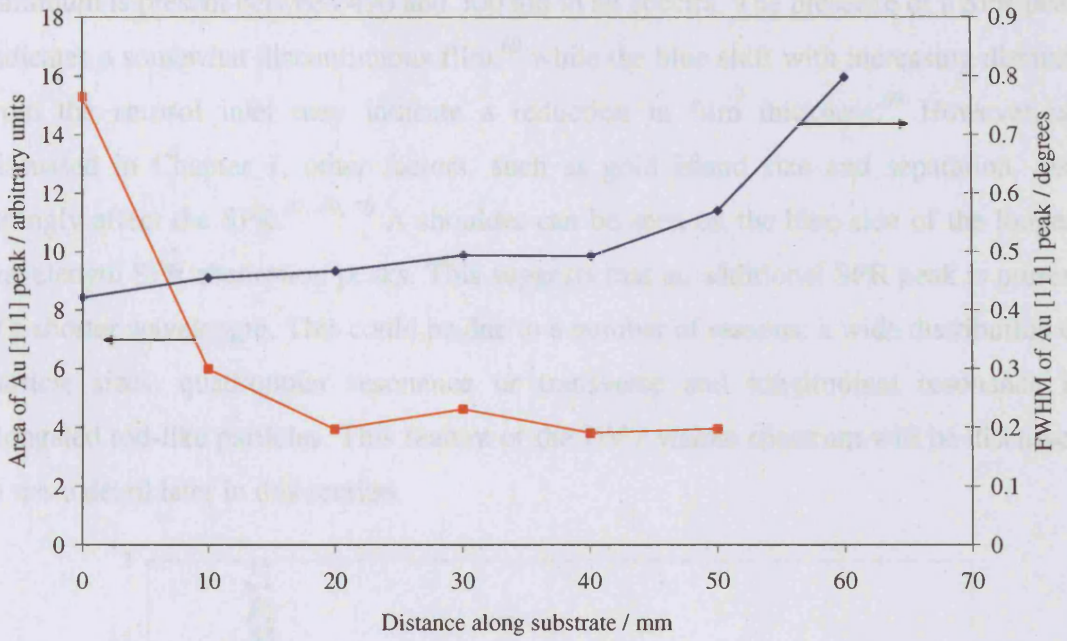

Figure 3.4. Variation in integrated area and FWHM of the Au [111] diffraction peak along the length of a gold film deposited from [$HAuCl_4$].

Two trends can be observed in figure 3.4. The integrated area of the Au [111] diffraction peak generally decreases along the length of the film, indicating (allowing for the assumptions stated above) that the rate of gold deposition falls moving away from the aerosol inlet. Secondly, the FWHM of the diffraction peak increases monotonically along the substrate length, indicating that the crystallite size decreases, ignoring strain effects. Scherrer analysis using the FWHM plotted in figure 3.3 showed that the crystallite size in the [111] direction varied from 20 nm at the front of the substrate to 11 nm at the rear. The position of the Au [111] peak varied between 2θ values of 38.26° and 38.32°, a total variation of 0.06°, along the length of the film. The cubic Au lattice constant was calculated from the positions of the [111] and [200] diffraction peaks as $a = 4.07$ Å, identical to that of bulk gold.

The optical properties of the film were investigated using UV / visible spectroscopy. Figure 3.5 shows spectra taken at regular intervals of distance along the substrate. At wavelengths shorter than 320 nm, the absorption is high due to the glass substrate. The remainder of the spectrum is dominated by the SPR absorption. At the front of the film, deposited nearest to the aerosol inlet, the SPR maximum is around 830 nm, with a shoulder around 550 nm. Moving along the substrate, the SPR maximum shifts to shorter wavelengths, reaching 630 nm at 55 mm from the aerosol inlet. An absorption

minimum is present between 490 and 500 nm in all spectra. The presence of a SPR peak indicates a somewhat discontinuous film,[69] while the blue shift with increasing distance from the aerosol inlet may indicate a reduction in film thickness.[69] However, as discussed in Chapter 1, other factors, such as gold island size and separation, also strongly affect the SPR.[67, 69, 70] A shoulder can be seen on the blue side of the longest wavelength SPR absorption peaks. This suggests that an additional SPR peak is present at a shorter wavelength. This could be due to a number of reasons: a wide distribution of particle sizes, quadropolar resonance or transverse and longitudinal resonance in elongated rod-like particles. This feature of the UV / visible spectrum will be discussed in more detail later in this section.

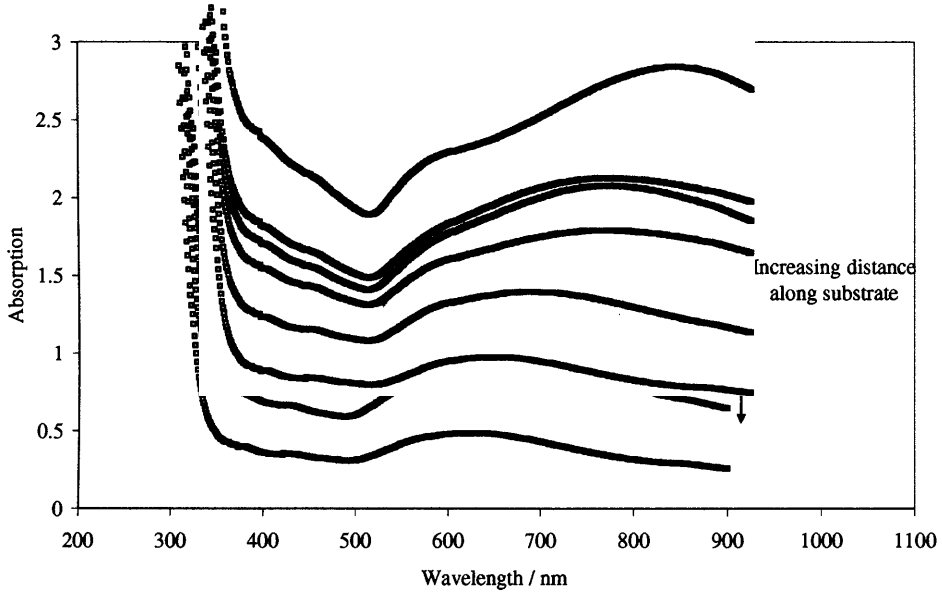

Figure 3.5. UV / visible absorption spectra of a film deposited from [$HAuCl_4$] on glass. Spectra were taken at 10 mm intervals along the film. The high absorption below λ = 330 nm is caused by the substrate. SPR absorption can be seen at varying positions in each spectrum.

Figure 3.6 shows the relationship between the crystallite size and the Au [111] peak area, determined from XRD data, and the SPR maximum at corresponding distances along the substrate. The crystallite size appears to have an approximately linear relationship with the SPR absorption maximum, while the area of the diffraction peak shows much less of a linear correlation.

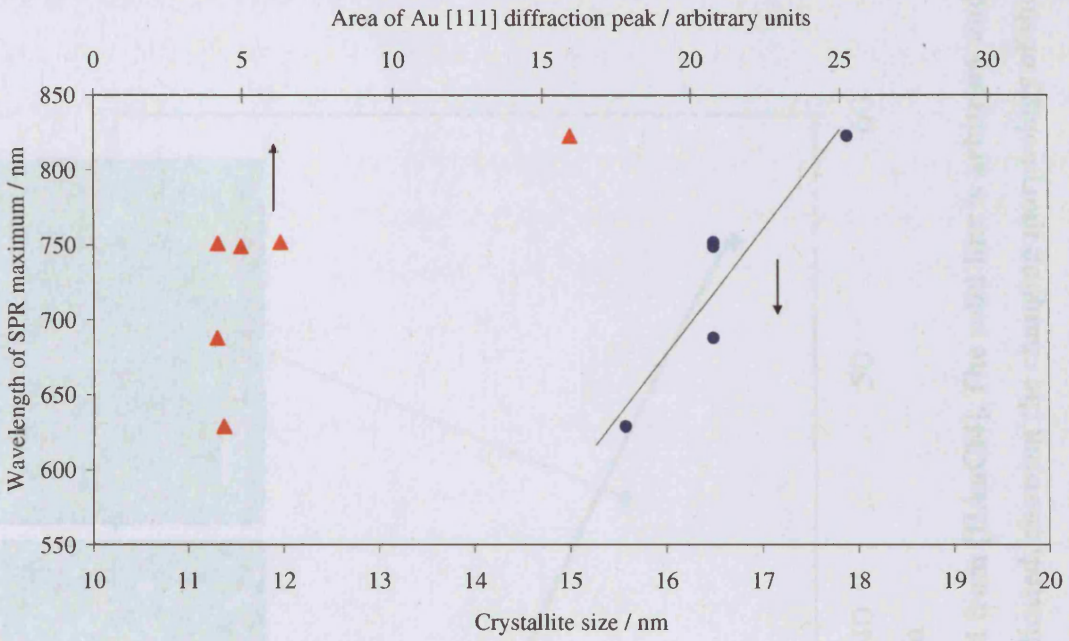

Figure 3.6. Graph showing the relationship between SPR absorption maximum determined by UV / vis spectroscopy and both the gold crystallite size (blue circles) and Au [111] diffraction peak area (red triangles). The dashed line is arbitrary and acts as a guide to the eye.

SEM imaging conducted in secondary electron mode revealed a changing morphology along the length of the film (figure 3.7). At the front of the film, the morphology appears highly particulate, with a wide range of particle size and shapes present, including elongated rods. Moving along the film, the particles become smaller and more widely spaced, and an underlying island-like morphology is revealed. SEM was also performed on cross sections of the film. The film thickness determined in this way was found to decrease monotonically from around 800 nm at 15 mm from the aerosol inlet to 120 nm at 45 mm from the aerosol inlet. The change in SPR absorption peak is likely to be affected by both the film thickness and the film microstructure. The shift of the SPR to shorter wavelengths is certainly consistent with a thinner film;[69] the effect of the changing film morphology cannot be directly determined, but may also contribute to the SPR blue shift.

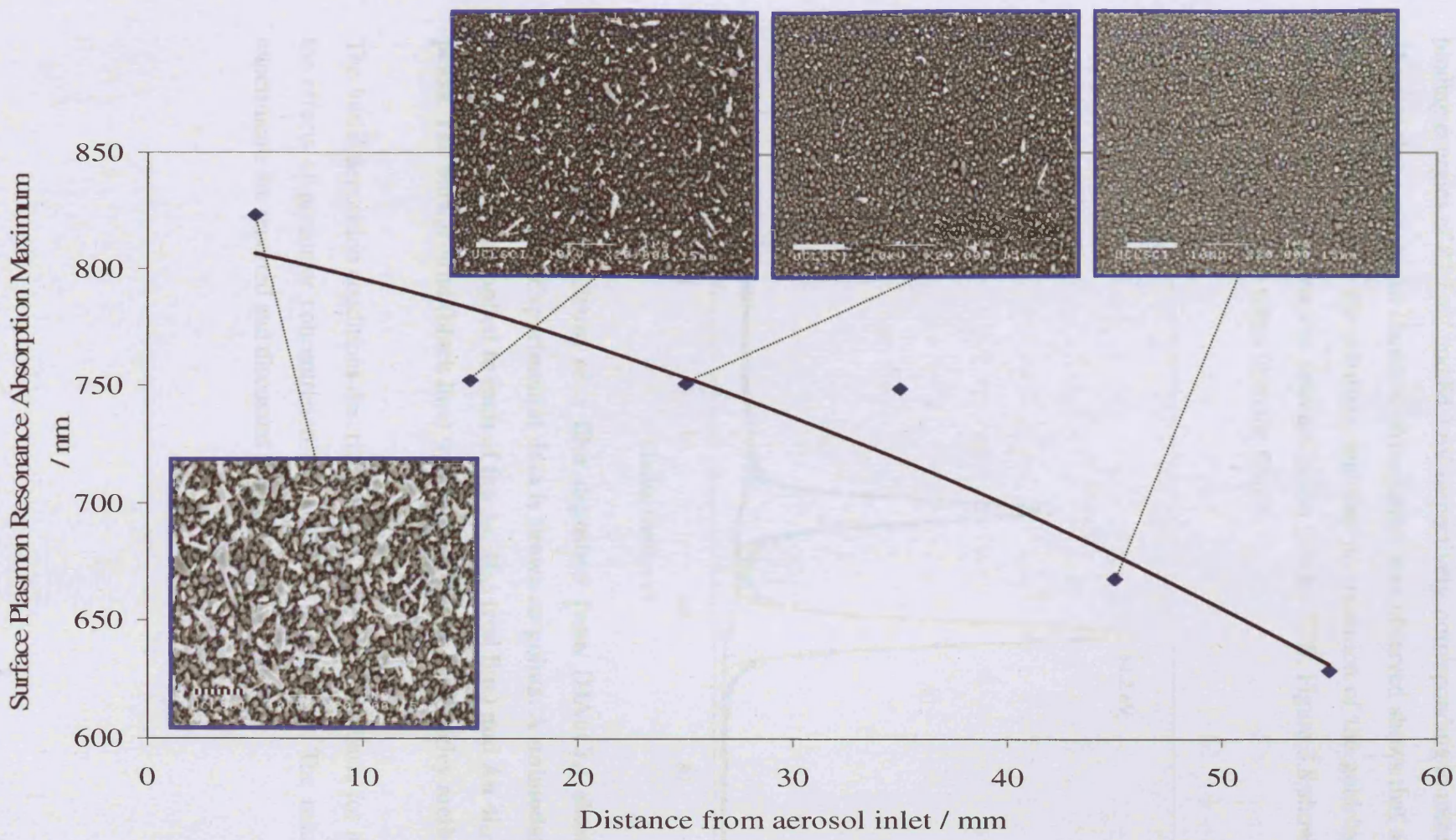

Figure 3.7. Variation in SPR absorption maximum along the length of a gold film deposited from [HAuCl4]. The solid line is arbitrary and acts as a guide to the eye. Inset: SEM (secondary electron) images taken at the positions indicated, showing the changing morphology of the film along its length. All images are at the same magnification; scale bars measure 1 μm.

XPS confirmed the presence of gold within the film. Au $4f_{5/2}$ and $4f_{7/2}$ photoelectron peaks were each fitted with a unimodal Gaussian-Lorentzian fit, with peak centres at binding energies of 87.7 eV and 84.2 eV respectively, corresponding to metallic gold.[163] The fact that a single Au chemical environment was observed shows that no unreacted precursor remained on the substrate, and that no oxidation of the gold had occurred. Additionally, no chlorine was detected in the film by XPS. Figure 3.8 shows the Au 4f photoelectron spectrum taken from the film.

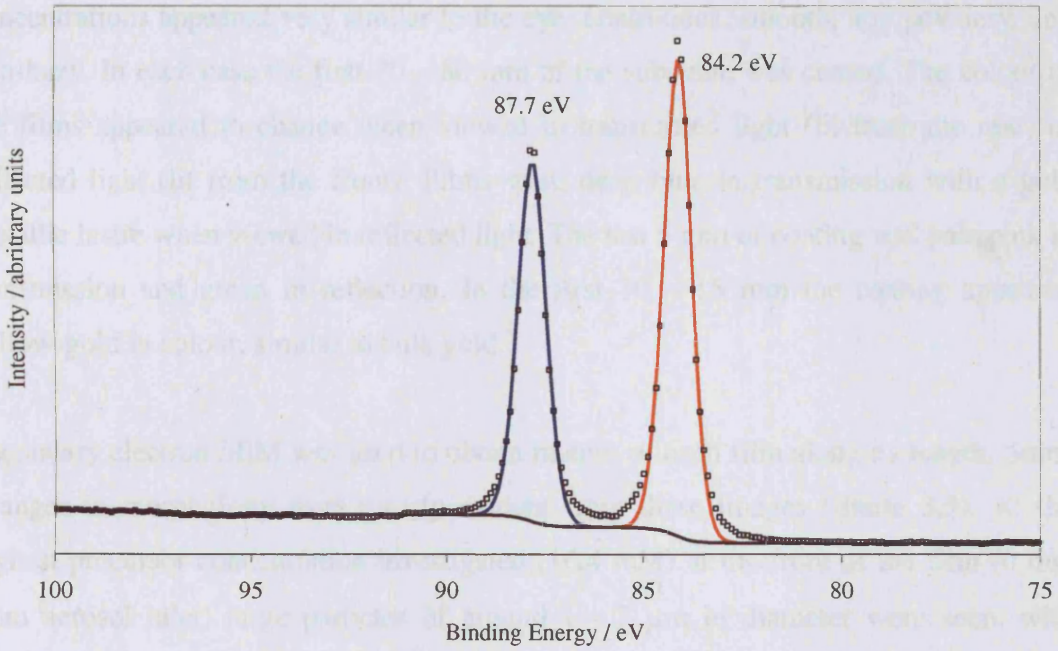

Figure 3.8. XPS spectrum of a film deposited from [$HAuCl_4$] showing Au 4f photoelectron peaks. Experimental data is shown as points. A unimodal Gaussian-Lorentzian fit were applied to each of the Au $4f_{7/2}$ (red line) and Au $4f_{5/2}$ (blue line) peaks. The background (black line) was determined by the Shirley method.

The initial deposition conditions described above were used as a basis for investigating the effects of precursor concentration and substrate temperature. The results of these experiments are reported and discussed below.

Precursor concentration

The precursor concentration was varied by changing the volume of solvent used, the total amount of [$HAuCl_4$] being kept constant at 0.080 g, 0.2 mmol. Depositions were carried out with 12.5, 25, 50, 100 and 200 mL of methanol (gold concentrations of 16.3, 8.1, 4.1, 2.0, 1.0 mM respectively). The initial case of 4.1 mM precursor solution has been discussed in detail above. All depositions were carried out at a substrate temperature of 500°C and a gas flow rate of 2.0 L min^{-1}. Films deposited at all concentrations appeared very similar to the eye: continuous, smooth, non powdery, and non-hazy. In each case the first 70 – 80 mm of the substrate was coated. The colour of the films appeared to change when viewed in transmitted light (lit from the rear) or reflected light (lit from the front). Films were deep blue in transmission with a gold metallic lustre when viewed in reflected light. The last 5 mm of coating was pale pink in transmission and green in reflection. In the first 10 – 15 mm the coating appeared yellow-gold in colour, similar to bulk gold.

Secondary electron SEM was used to obtain images of each film along its length. Some changes in morphology were clearly evident from these images (figure 3.9). At the highest precursor concentration investigated (16.4 mM) at the front of the film (0 mm from aerosol inlet) large particles of around 1 - 2 μm in diameter were seen, with irregular shape and size. Closer inspection showed that these large particles seem to be composed of smaller agglomerated or sintered particles. The particles were very closely spaced considering their diameters; typical spacing was around 50 nm. With greater distance from the aerosol inlet, the film morphology changed. Particle size decreased significantly to around 100 – 200 nm in diameter, although particle size and shape remained very irregular. At 20 mm from the aerosol inlet, the particle size decreased further. Some square shaped particles around 500 nm in size, and rod-like particles from 100 to 500 nm in length were visible.

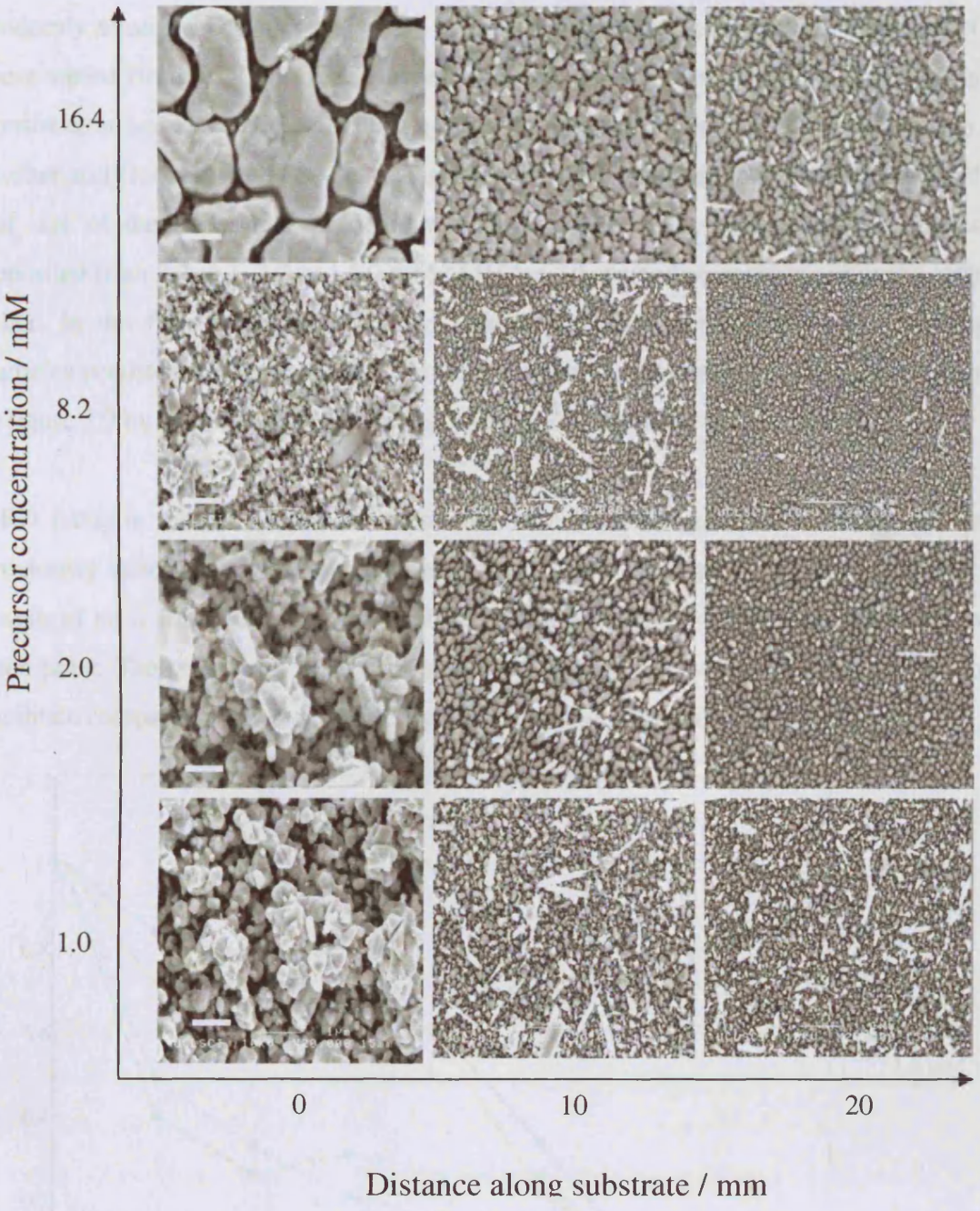

Figure 3.9: Secondary electron SEM images taken along the length of gold films deposited from various concentrations of [$HAuCl_4$]. All images were taken at the same magnification. Scale bars measure 1 μm. Images taken from the film deposited from a precursor concentration of 4.1 mM can be found in figure 3.7.

Decreasing precursor concentration had a significant effect on the film morphology. At concentrations below 16.4 mM, the morphology close to the aerosol inlet consisted of randomly arranged particles and rods, some showing facets and vertices. The size of these varied from 50 - 500 nm. Further from the aerosol inlet, the films appeared to consist of an underlayer of particulate gold, with long rod shaped particles lying on top. Further still from the aerosol inlet, the amount of rod-like particles became smaller, and the size of the underlying particles was also reduced. The morphologies of films deposited from 8.2, 4.1, 2.0 and 1.0 mM of [$HAuCl_4$] seemed reasonably similar to each other. In the film deposited from the lowest precursor concentration, the rod-like particles persisted further along the film length and in greater number. This can be seen in figure 3.9 by comparing the images taken at 20 mm from the aerosol inlet.

XRD patterns showed peaks corresponding to crystalline gold for all samples. As previously described, XRD measurements were taken at regular intervals along the length of each film. The Au [111] peak position, area and FWHM were measured at each point. The peak areas were normalised to the maximum value for each sample, to facilitate comparison between films. Figure 3.10 shows the result of this analysis.

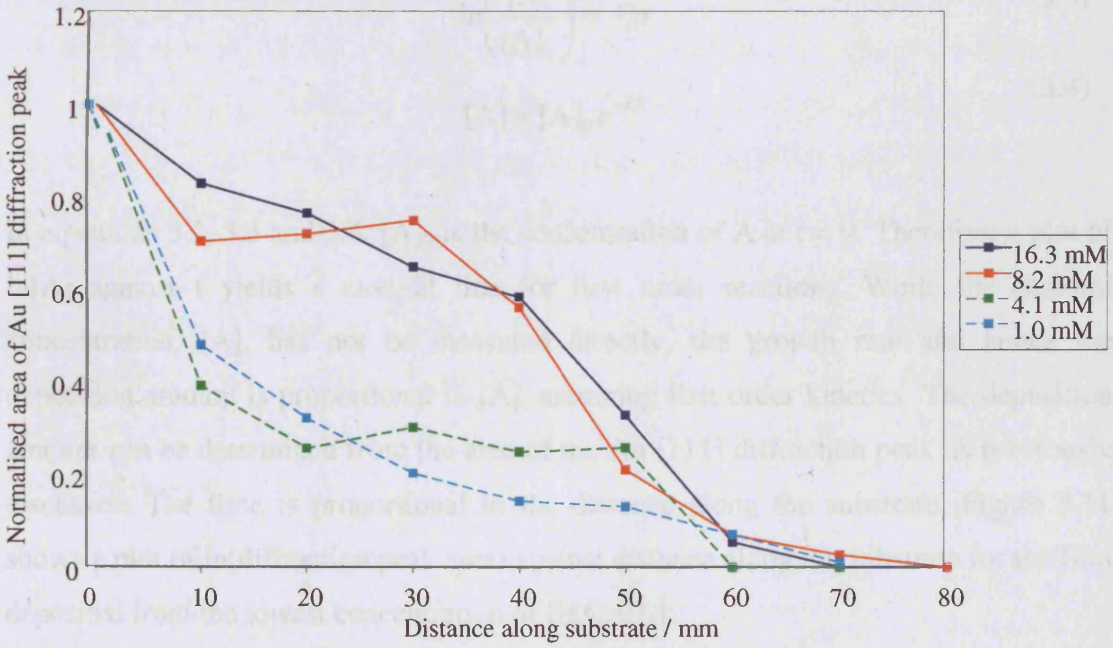

Figure 3.10 Integrated areas of Au [111] diffraction peaks, showing the variation in deposition with distance from the aerosol inlet. Data from four films are shown, deposited using different concentrations of [$HAuCl_4$], as indicated in the legend.

From figure 3.10 it is evident that deposition is greatest nearest to the aerosol inlet and generally decreases moving along the length of the substrate. Each film reaches zero integrated area at a distance of 60 - 80 mm from the aerosol inlet. At the lowest concentration (1.0 mM, light blue dashed line in figure 3.5) the measured peak area decreases monotonically. The change in film deposition along the length of the substrate resembles an exponential decay which would be expected in a first order reaction. If the deposition were a single step first order reaction, then the concentration of precursor is proportional to the rate of reaction. This is given by the first order rate equation:[164]

$$\frac{d[A]}{dt} = -k[A] \tag{3.1}$$

In equation 3.1, [A] is the concentration of precursor and k is the rate constant. The integrated form of the differential rate equation is:

$$\int_{[A]_0}^{[A]_t} \frac{d[A]}{[A]} = \int_0^t -k\,dt \tag{3.2}$$

$$\ln\left(\frac{[A]}{[A]_0}\right) = -kt \tag{3.3}$$

$$[A] = [A]_0 e^{-kt} \tag{3.4}$$

In equations 3.2, 3.3 and 3.4, $[A]_0$ is the concentration of A at t = 0. Therefore a plot of ln[A] against t yields a straight line for first order reactions. While the reactant concentration, [A], has not be measured directly, the growth rate and hence the deposition amount is proportional to [A], assuming first order kinetics. The deposition amount can be determined from the area of the Au [111] diffraction peak as previously discussed. The time is proportional to the distance along the substrate. Figure 3.11 shows a plot of ln(diffraction peak area) against distance along the substrate for the film deposited from the lowest concentration of $[HAuCl_4]$.

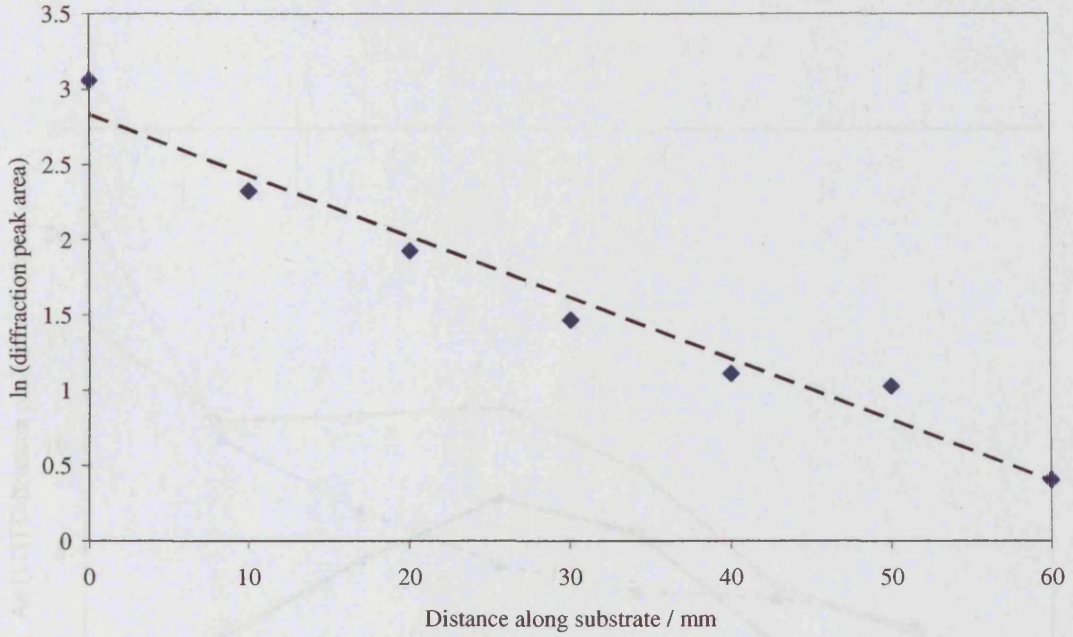

Figure 3.11 Plot of ln(diffraction peak area) against distance along substrate. The straight line indicates that this deposition can be modelled as a first order process.

The linear plot shown in figure 3.11 indicates that the deposition from low concentration of [$HAuCl_4$] can be modelled as a simple first order process. Similar plots to determine whether zero and second order rate equations were appropriate resulted in non-linear graphs. Films deposited from higher concentrations of [$HAuCl_4$] did not show a simple first order deposition rate. Figure 3.12 shows the XRD profile of a film deposited from a 8.2 mM solution of [$HAuCl_4$]. Also shown is the deposition profile of the film deposited from a 1.0 mM, and the difference between them. At higher concentration, there is additional deposition between 10 and 50 mm from the aerosol inlet, with a maximum at 30 mm. The origin of this deposition will be discussed in the following section.

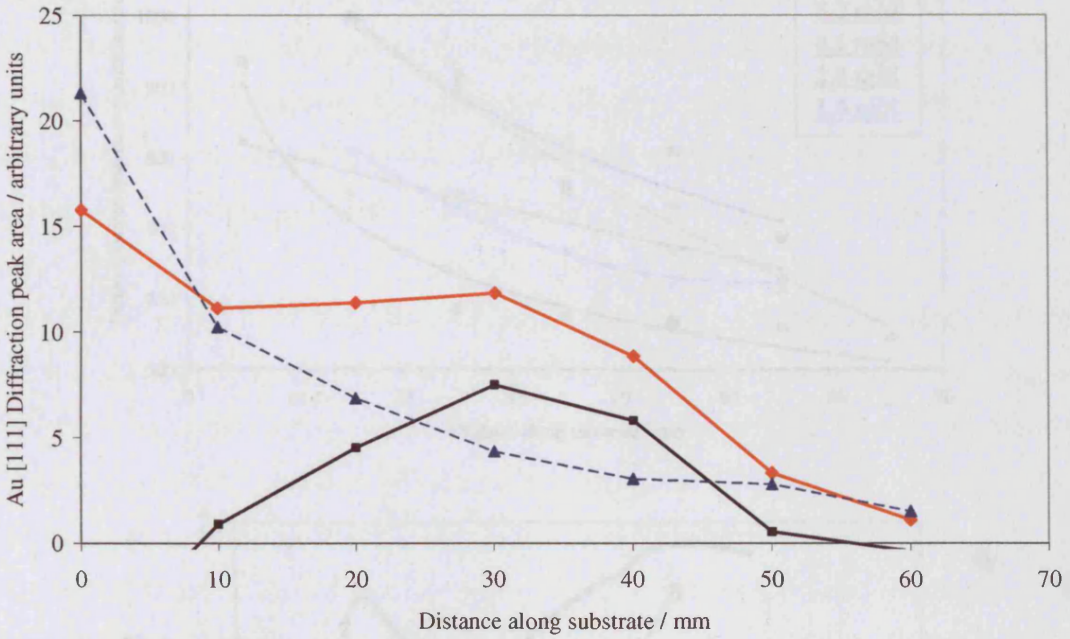

Figure 3.12. Deposition profiles of gold films deposited from 8.2 mM (red) and 1.0 mM (blue) solutions of [$HAuCl_4$]. The black line shows the difference in deposition profiles.

The optical properties of the films were studied using UV / visible absorption spectroscopy. As in the case of the initially investigated film, some regions showed two distinct SPR peaks. Figure 3.13, top, shows the change in SPR absorption maximum along the length of films deposited from varying concentrations of [$HAuCl_4$]; where two SPR peaks are present, the longer wavelength peak is used. In each film, the SPR was seen to blue-shift with increasing distance along the substrate. It can also be seen that in general, a blue-shift is observed moving from higher to lower precursor concentrations, although this is not the case for the 2.0 mM and 1.0 mM films.

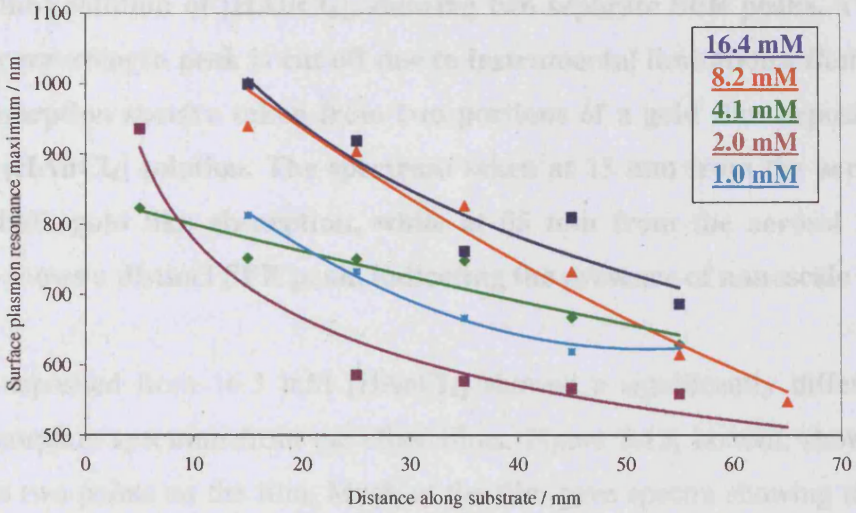

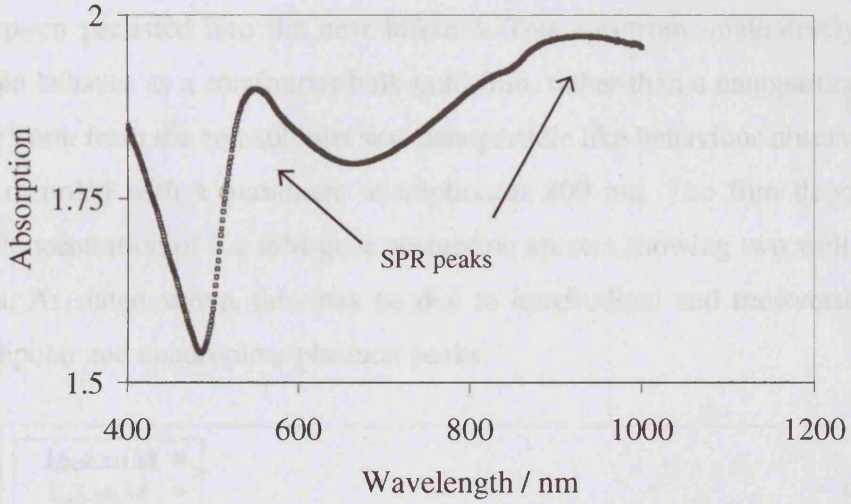

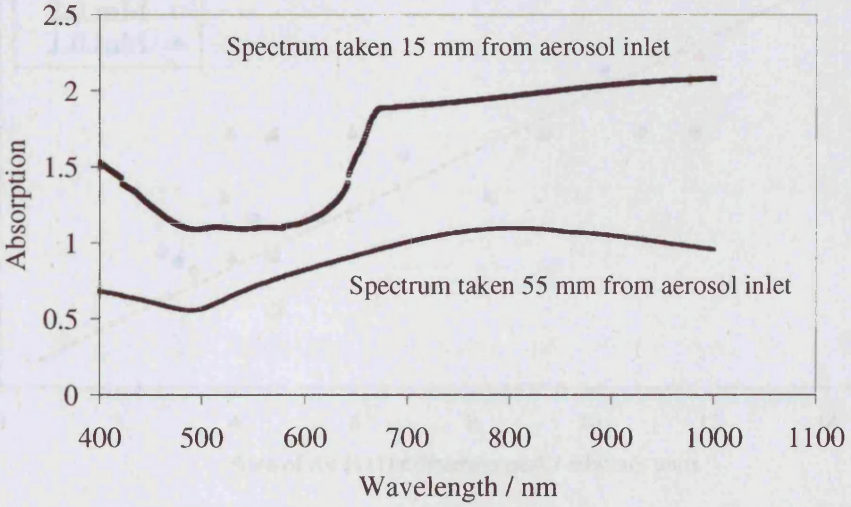

Figure 3.13. ***Top*****: Change in SPR absorption maxima along the length of films deposited from various concentrations of [$HAuCl_4$] in methanol. A coloured trend line is shown for data points for each sample. (continued overleaf)**

Figure 3.13 (continued) ***Centre*****: UV / visible absorption taken from a film deposited from 8.2 mM solution of [$HAuCl_4$], showing two separate SPR peaks. The tail of the higher wavelength peak is cut off due to instrumental limitations.** ***Bottom:*** **UV / visible absorption spectra taken from two portions of a gold film deposited from 16.3 mM [$HAuCl_4$] solution. The spectrum taken at 15 mm from the aerosol inlet shows a bulk gold like absorption, while at 55 mm from the aerosol inlet, the spectrum shows a distinct SPR peak, indicating the presence of nanoscale gold.**

The film deposited from 16.3 mM [$HAuCl_4$] showed a significantly different UV / visible absorption spectrum from the other films. Figure 3.13, bottom, shows spectra taken from two points on the film. Much of the film gave spectra showing no discreet SPR absorption, but rather a sharp increase in absorption a wavelength of 600 nm. This high absorption persisted into the near infrared. This spectrum qualitatively suggests that the gold behaves as a continuous bulk gold film, rather than a nanoparticulate film. Not until 55 mm from the aerosol inlet was nanoparticle like behaviour observed; a SPR peak was recorded with a maximum absorption at 800 nm. The film deposited at a precursor concentration of 8.2 mM gave absorption spectra showing two well separated SPR peaks. As stated above, this may be due to longitudinal and transverse plasmon peaks, or dipolar and quadroploar plasmon peaks.

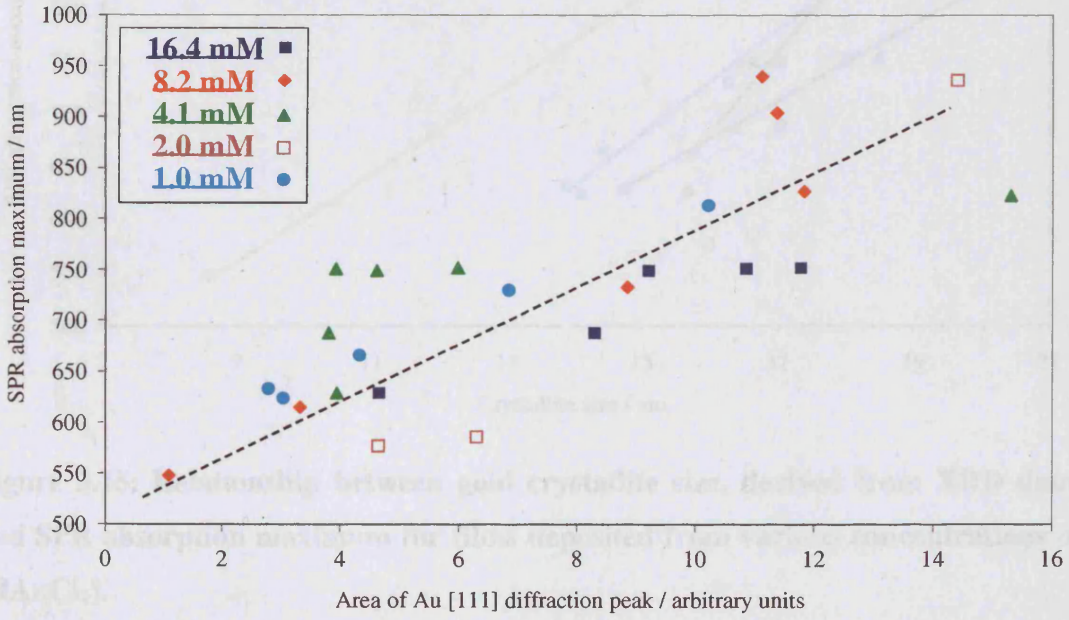

Figure 3.14. Relationship between Au [111] diffraction peak area and SPR absorption peak maximum (longest wavelength peak). Different coloured points refer to films deposited from different concentrations of precursor, as indicated. The dashed line is arbitrary and indicates the general trend of the data.

Figure 3.14 shows the relationship between the amount of crystalline gold at a specific position, determined by integrated Au [111] diffraction peak area, and the SPR absorption maximum at that position. There is a general upward trend, indicated by the dashed line, showing a red-shift in SPR absorption maximum with increasing amount of crystalline gold. In four of the five films examined (those deposited from 16.4, 8.2, 2.0 and 1.0 mM solutions of [$HAuCl_4$]) the trend appears close to linear. One film, that deposited from 4.1 mM (green points in figure 3.14) shows no strong correlation between peak area and SPR absorption maximum. Overall, the Au [111] peak area is a reasonably good predictor of SPR absorption maximum. This is, perhaps, surprising, given the extreme sensitivity of the SPR to film nanostructure, and the dependence of the diffraction peak area only on the amount of crystalline gold present. It seems that in this case, the nanostructures of the films were sufficiently similar that a measure of the amount of gold present also gave a reasonable approximation of the SPR absorption peak maximum.

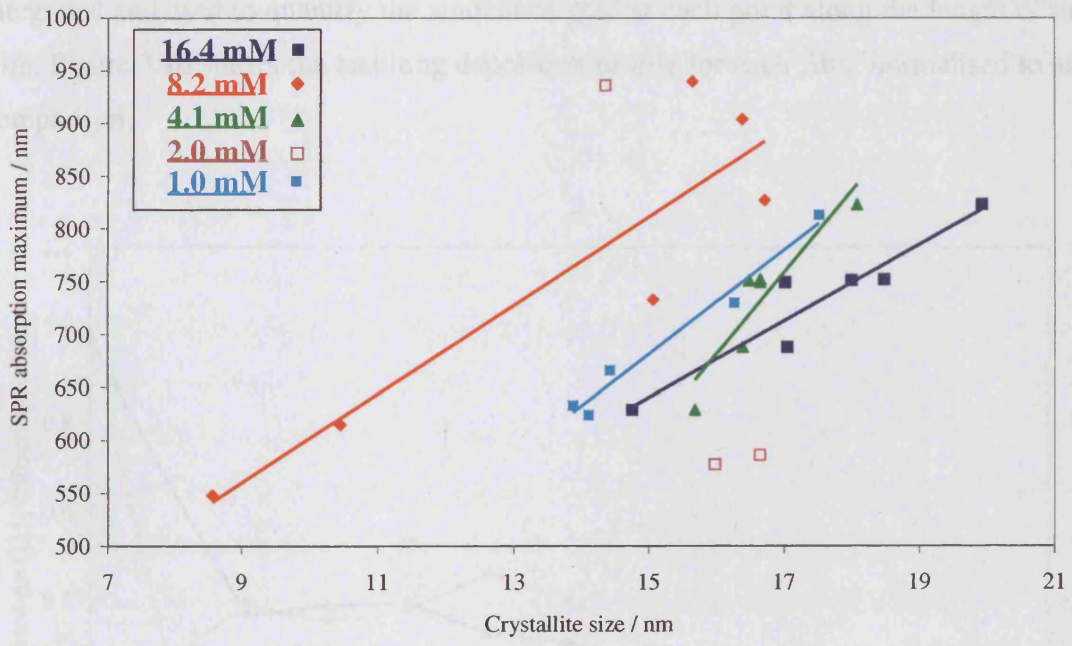

Figure 3.15: Relationship between gold crystallite size, derived from XRD data, and SPR absorption maximum for films deposited from various concentrations of [$HAuCl_4$].

The crystallite size derived from the Au [111] diffraction peak FWHM was also compared to the frequency of the SPR. Figure 3.15 shows this relationship for each of the films discussed in this section. When viewed as a whole, the data appears to show

no correlation between crystallite size and SPR. However, within each film, a linear trend can be clearly discerned, shown by coloured trendlines in figure 3.15.

Substrate temperature

In order to investigate the dependence of the deposition rate on temperature, depositions were carried out using reduced substrate temperatures of 400°C and 350°C. A further attempted deposition at a substrate temperature of 250°C resulted in no appreciable film on the substrate. As before, a precursor solution was made up using [$HAuCl_4$] (0.080 g, 0.2 mmol) in methanol (50 mL), and a gas flow rate of 2.0 L min^{-1} was used. The films appeared blue, and were poorly adherent to the substrate. A greater proportion of the substrate was coated, compared with the depositions at 500°C.

Powder XRD patterns were recorded along the length of each film. In each case peaks corresponding to crystalline cubic gold were observed. The Au [111] peak was integrated and used to quantify the amount of gold at each point along the length of the film. Figure 3.16 shows the resulting deposition profile for each film, normalised to aid comparison.

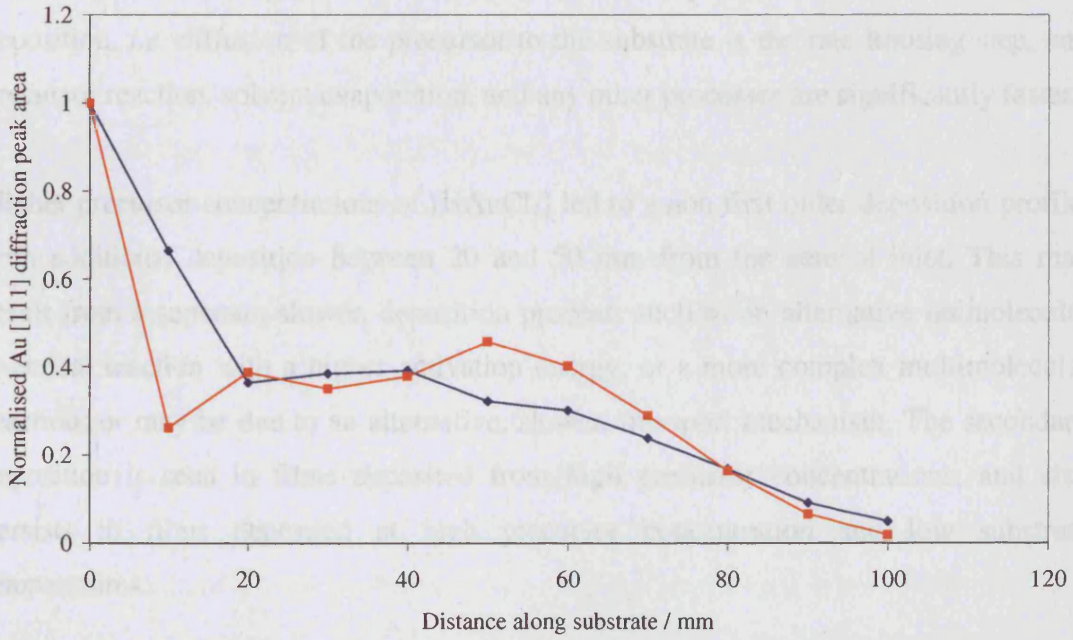

Figure 3.16. Deposition profile of gold films deposited from [$HAuCl_4$] at 400°C (blue points) and 350°C (red points).

In each case, deposition was greatest at the front of the substrate, and in each case the deposition reached zero at approximately 100 mm from the aerosol inlet. The profiles do not appear to be first order decreases, as seen in films deposited from low concentrations of [$HAuCl_4$], but rather they incorporate the distinctive secondary deposition feature previously seen in films deposited from a high concentration of [$HAuCl_4$].

3.3.2 Discussion

Deposition kinetics

Since CVD is a complex multi-step process, discussion of kinetics is often undertaken in only the most general terms.[29] In the case of the depositions from [$HAuCl_4$] described here, there are a number of simplifying factors that allow more insight into the reaction kinetics than in some other CVD processes. Firstly, the deposition is from a single source precursor, and the decomposition of the precursor is unimolecular. Secondly, there is a single deposited material, and the use of powder XRD at regular intervals allows the easy measurement of the deposition profile. The deposition profile of the film deposited from the lowest concentration of [$HAuCl_4$] corresponded to a first order process, as shown in figure 3.11. This type of profile may result from a diffusion limited deposition, *i.e.* diffusion of the precursor to the substrate is the rate limiting step, and precursor reaction, solvent evaporation, and any other processes are significantly faster.

Higher precursor concentrations of [$HAuCl_4$] led to a non first order deposition profile, with additional deposition between 20 and 50 mm from the aerosol inlet. This may result from a separate, slower, deposition process, such as an alternative unimolecular chemical reaction with a higher activation energy, or a more complex multimolecular reaction, or may be due to an alternative, slower, transport mechanism. The secondary deposition is seen in films deposited from high precursor concentrations, and also persists in films deposited at high precursor concentration and low substrate temperatures.

The formation and deposition of gas phase particles is a possible deposition mechanism in CVD. This deposition mechanism is expected to be slower than deposition from diffusion of molecular precursors to the substrate, due in part to thermophoresis acting

on the particles. Particle deposition could, therefore be the secondary deposition mechanism shown in figure 3.12. Gas phase particle formation would be more prevalent at higher precursor concentrations, which correlates with the observance of the secondary deposition mechanism at high precursor concentrations.

Film nanostructure

The hypothesis of gas phase particle formation correlates to some extent with the observed film morphologies. SEM imaging showed that films deposited from [$HAuCl_4$] consisted of particles, rods and regions of island-like growth. Such variation in film morphology has not been observed in gold films deposited by physical methods,[68-70, 73, 165] and previous reports of deposition of gold by CVD do not mention the nanostructure, being more concerned with patterned deposition and film purity. The presence of particles and rods suggests that gas phase reactions occur, as particles are known to form in the gas phase during thermal CVD.[24, 25, 28, 143] The presence of island-like growth is usually typical of surface reaction.[26] Therefore, it is likely that both surface and gas phase reaction occurs, and both have an effect on the film morphology. Thus depositions using [$HAuCl_4$] are similar in this regard to previously reported particle assisted CVD of materials such as TiO_2.[24] The presence of a large number of long rod like particles in many of the films is an interesting observation, considering that previous studies of gas phase gold particle formation have produced roughly spherical particles,[22, 166] and surfactants are required to grow gold nanorods in solution.[65, 167] It is not clear how these particles form within the CVD reactor, or why they seem to be more prevalent at lower precursor concentrations.

Optical absorption of gold films

The optical properties of nano-scale gold films are strongly influenced by the micro and nanostructure.[70, 165] Films deposited from [$HAuCl_4$] show SPR absorption maxima ranging from 550 – 950 nm. In some cases, two SPR peaks can be distinguished. Two SPR absorption peaks have been observed in large gold particles, where quadroplar and dipolar peaks are present,[54] and in gold nanorods where longitudinal and transverse peaks are present.[168] In contrast, discontinuous films of gold prepared by a variety of methods tend to show only a single broad SPR peak, with no discernable shoulder, even for relatively red-shifted SPR peaks appearing at wavelengths longer than 700 nm.[71-73]

SEM imaging, shown in figure 3.9, clearly shows the presence of rod-like structures on the surface of the films, suggesting that the presence of two SPR peaks could be due to separate longitudinal and transverse plasmons. In concurrence with this speculation, the film deposited from the highest concentration of [$HAuCl_4$] showed very few rod like structures in the SEM images, and the absorption spectrum showed only one, very broad SPR peak (figure 3.13). Meanwhile, the film deposited from 8.2 mM [$HAuCl_4$] contained a considerable amount of nanorods, and showed two well separated SPR peaks.

It was found that the wavelength of the SPR absorption correlated with both the amount of gold present in the film and the gold crystallite size. In the case of SPR wavelength vs. amount of gold present, an approximate linear fit could be applied to the collective data from all the films studied (figure 3.17). The coefficient of determination (R^2 value) of this linear fit was determined to be 0.67. In the case of SPR wavelength vs. crystallite size, an attempt to linearly fit the entire data set was much less successful; the R^2 value for the best linear fit was 0.22.

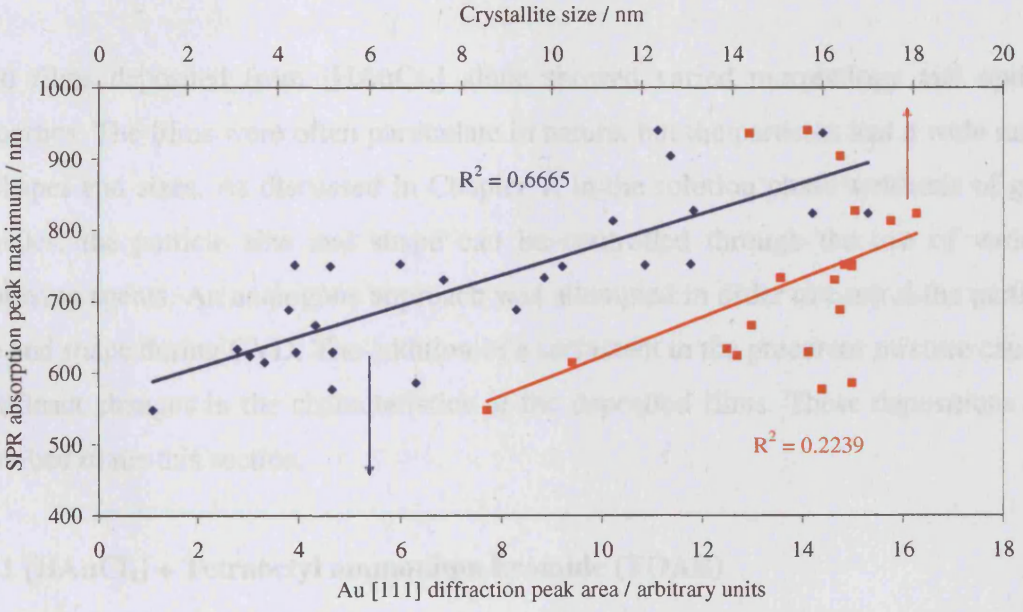

Figure 3.17. Relationships between crystallite size, Au [111] diffraction peak area and SPR absorption maximum for all films deposited from single source [$HAuCl_4$]. Linear fits and their coefficients of determination are shown for both data sets.

However, when data from each film is considered separately, as shown in Figure 3.15, good linear correlations can be seen, with R^2 values between 0.8 and 0.9, although only 5 – 7 data points are available in each case. Although correlation does not imply

causation, it can be said generally that in films deposited from [$HAuCl_4$], the Au [111] diffraction peak area is a reasonably good predictor of SPR wavelength. It may be a useful tool considering the ease of measuring the powder diffraction pattern compared with, for example, recording and analysing an SEM image. As stated previously, the relationship between SPR wavelength and amount of gold present across a range of films is surprising considering the very different morphologies present in those films. Perhaps because it is a measure of the total amount of gold and will incorporate measures of film thickness and coverage, the diffraction peak area is a useful predictor of SPR absorption maximum for a wide range of films. Within a specific film, the crystallite size is also a good predictor of SPR, but when data from all films is considered, the linear fit becomes poor. It is not known what causes the relationship between crystallite size and SPR wavelength to vary between films, although this may be a convenient way of quantifying surface plasmon interactions between gold crystallites.

3.4 Depositions using [$HAuCl_4$] + Surfactant

Gold films deposited from [$HAuCl_4$] alone showed varied morphology and optical properties. The films were often particulate in nature, but the particles had a wide range of shapes and sizes. As discussed in Chapter 1, in the solution phase synthesis of gold particles, the particle size and shape can be controlled through the use of various stabilising agents. An analogous approach was attempted in order to control the particle size and shape during CVD. The addition of a surfactant to the precursor mixture caused significant changes in the characteristics of the deposited films. These depositions are described in the this section.

3.4.1 [$HAuCl_4$] + Tetraoctyl ammonium bromide (TOAB)

Depositions were carried out using [$HAuCl_4$] and TOAB, a quaternary ammonium salt that has been previously used as a phase transfer reagent and surfactant for directing nanoparticle growth.[82] The intention of the investigation was to discover whether TOAB could be used as a shape directing agent in a CVD environment. Precursor solutions were made by dissolving [$HAuCl_4$] in methanol followed by addition of TOAB. The solution was stirred for 10 min, during which time the colour changed from

pale yellow to dark orange, associated with the substitution of chloride for bromide ions in the gold coordination sphere:[101]

$$[HAuCl_4] + 4Br^- \rightarrow [HAuBr_4] + 4Cl^-$$

Initial investigations were carried out using a precursor solution made up of [$HAuCl_4.3H_2O$] (0.080 g, 0.2 mmol) and TOAB (0.5 g, 0.9 mmol) in methanol (50 mL) using a substrate temperature of 500°C and a flow rate of 2.0 L min^{-1}. The addition of TOAB to the precursor mix strongly affected the appearance of the deposited films compared with deposition using [$HAuCl_4$] alone. The entire substrate was not covered; the films were localised to a narrow strip near the aerosol inlet. Different portions of the film appeared either red or blue in transmission. In reflection, the films appeared metallic gold or green.

Secondary electron SEM revealed that the film was made up of spherical particles which appeared to be distributed randomly on the substrate. Figure 3.18 shows SEM images taken along the length of the film. Using SEM conducted in backscattering the spherical particles appeared brighter than the background. This shows that the particles were more dense than the surface beneath them, suggesting gold particles on a silica surface. The images in figure 3.18 show the coverage to be less than one monolayer of particles at the front of the substrate, as uncoated silica can be seen between the particles. The coverage of the substrate initially increased with increasing distance from the aerosol inlet. At around 15 mm along the film, the coverage exceeded one monolayer, and particles could be seen stacked on top of each other. Throughout the film, including in areas of greater than one monolayer coverage, particles appeared non agglomerated and spherical.

Particle diameters (d) were measured manually using the secondary electron SEM images. Backscattered electron images were not used for particle size determination due to poor resolution of the particle edges. Images taken in secondary electron mode, being more sensitive to surface morphology, were better suited to particle measurement. Histograms showing the particle size distributions are shown in figure 3.18 next to the relevant SEM image. Throughout the substrate, a significant proportion of the population was clustered in a near symmetrical distribution centred on d = 120 nm. At the front of the substrate, smaller particles, approximately 30 nm in diameter were also

present in significant numbers. This population of smaller particles decreased in number with increasing distance from the aerosol inlet.

Figure 3.18, panel C shows that at 9.6 mm along the substrate the distribution of particle sizes appeared unimodal and centred around d = 120 nm. Nanoparticle formation reactions typically produce normal[87] (Gaussian) or log-normal size distributions.[59, 88, 89] A probability plot was used in order to determine which distribution best fits the particles produced in this deposition. Figure 3.19 shows the probability plot of the cumulative frequency against the diameter, d, and log diameter, log(d) using the same data as is displayed in figure 3.18 panel C. The probability plot against d is seen to be close to linear; the probability plot against log d shows greater deviation from linearity, showing that a normal distribution is more appropriate.[87] Size distributions taken from images in panel C (figure 3.18) were therefore fitted with a normal distribution with mean particle diameter, μ = 121 nm and standard deviation, σ = 18 nm. The values of μ and σ showed little variation over the length of the substrate. The percentage standard deviation of 15 % compares favourably with those observed in optimised solution phase gold nanoparticle syntheses.[92, 95] The histograms obtained from images A and B (figure 3.18) were fitted with bimodal normal distributions to take into account the presence of smaller particles.

In order to confirm that the particles seen in secondary electron SEM images were gold particles on a silica substrate, backscattered SEM images were taken. The bright areas in the backscattered image shown in figure 3.20 represent areas of high electron density. Since metallic gold has significantly higher electron density than silica, it is expected that gold particles will appear as bright spots on a dark background. It can be seen that the bright spots in the backscattered electron image in figure 3.20 correspond to the positions of the spherical particles seen in the corresponding secondary electron image, taken at the same point. Some of the smaller particles seen in the secondary electron image are not seen in the backscattered electron image. This may be due to the lower intensity of the backscattered electrons. It should also be noted that the apparent size of the particles is smaller in the backscattered electron image. Since image contrast in secondary electron images is dependent on the topography of the sample, and steep or highly curved surfaces appear as bright areas, it is thought that secondary electron images will more accurately resolve the edges of the nanoparticles. Therefore, all measurements of nanoparticle size have been taken from secondary electron images.

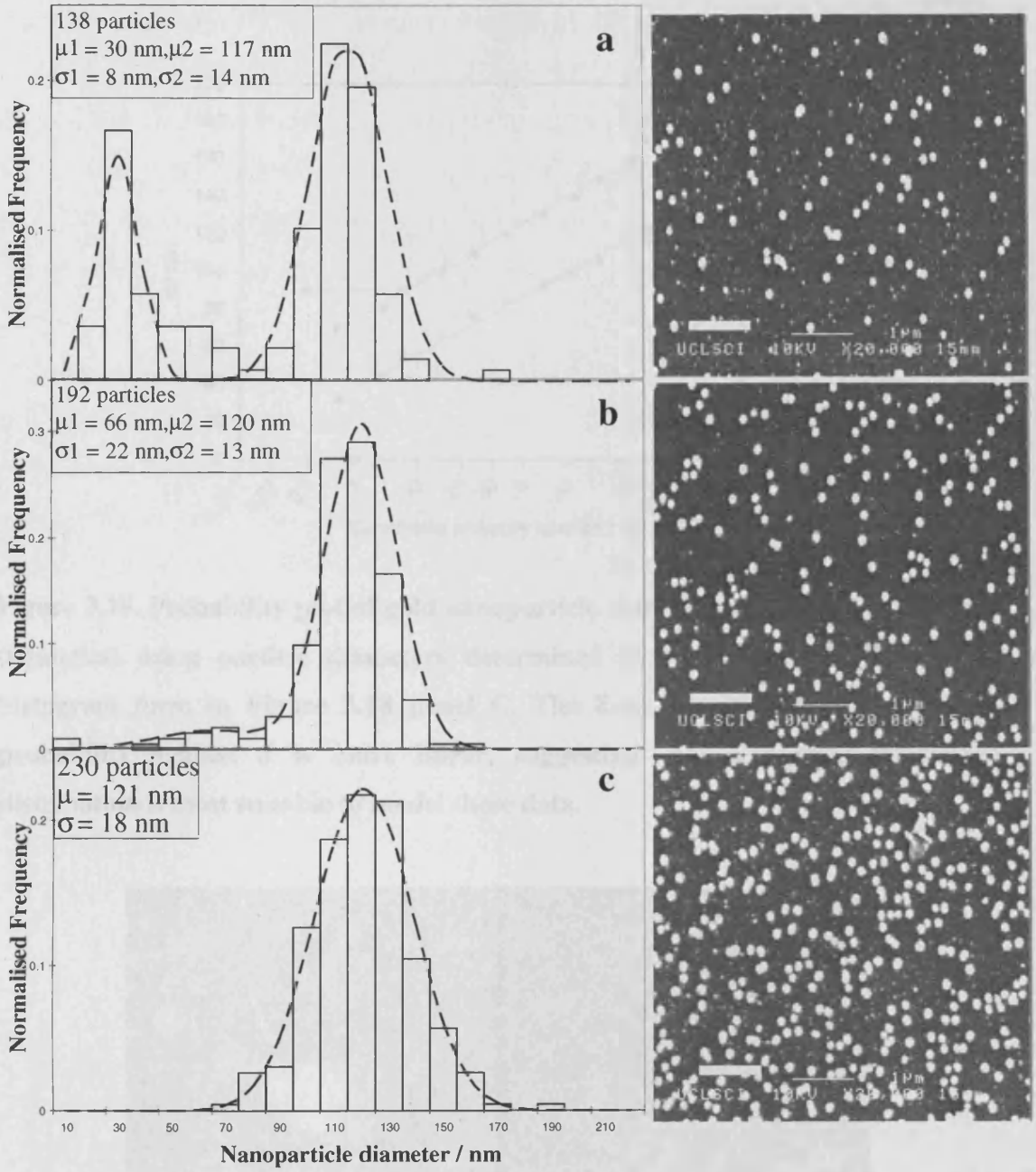

Figure 3.18. SEM (secondary electron) images and associated particle size distributions of a gold nanoparticle film deposited from [$HAuCl_4$] and TOAB. Scale bars measure 1 μm. The analyses relate to various distances along the substrate: a) 4.3 mm, b) 6.3 mm, c) 9.6 mm. The particle size distributions are fitted to unimodal or bimodal Gaussian distributions (dashed lines) as discussed in the text. The sample size and the mean (μ) and standard deviation (σ) for each Gaussian fit are indicated.

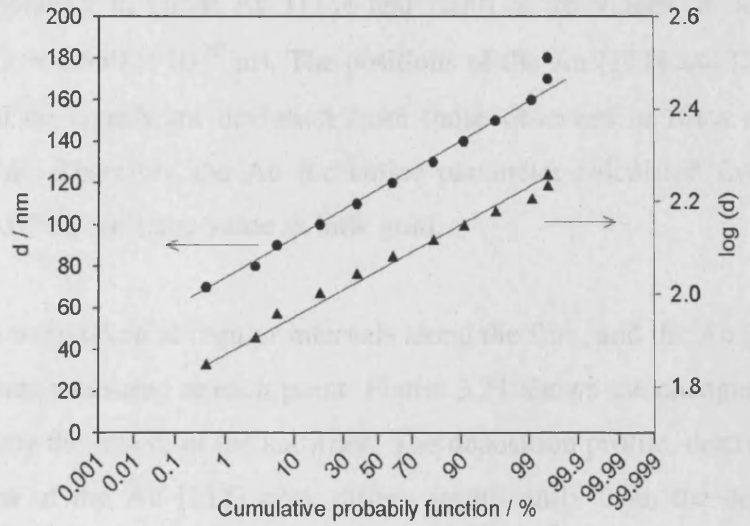

Figure 3.19. Probability plot of gold nanoparticle diameter, d (circles), and log (d) (triangles) using particle diameters determined by SEM, and also plotted in histogram form in Figure 3.18 panel C. The lines are arbitrary. The plot of probability against d is more linear, suggesting that a normal (Gaussian) distribution is most suitable to model these data.

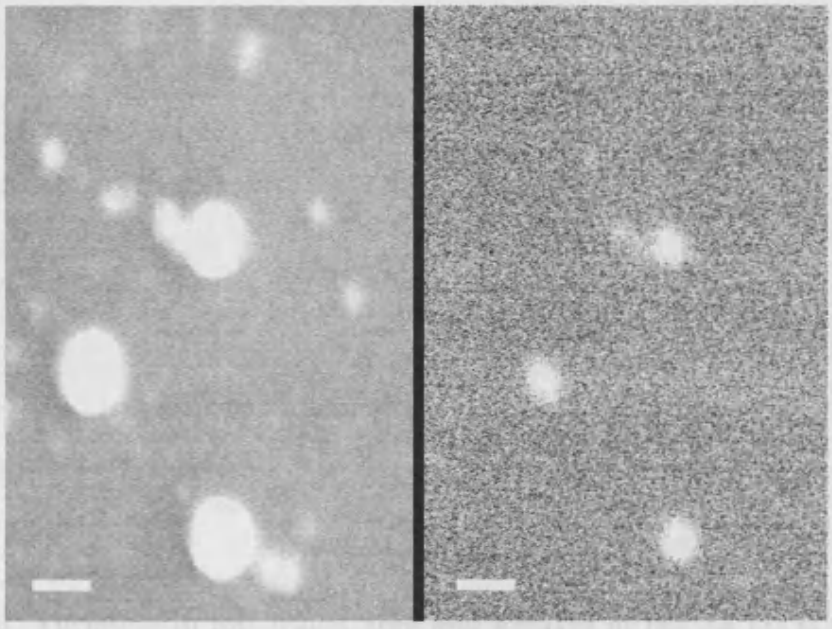

Figure 3.20. ***Left:*** **High resolution secondary electron SEM image of gold nanoparticles deposited from [$HAuCl_4$] and TOAB.** ***Right:*** **High resolution backscattered electron SEM image of the same region. Both scale bars measure 100 nm.**

Glancing angle powder XRD revealed the presence of crystalline gold with diffraction peaks corresponding to cubic Au [111] and [200] at 2θ values of 38.4° and 44.3° respectively ($\lambda = 1.540 \times 10^{-10}$ m). The positions of the Au [111] and [200] diffraction peaks showed no significant deviation from those observed in films deposited from [$HAuCl_4$] alone. Therefore the Au fcc lattice parameter calculated from these peaks remains $a = 4.07$ Å, the same value as bulk gold.

XRD patterns were taken at regular intervals along the film, and the Au [111] peak area and FWHM was measured at each point. Figure 3.21 shows the changing XRD profile of the film along the length of the substrate. The deposition profile, determined from the integrated area of the Au [111] peak differs significantly from the depositions from [$HAuCl_4$] alone, discussed in the previous section. The integrated area was very low at the front of the substrate, and reached a maximum at 20 mm along the film. In contrast, in films deposited from [$HAuCl_4$] alone, the peak area decreased monotonically from a high value at the front of the substrate.

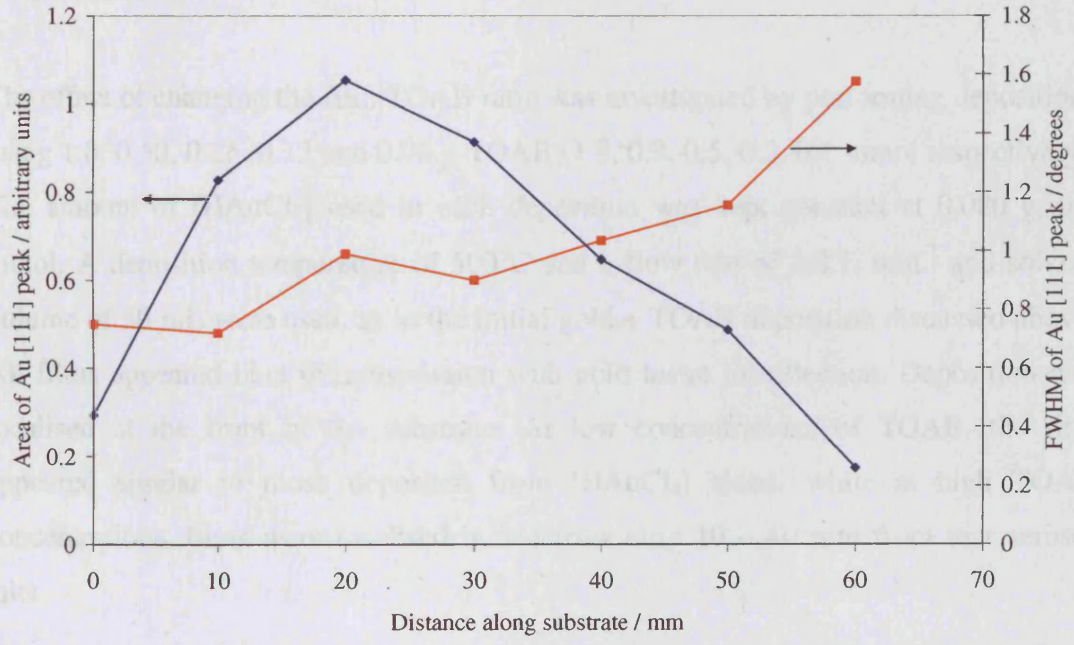

Figure 3.21. Variation in integrated area and FWHM of the Au [111] diffraction peak along the length of a gold film deposited from [$HAuCl_4$] and TOAB.

The FWHM of the diffraction peak generally increases with increasing distance, showing a reduction in the crystallite size, if strain effects are ignored. The crystallite size was calculated from the Au [111] FWHM using the Scherrer equation. Crystallite

sizes ranged from 8 – 17 nm, which is slightly smaller than in the film deposited in the absence of TOAB. Some particles of this size were observed by SEM, especially near the front of the substrate. These particles could be single crystals. However, the majority of particles are much larger than the Scherrer crystallite size, meaning that each particle must be polycrystalline. The decrease in crystallite size along the length of the substrate may be due to depletion of the precursor.

X-ray photoelectron spectroscopy confirmed the presence of metallic gold on the substrate surface. Au $4f_{5/2}$ and $4f_{7/2}$ photoelectron peaks were each fitted with a unimodal Gaussian-Lorentzian fit, with peak centres at binding energies of 87.5 eV and 84.0 eV respectively, corresponding to metallic gold.[163] Chlorine and bromine were not detected. Nitrogen was detected, with a N 1s photoelectron peak at 400.0 eV, which is typical of nitrogen in amines,[169] suggesting the presence of quaternary ammonium capping groups on the film surface. However, this binding energy value is also close to that expected for N_2, so may possibly be due to adsorbed atmospheric gas.

Gold : TOAB Ratio

The effect of changing the Au : TOAB ratio was investigated by performing depositions using 1.0, 0.50, 0.25, 0.12 and 0.06 g TOAB (1.8, 0.9, 0.5, 0.2, 0.1 mmol respectively). The amount of [$HAuCl_4$] used in each deposition was kept constant at 0.080 g, 0.2 mmol. A deposition temperature of 500°C and a flow rate of 2.0 L min^{-1} and solvent volume of 50 mL were used, as in the initial gold + TOAB deposition discussed above. All films appeared blue in transmission with gold lustre in reflection. Deposition was localised at the front of the substrate. At low concentrations of TOAB, the film appeared similar to those deposited from [$HAuCl_4$] alone, while at high TOAB concentrations, films were localised in a narrow strip 10 – 40 mm from that aerosol inlet.

SEM imaging conducted in secondary electron mode revealed highly variable film morphology. Figure 3.22 shows images taken along the length of films deposited using different concentrations of TOAB.

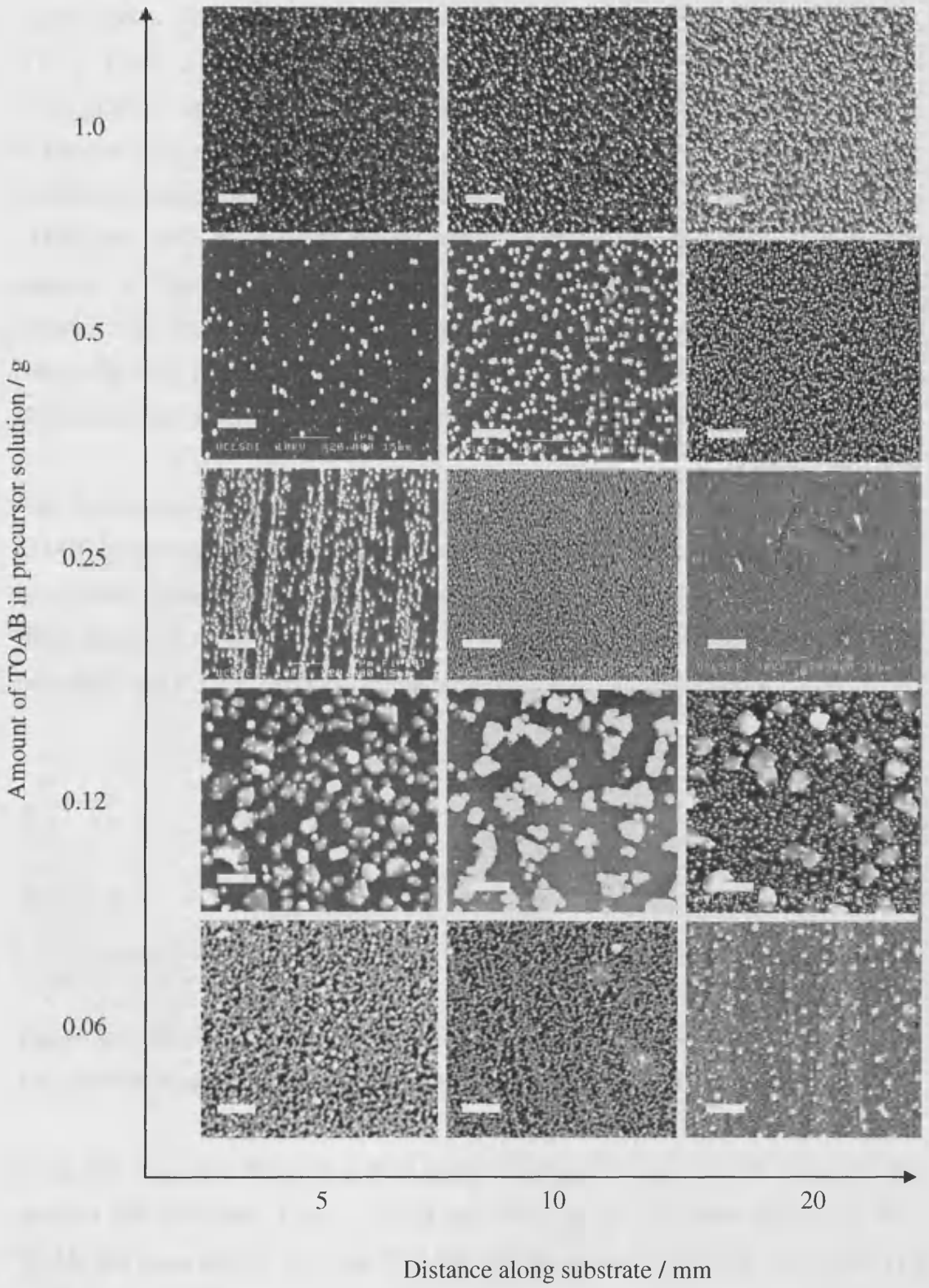

Figure 3.22. Secondary electron SEM images taken along the length of films deposited from mixtures of TOAB (0.5 – 0.06 g) and [$HAuCl_4$] (0.080 g). Scale bars measure 1 μm.

At higher concentrations of TOAB (1.0 – 0.25 g), spherical particles are clearly visible throughout the films. Even in portions of the film where particle coverage is high, agglomeration of particles does not seem to have occurred. In the film deposited using 0.12 g TOAB, some spherical particles are observed, accompanied by cuboids or flat plates. SEM imaging conducted in backscattering mode, which shows the composition of the film, both the spherical particles and the cuboids appear to have similar electron density, suggesting that both are composed of gold. In the film deposited from 0.06 g TOAB, the structure appears grainy, which could be due to highly agglomerated particles or island growth formation. Further along the substrate, some spherical particles over 100 nm in diameter are seen. In all cases, even in that of the lowest concentration of TOAB, it is clear that the presence of the surfactant has a strong effect on the nanostructure of the film.

Size distributions could be determined from films deposited using 1.0, 0.5 and 0.25 g of TOAB. In films deposited from lower amounts of TOAB, individual particles could not be accurately measured due to agglomeration. Figure 3.23 shows size distributions from films deposited from 1.0 and 0.25 g TOAB. The size distribution from the film deposited from 0.5 g TOAB has already been presented, in figure 3.18.

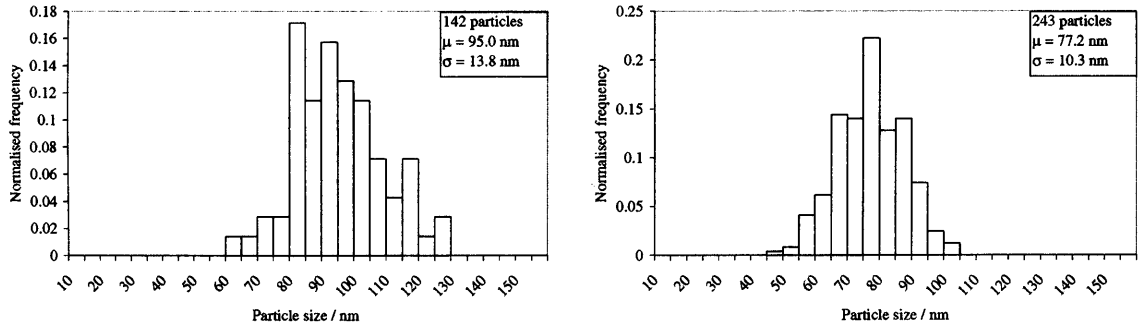

Figure 3.23. Size distributions of particles deposited using [$HAuCl_4$] + TOAB. *Left:* 1.0 g TOAB. *Right:* 0.25 g TOAB. The x-axis scale is identical in each histogram.

In the film deposited from 1.0 g TOAB, the mean particle size was 95.0 nm, and the standard deviation was 14 nm (15 % of the mean). In the film deposited from 0.25 g TOAB, the mean particle size was 77.2 nm, and the standard deviation was 10 nm (13 % of the mean). Therefore both of these depositions resulted in smaller particles compared to the previously described deposition carried out using 0.5 g TOAB.

Powder XRD patterns showed peaks corresponding to crystalline gold for all samples. There was no significant variation in the peak positions of the Au [111] and [200] peaks, either with changing TOAB concentration or compared to films deposited from [$HAuCl_4$] alone. As previously described, XRD measurements were taken at regular intervals along the length of each film. The Au [111] peak position, area and FWHM were measured at each point. The peak areas were normalised to the maximum value for each sample, to facilitate comparison between films. Figure 3.24 shows the result of this analysis.

In contrast to films deposited from [$HAuCl_4$] alone, the point of maximum deposition did not occur close to the aerosol inlet, but varied in position with the amount of TOAB present. With a high concentration of TOAB, the maximum deposition occurred at 40 mm from the aerosol inlet and decreased with the amount of TOAB in the precursor solution (figure 3.24). It was also evident from the XRD data that the total amount of gold deposited in each film varied with TOAB concentration. The total amount of gold deposited in each film was estimated by summing the peak areas of the Au [111] diffraction peaks, taken at 10 mm intervals along the entire length of each film. Figure 3.25 shows this estimation of total gold deposition plotted against amount of TOAB used.

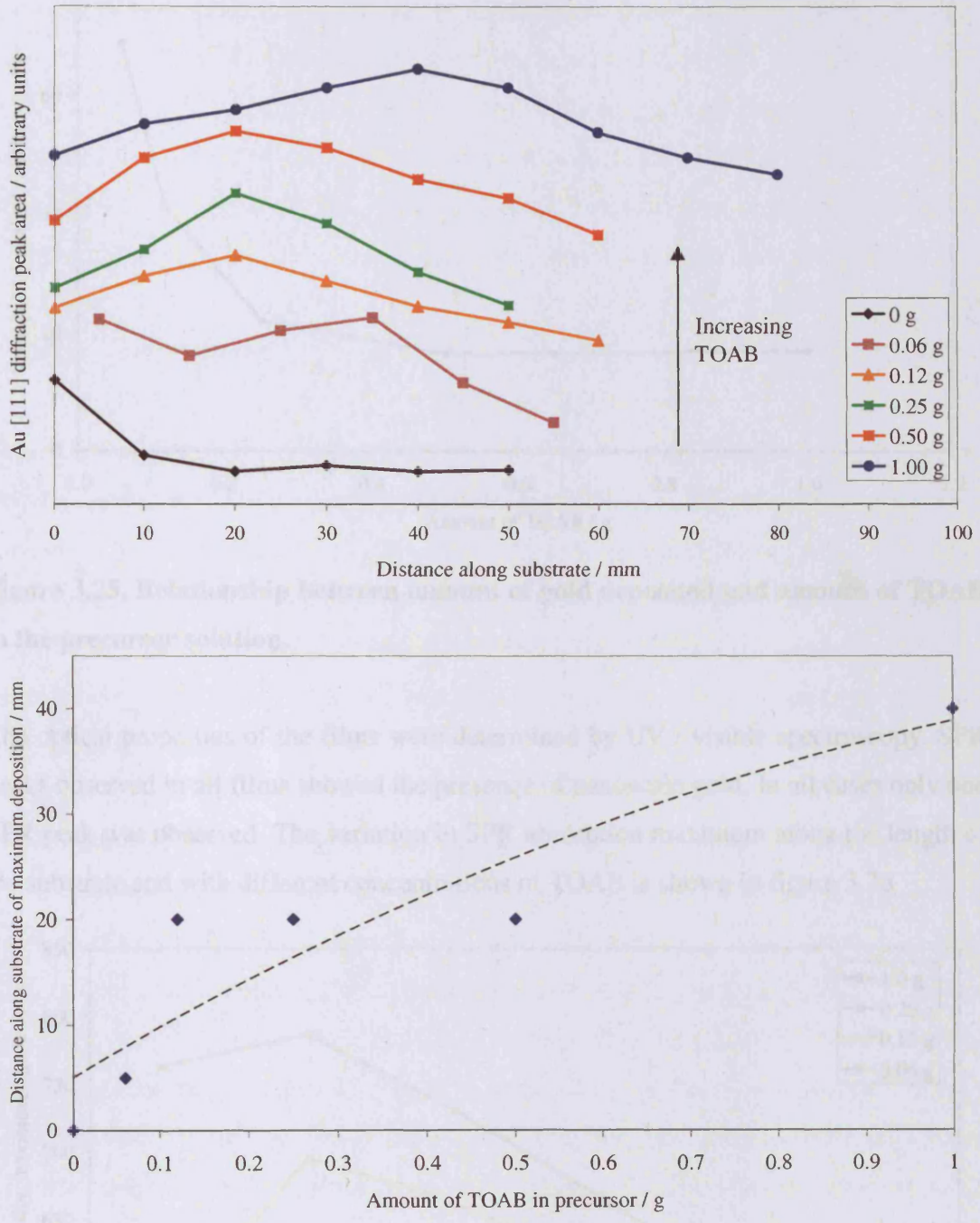

Figure 3.24. ***Top:*** **Integrated area of the Au [111] diffraction peak along the length of films deposited from [$HAuCl_4$] (0.080 g) and various amounts of TOAB, as indicated in the legend. Each data series is normalised, and offset for clarity.** ***Bottom:*** **Distance of greatest deposition along the substrate, for the films deposited using various amounts of TOAB.**

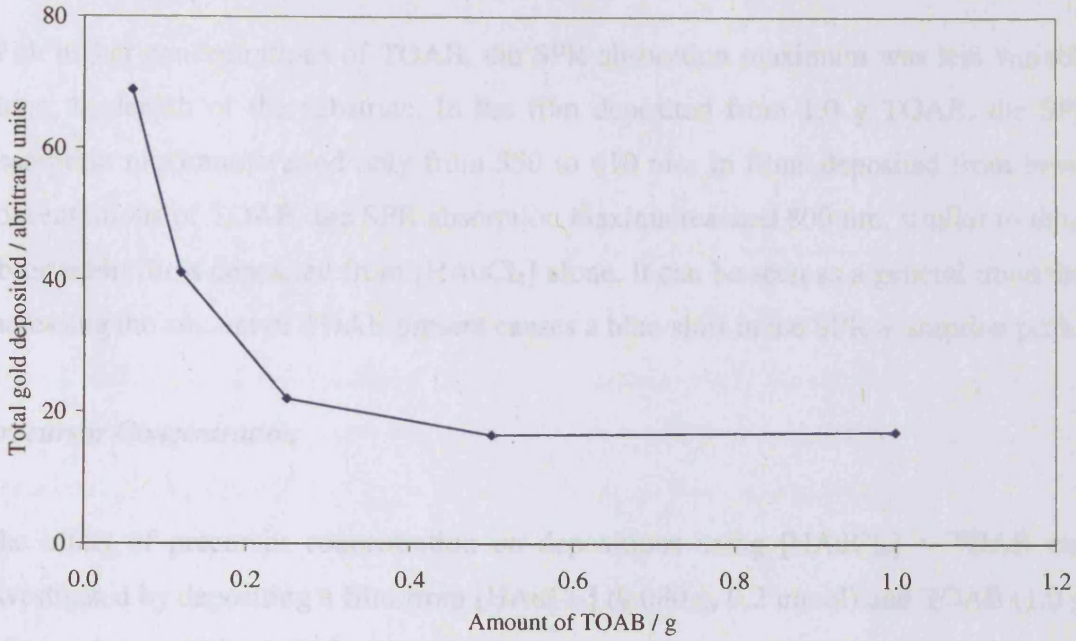

Figure 3.25. Relationship between amount of gold deposited and amount of TOAB in the precursor solution.

The optical properties of the films were determined by UV / visible spectroscopy. SPR peaks observed in all films showed the presence of nanoscale gold. In all cases only one SPR peak was observed. The variation in SPR absorption maximum along the length of the substrate and with different concentrations of TOAB is shown in figure 3.26.

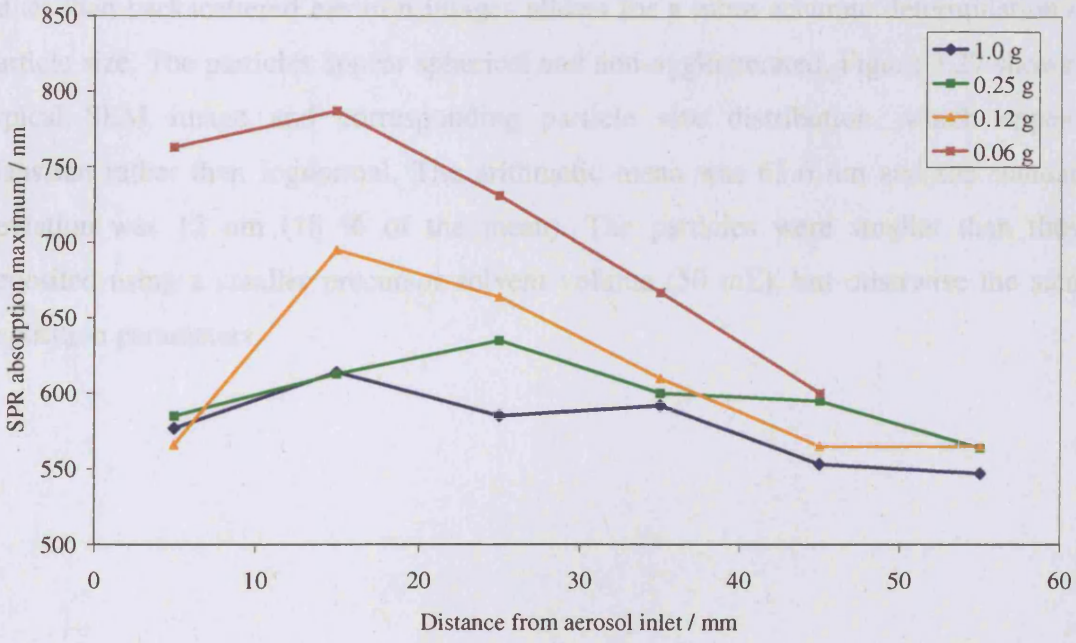

Figure 3.26. Variation in SPR absorption maximum along the length of films deposited from [$HAuCl_4$] and various amounts of TOAB (indicated, inset).

With higher concentrations of TOAB, the SPR absorption maximum was less variable along the length of the substrate. In the film deposited from 1.0 g TOAB, the SPR absorption maximum varied only from 550 to 610 nm. In films deposited from lower concentrations of TOAB, the SPR absorption maxima reached 800 nm, similar to those observed in films deposited from [$HAuCl_4$] alone. It can be seen as a general trend that increasing the amount of TOAB present causes a blue-shift in the SPR absorption peak.

Precursor Concentration

The effect of precursor concentration on depositions using [$HAuCl_4$] + TOAB was investigated by depositing a film from [$HAuCl_4$] (0.080 g, 0.2 mmol) and TOAB (1.0 g, 1.8 mmol) in methanol (200 mL) at a substrate temperature of 500°C using a flow rate of 2.0 L min^{-1}. These parameters are the same as those used for a deposition already reported, except that a larger volume of solvent was used. The film appeared similar to those already described, a localised blue strip of deposition approximately 10 – 60 mm from the aerosol inlet.

SEM conducted in secondary electron mode revealed the presence of particles on the substrate surface. As discussed earlier, it is believed that the use of secondary electron rather than backscattered electron images allows for a more accurate determination of particle size. The particles appear spherical and non-agglomerated. Figure 3.27 shows a typical SEM image and corresponding particle size distribution, which appears Gaussian rather than lognormal. The arithmetic mean was 65.6 nm and the standard deviation was 12 nm (18 % of the mean). The particles were smaller than those deposited using a smaller precursor solvent volume (50 mL), but otherwise the same deposition parameters.

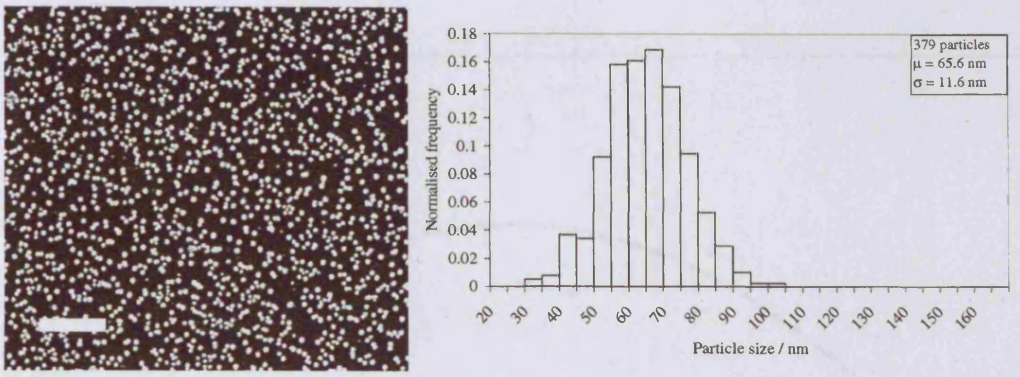

Figure 3.27. SEM (secondary electron) images and associated particle size distributions of a gold nanoparticle film deposited from a low concentration precursor solution of [$HAuCl_4$] + TOAB. The scale bar measures 1 μm.

Glancing angle powder XRD revealed the expected Au [111] and [200] diffraction peaks. As previously described, XRD measurements were taken at regular intervals along the length of the film. The Au [111] peak position, area and FWHM were measured at each point, and this data is shown in figure 3.28.

UV / visible spectroscopy revealed a SPR absorption peak, which varied in position from 690 – 550 nm (figure 3.29).

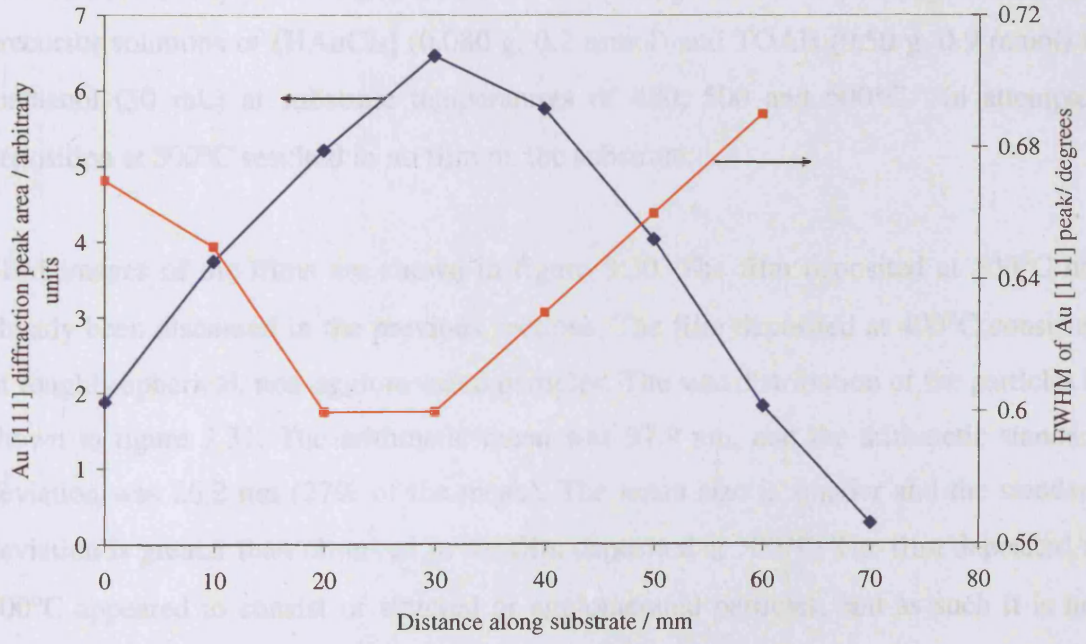

Figure 3.28. Variation in Au [111] diffraction peak area and FWHM with distance along the substrate for a film deposited from a low concentration of [$HAuCl_4$] + TOAB.

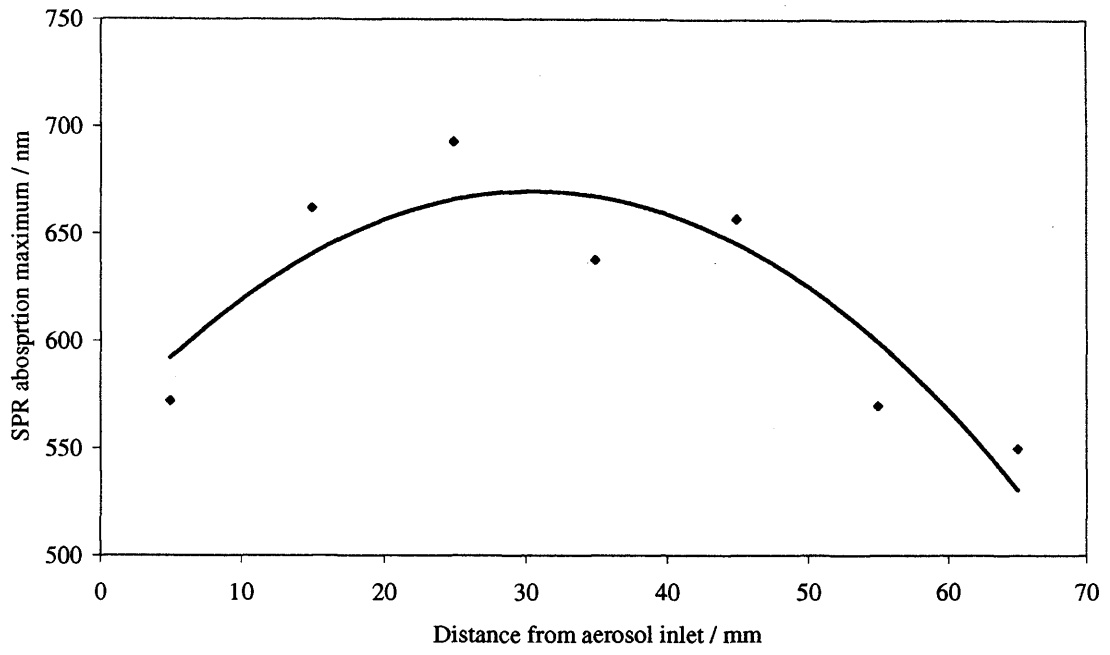

Figure 3.29. Variation in SPR absorption maximum with distance along the substrate for a film deposited from a low concentration of [$HAuCl_4$] + TOAB. The line is a guide to the eye.

Deposition Temperature

The effect of deposition temperature was investigated by depositing films from precursor solutions of [$HAuCl_4$] (0.080 g, 0.2 mmol) and TOAB (0.50 g, 0.9 mmol) in methanol (50 mL) at substrate temperatures of 400, 500 and 600°C. An attempted deposition at 300°C resulted in no film on the substrate.

SEM images of the films are shown in figure 3.30. The film deposited at 500°C has already been discussed in the previous sections. The film deposited at 400°C consisted of roughly spherical, non-agglomerated particles. The size distribution of the particles is shown in figure 3.31. The arithmetic mean was 97.9 nm, and the arithmetic standard deviation was 26.2 nm (27% of the mean). The mean size is smaller and the standard deviation is greater than observed in the film deposited at 500°C. The film deposited at 600°C appeared to consist of sintered or agglomerated particles, and as such it is not possible to obtain an accurate size distribution.

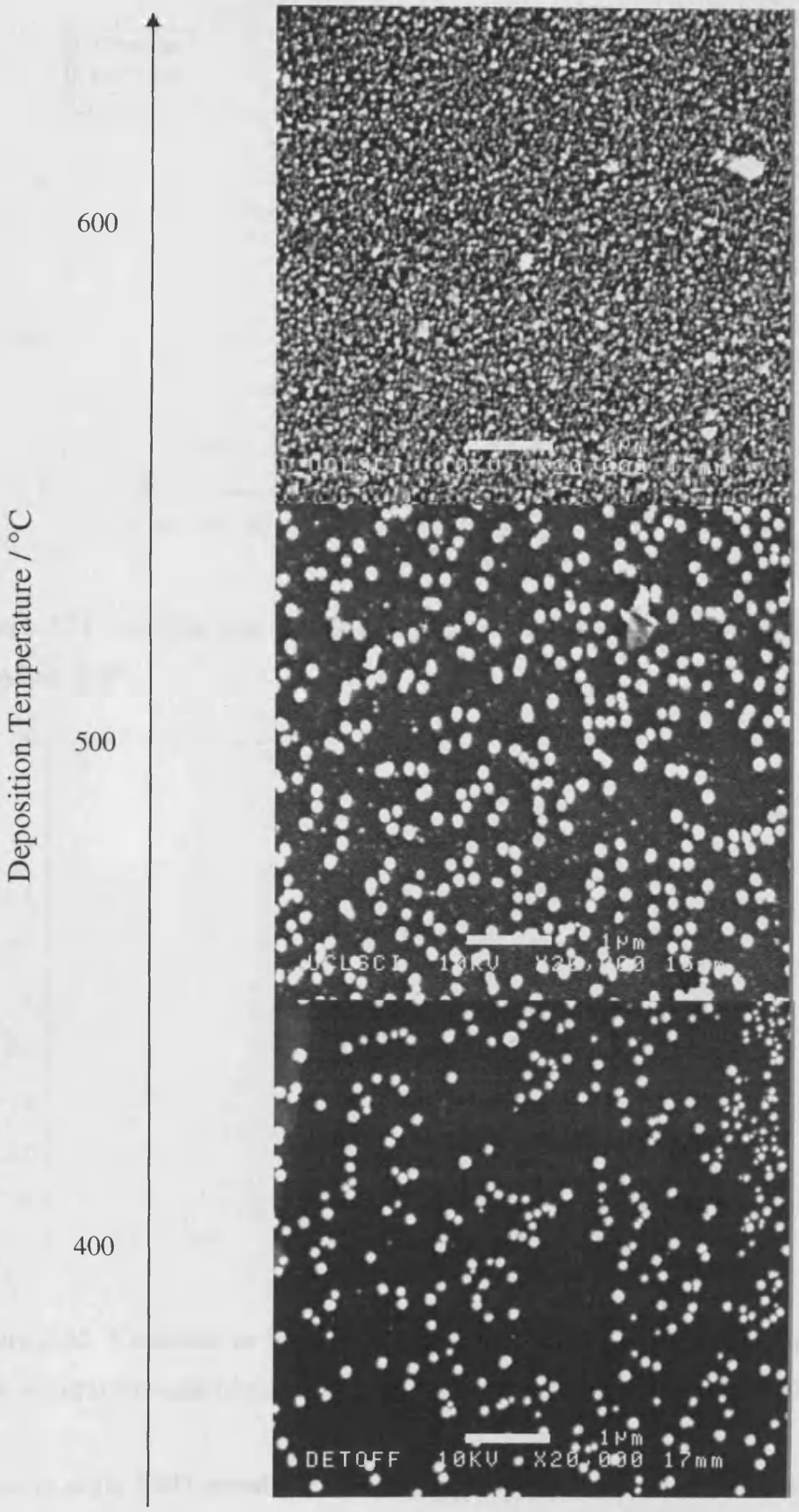

Figure 3.30: SEM images (secondary electron) of films deposited from [HAuCl4] (0.080 g) and TOAB (0.50 g) at various deposition temperature. All images are at the same scale; scale bars measure 1 μm.

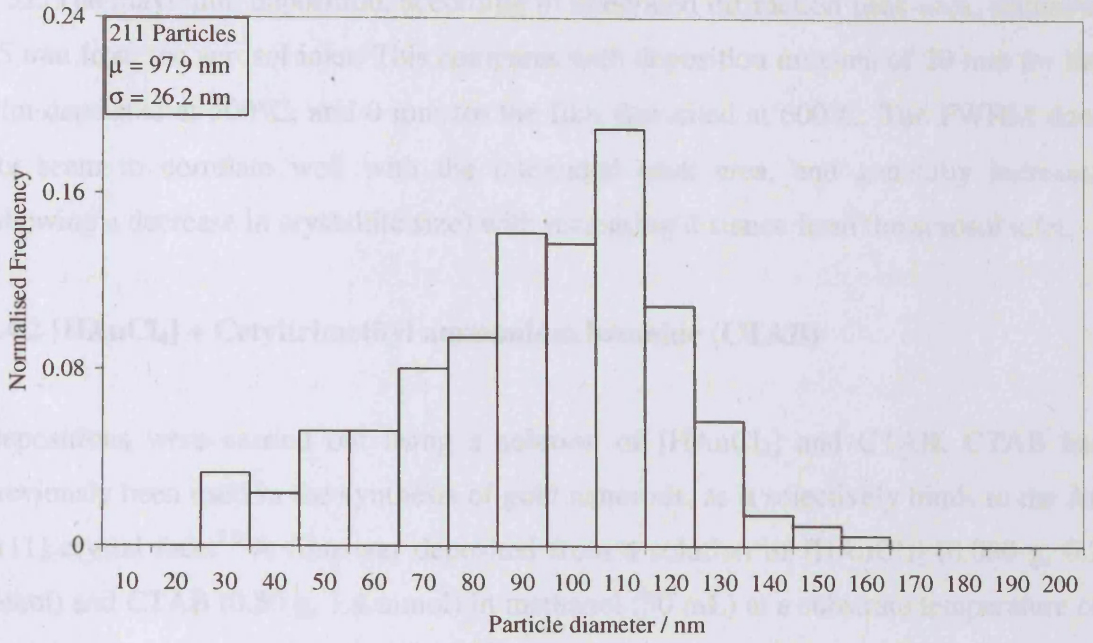

Figure 3.31. Particle size distribution of the film deposited from [$HAuCl_4$] and TOAB at 400°C.

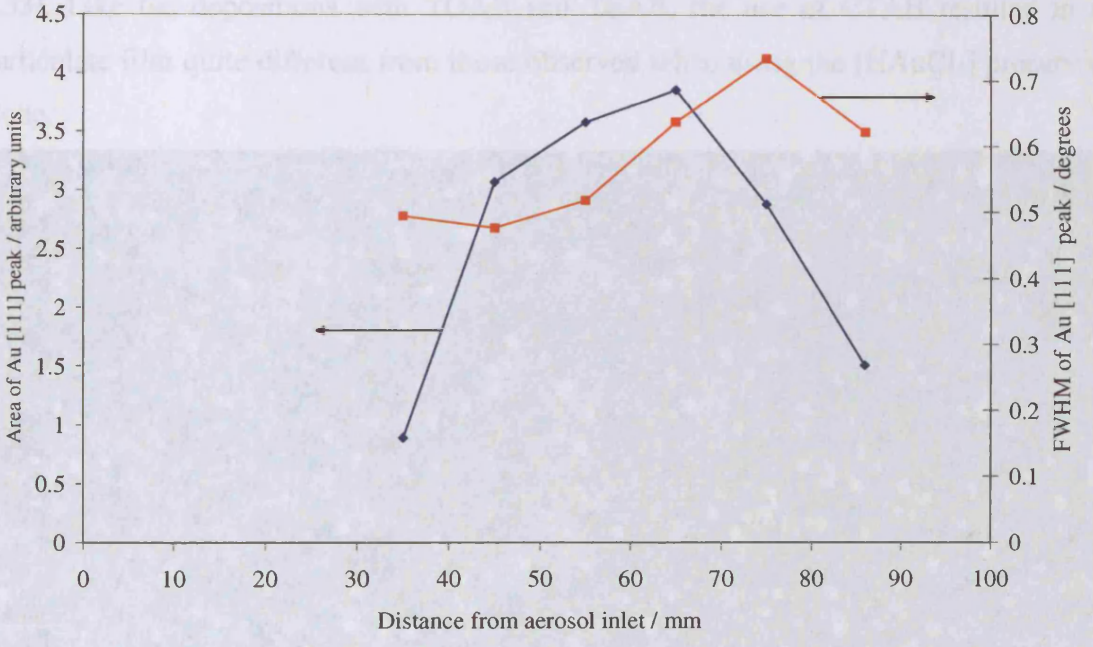

Figure 3.32. Variation in integrated area and FWHM of the Au [111] diffraction peak along the length of a gold film deposited from [$HAuCl_4$] and TOAB at 400°C.

Glancing angle XRD revealed cubic gold peaks in all three films. The positions of the Au [111] and [200] peaks were identical to those recorded for other gold films discussed above, and to reported values for bulk gold. The variation in Au [111] diffraction peak area and FWHM for the film deposited at 400°C is shown in figure

3.32. The maximum deposition, according to integrated diffraction peak area, occurs at 65 mm from the aerosol inlet. This compares with deposition maxima of 20 mm for the film deposited at 500°C, and 0 mm for the film deposited at 600°C. The FWHM does not seem to correlate well with the integrated peak area, and generally increases (showing a decrease in crystallite size) with increasing distance from the aerosol inlet.

3.4.2 $[HAuCl_4]$ + Cetyltrimethyl ammonium bromide (CTAB)

Depositions were carried out using a solution of $[HAuCl_4]$ and CTAB. CTAB has previously been used in the synthesis of gold nanorods, as it selectively binds to the Au [111] crystal face.[77] A film was deposited from a solution of $[HAuCl_4]$ (0.080 g, 0.2 mmol) and CTAB (0.50 g, 1.4 mmol) in methanol (50 mL) at a substrate temperature of 500°C and a gas flow rate of 2.0 L min^{-1}.

SEM images were taken in secondary electron mode along the length of the film (Figure 3.33). Like the depositions with TOAB and TEAB, the use of CTAB resulted in a particulate film quite different from those observed when using the $[HAuCl_4]$ precursor alone.

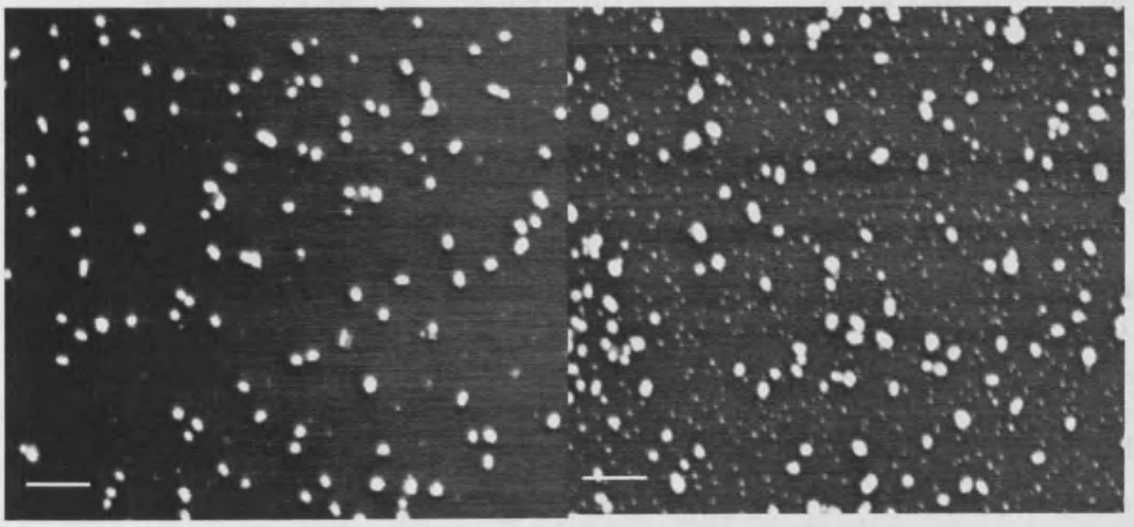

Figure 3.33. Secondary electron SEM images of a film deposited from $[HAuCl_4]$ and CTAB: *left*, 2.2 mm from aerosol inlet, *right*, 4.2 mm from aerosol inlet. Note the presence of elongated rod-like particles. Scale bars measure 1 μm.

Notably some particles are slightly elongated and rod-like. Although some of these have a 'dog-bone' shape, perhaps characteristic of two closely spaced or agglomerated spherical particles, many rods with near constant width along their length can be seen,

suggesting that these rods were not formed by merger of spherical particles. Measurement of the aspect ratios of these particles revealed that they are significantly less spherical and more rod like than particles deposited from TOAB. Figure 3.34 shows the aspect ratio distribution of particles deposited from TOAB and CTAB using otherwise identical CVD conditions. In films deposited from TOAB, over half of the particles measured had an aspect ratio below 1.2, while in films deposited from CTAB, a significant proportion of the measured particles showed aspect ratios from 1.4 to 1.7. It can be concluded that CTAB has a significant shape directing effect on the nanoparticles formed during the deposition process.

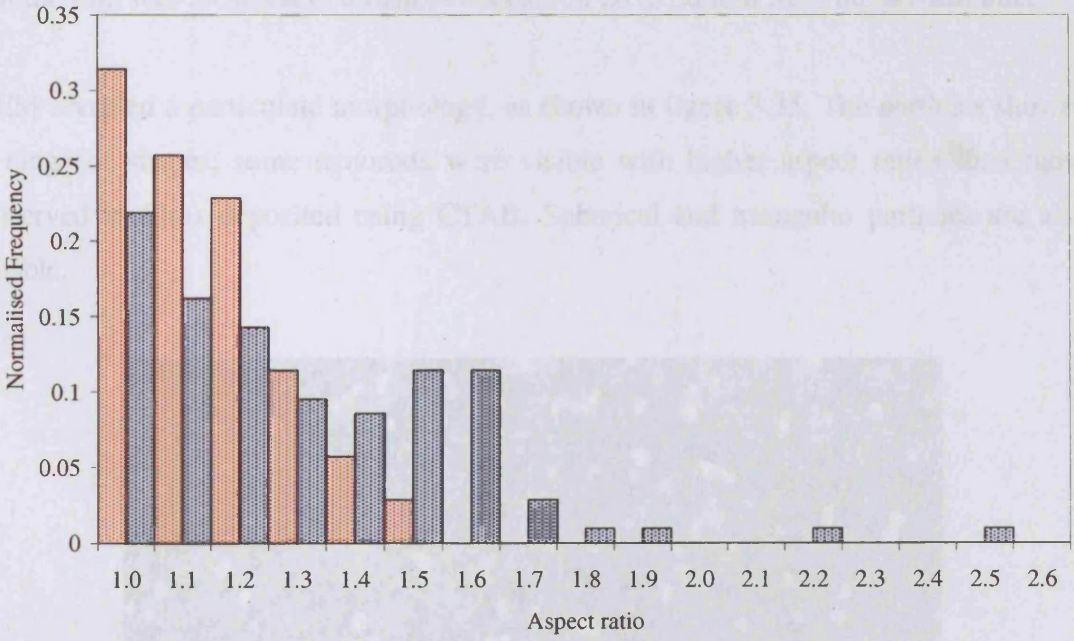

Figure 3.34. Shape distributions for gold nanoparticle films deposited from solutions containing TOAB (red) and CTAB (blue).

SEM images also show many very small particles, which are difficult to resolve and measure due to their size. They are particularly apparent in the right hand image in figure 3.33. The particles appear to be under 10 nm in size, and there appear to be no particles intermediate in size between the very small particles and the large rod-shaped particles.

3.4.3 [$HAuCl_4$] + Tetraethyl ammonium bromide (TEAB)

A deposition was carried out using a solution of HAuCl4 and TEAB, with the intention of investigating the effect of alkyl chain length on the shape directing properties of the surfactant. The alkyl chain length of the TEAB surfactant is significantly shorter than TOAB, discussed above. A precursor solution of [$HAuCl_4$] (0.040 g) and TEAB (0.09 g, 0.4 mmol) in methanol (50 mL) was prepared. The deposition was carried out at a substrate temperature of 500°C using a flow rate of 2.0 L min^{-1}. The resulting film appeared visually very similar to those deposited from [$HAuCl_4$] + TOAB. The film was blue in transmission, and gold in reflection. The entire substrate was not covered, but the film was localised to a strip of deposition 20 to 50 mm from the aerosol inlet.

SEM revealed a particulate morphology, as shown in figure 3.35. The particles showed a range of shapes; some nanorods were visible with higher aspect ratios than those observed in films deposited using CTAB. Spherical and triangular particles are also visible.

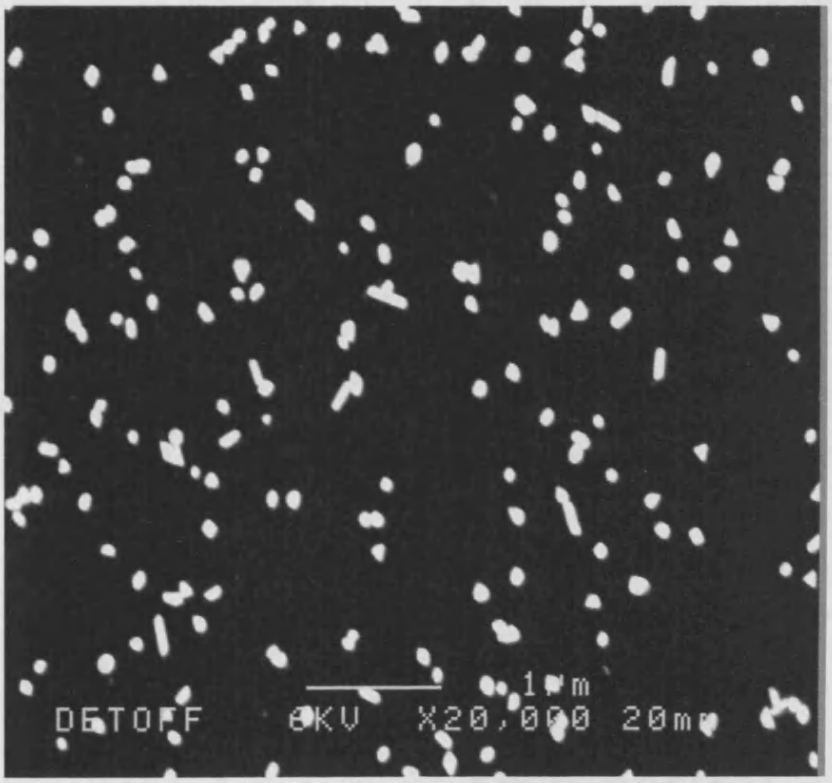

Figure 3.35 SEM (secondary electron) image of a film deposited from [$HAuCl_4$] and TEAB. The scale bar measures 1 µm.

Figure 3.36 shows the particle size and shape distributions from the images in figure 3.35. The long and short axis of each particle was measured. The particle size shown is the average of the long and short axes. The arithmetic average particle size is 103 nm, and the standard deviation is 18 nm (17 % of the mean). In the shape distribution histogram, it can be seen that while near spherical particles are present, many particles have aspect ratios between 1.3 and 2.6, and some have aspect ratios as high as 4.5. The particles are significantly more elongated than those deposited from CTAB under otherwise identical conditions.

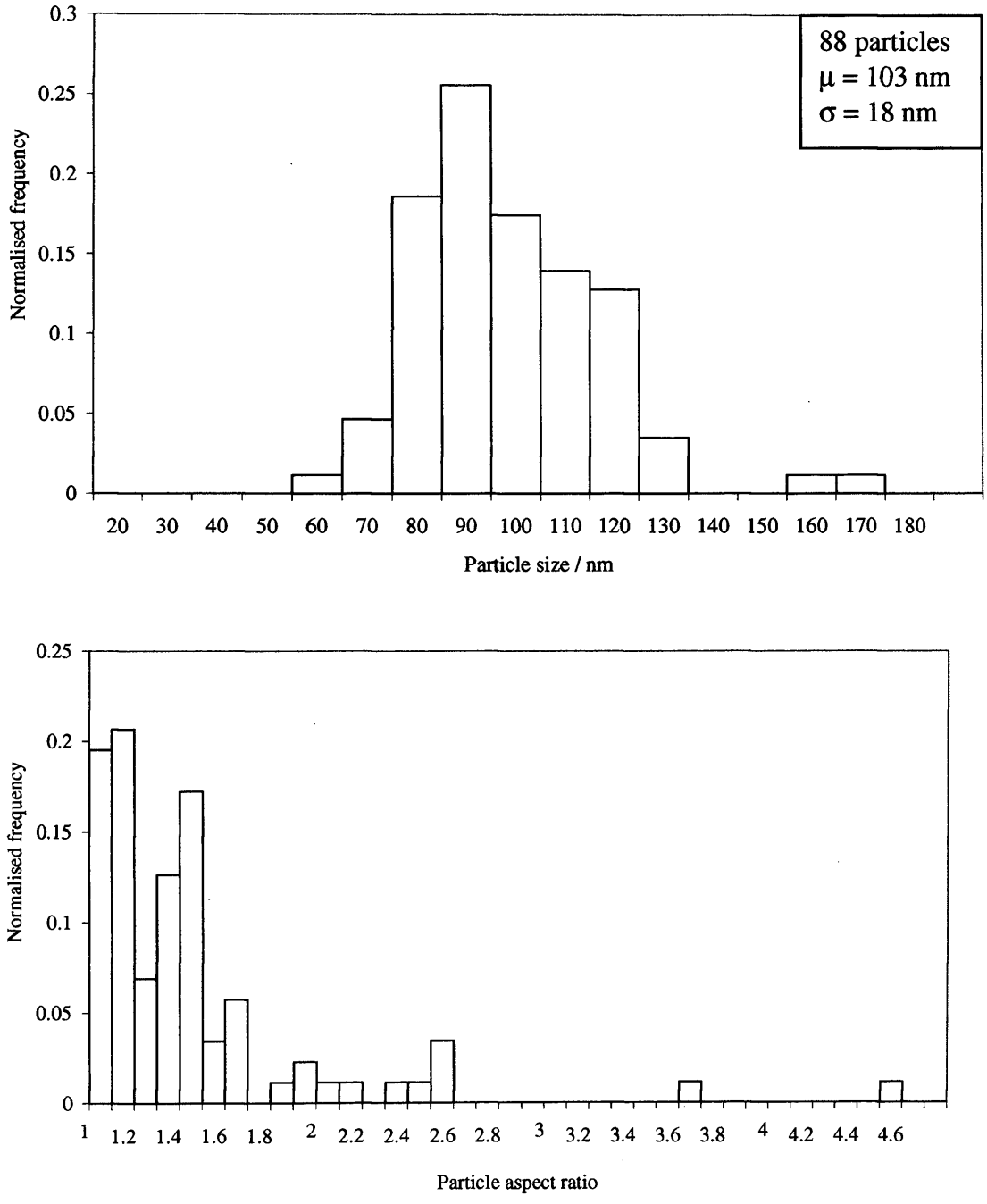

Figure 3.36. ***Top:*** **Particle size distribution for the film deposited from [$HAuCl_4$] + TEAB.** ***Bottom:*** **Particle shape distribution for the same film.**

3.4.4 Superstructures

In many of the films deposited from [$HAuCl_4$] + surfactant, linear assemblies of nanoparticles were observed by SEM on the substrate surface. Some examples of these are shown in Figure 3.37. These superstructures appeared in films deposited from each surfactant. In some cases they were around 1 μm in length, and consisted of 10 – 20 particles. In other cases, they were over 50 μm and consisted of several hundred particles.

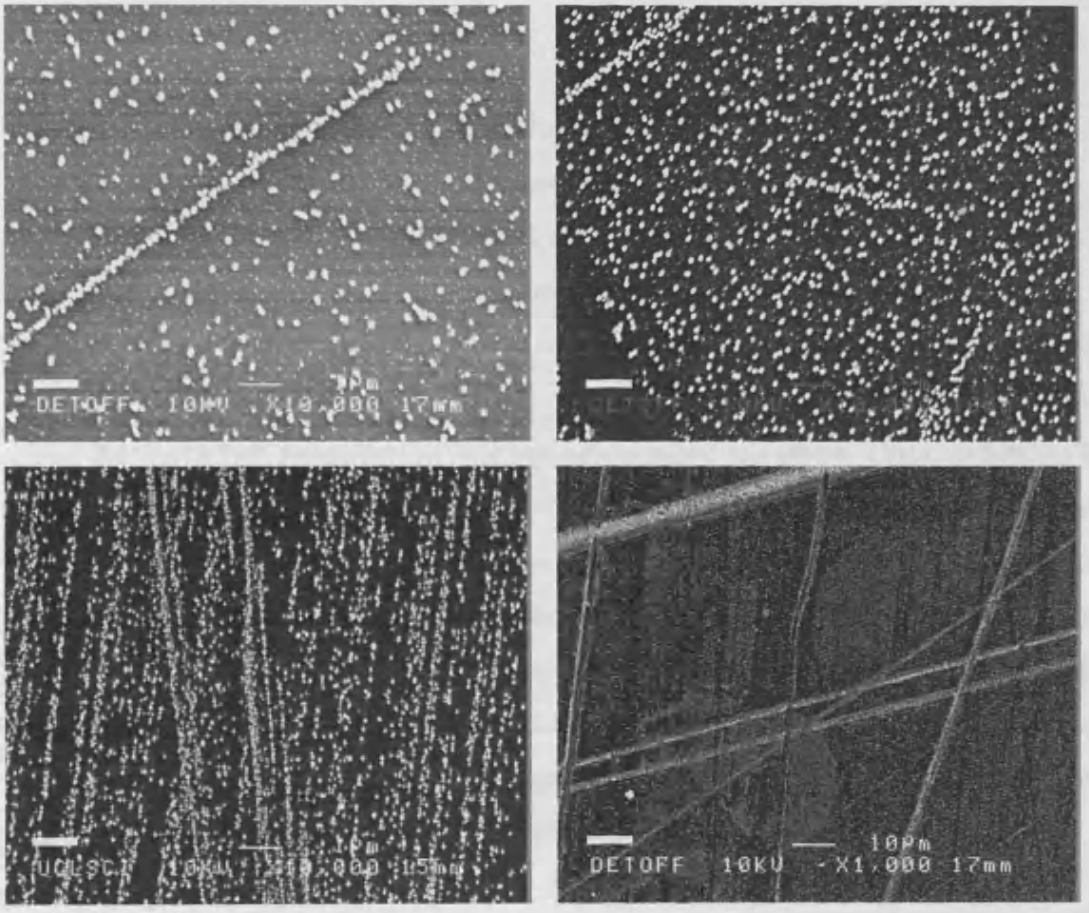

Figure 3.37. SEM (secondary electron) images of various linear superstructures of gold nanoparticles deposited from [$HAuCl_4$] + surfactant. Images are at various magnifications and scale bars (bottom left of each image) measure, clockwise from top left, 1 μm, 1 μm, 10 μm, 1 μm.

These features may form along defects in the substrate. Since the substrate is amorphous, there will be no crystal step edges. Instead, scratches caused during manufacture or handling of the glass may be the cause. If so, this suggests that the

particles are somewhat mobile on the substrate surface, to be able to find and align themselves along the scratches. An alternative explanation is that the alignment is caused by surfactant interactions. XPS has provided evidence that some surfactant molecules remain attached to the particles on the substrate. It is possible that the alignment of the metal particles is driven by van der Waals interactions between the alkane chains of the surfactants.

3.4.5 Discussion

Deposition Mechanism

It is clear from SEM images and deposition profiles derived from XRD data that the presence of surfactant molecules in the precursor solution has a profound effect on the deposition of gold films. The presence of an increasing amount of surfactant causes the point of greatest deposition to shift further from the aerosol inlet and also reduces the total amount of gold deposited. It seems, therefore, that the presence of surfactant molecules prevents [$HAuCl_4$] from reaching the substrate. One possible explanation of this is that surfactant promotes particle formation in the gas phase. Particles tend to take longer to reach the substrate in a horizontal cold wall reactor, as discussed in Chapter 1 (see figure 1.3), so this could alter the deposition profile in the manner observed experimentally. This hypothesis is supported by the observation of spherical and rod-like gold particles on the substrate. The fact that the total amount of gold deposited falls as the amount of TOAB is increased also points to gas phase particle formation, as thermophoresis tends to drive gas phase particles away from the hot substrate, meaning that less gold will be deposited onto the substrate.

Trends in Particle Size Distribution

Particle size distributions varied with amount of TOAB, deposition temperature and precursor concentration. Using 1.0, 0.5 and 0.25 g of TOAB resulted in particles with mean diameters of 95.0, 121 and 77 nm, and standard deviations of 14, 18 and 10 nm respectively. Lower amounts of TOAB resulted in films with high levels of particle agglomeration, so size distributions could not be calculated. Depositions at 500°C and 400°C led to films with mean particle sizes of 121 and 98 nm and standard deviations of 18 and 26 nm respectively. In the film deposited at 600°C, particles were agglomerated

and could not be measured accurately. Depositions carried out with 50 mL and 200 mL of solvent resulted in mean particle diameters of 121 and 65.6 nm and standard deviations of 18 and 12 nm respectively. In summary, the largest particles were produced using 0.5 g TOAB, 0.080 g [$HAuCl_4$] in 50 mL methanol at a substrate temperature of 500°C. Increasing or reducing the amount of TOAB, reducing the temperature or increasing the solvent volume appear to produce smaller particles.

Formation of Nanoparticles within the Reactor

In contrast to the use of preformed particles as precursors, which will be discussed in the following section, when using [$HAuCl_4$] in conjunction with a surfactant, the nanoparticles that result must be formed at some point during the deposition. Solutions of [$HAuCl_4$] and the surfactants used in this work are stable for many days at room temperature, and also are not visibly altered by the ultrasonic atomisation process, suggesting that it is the increased temperatures of the CVD reactor that initiate nanoparticle formation. As no *in situ* probing of the deposition process was carried out, the mechanism and location of particle formation must be deduced indirectly. Several mechanistic options can be considered based on knowledge of solution phase nanoparticle synthesis, gas phase particle growth and CVD processes:

- Micelle directed growth: Particles are formed within a micelle of surfactant molecules, which, to an extent, control the size and shape of the particle.[99, 170-172]
- Solvent Aerosol Thermolysis (SAT): The evaporation of the aerosol droplet leads to precipitation followed by reaction of the precursors, leading to hollow or solid particle formation. Particle growth is constrained by the amount of reactant present within a single aerosol droplet.[37, 39, 102, 105, 173-175]
- Charged cluster formation: Particles form in the gas phase around a charged nucleation site, which might be an ionised gas molecule.[22, 23]
- Surface island growth: Particles grow from nucleation sites on the surface of the substrate.[26, 71]

By comparison with depositions using [$HAuCl_4$] alone, it is clear that the surfactant has an important impact on the film morphology; narrowly dispersed particles are seen in depositions with surfactant present, but very wide particle size and shape distributions are observed in depositions from [$HAuCl_4$] alone. In addition, the use of CTAB and TEAB has been shown to specifically affect the shape of the nanoparticles, causing the

deposition of elongated nanorods. It is also observed that the diffusion of [$HAuCl_4$] to the substrate, which is presumably behind the growth of films from [$HAuCl_4$] alone, is suppressed when surfactant is present. Consequently, the correct mechanism must explain these differences. Micelle directed growth is the obvious choice, as this mechanism requires the surfactant molecules to form the micelle. Additionally, this is the mechanism that operates in the solution phase syntheses of gold particles which use surfactants. The difference in nanoparticle shape between depositions using CTAB and TOAB is strong evidence that nanoparticle growth is directed by the surfactant capping groups. Since a solvent is required to form a micelle, the growth of nanoparticles through this method must occur within the aerosol droplets before they vapourise.

The SAT mechanism has been shown to be capable of producing monodisperse particles of a variety of materials.[37, 39] Monodisperse SAT particles form from the contents of a single aerosol droplet. Since the size and solute concentration of the aerosol droplets is known for each deposition, the mass of gold in a single aerosol droplet can be calculated. From this, the size of a spherical gold particle produced from the contents of a single aerosol droplet can be determined. Table 3.1 shows two such calculations, on films deposited from identical quantities of [$HAuCl_4$] and TOAB in 50 mL and 200 mL of solvent.

Aerosol droplet radius / m	Aerosol droplet volume / m^3	Aerosol droplet volume / mL
2.4×10^{-5}	5.79×10^{-14}	5.79×10^{-8}

Deposition	[$HAuCl_4$] / g	Volume solvent / mL
I	0.080	200
II	0.080	50

Deposition	Mass of [$HAuCl_4$] in 1 mL / g	Mass of [$HAuCl_4$] in each aerosol droplet / g	Mass of Au in each aerosol droplet / g	Theoretical Au particle volume / m^3	Theoretical Au particle diameter / nm	Actual mean Au particle diameter / nm
I	4.0×10^{-4}	2.3×10^{-11}	1.2×10^{-11}	6.0×10^{-19}	1040	66
II	1.6×10^{-3}	9.2×10^{-11}	4.6×10^{-11}	2.4×10^{-18}	1660	95

Table 3.1. ***Top:*** **Calculations of the aerosol droplet volume, based on the Lang diameter calculated for methanol given in Table 1.1.** ***Middle:*** **Relevant parameters of two depositions.** ***Bottom:*** **Calculations to determine the spherical particle size obtained when formed from the contents of a single aerosol droplet. The actual particle size obtained in these depositions is also given, for comparison.**

There is a large discrepancy between the theoretical and observed particle size. If gold particles formed from the entire contents of an aerosol droplet, then they would be expected to be over 1 μm in diameter, even for the lowest precursor concentration used. The actual particle diameters observed were under 100 nm. This seems to show that several separate particles are produced from the contents of each aerosol droplet. While it is possible for several crystallites to form from one droplet in SAT, for example if the evaporation rate or solute concentration is high, these are thought to always agglomerate to form a single polycrystalline particle.[36, 176, 177] Furthermore, it is hard to explain why the surfactant is necessary, *i.e.* why this SAT mechanism does not occur in depositions with [$HAuCl_4$] alone.

Gas phase charged cluster formation is known to occur in deposition of gold, but the gold clusters observed were around 2 nm, very much smaller than those observed to be deposited by CVD. Additionally, the role of the surfactant in this mechanism is unclear.

It seems that the micelle growth mechanism is the strongest candidate for the growth mechanism of gold particles within the reactor. This suggests that the particles are formed in solution, within the aerosol droplets before solvent evaporation. As stated in Chapter 1, the evaporation lifetime of a volatile aerosol droplet can be of the order of milliseconds.[30] Solution phase nanoparticle growth using similar surfactants can be very rapid, but these syntheses use strong reducing agents, such as sodium borohydride to initiate the reaction.[82] The solution phase synthesis of nanoparticles using principally thermal energy is known as solvothermal synthesis. The solvothermal synthesis of gold particles has been reported, by heating a toluene solution of [$HAuCl_4$] to 160°C in the presence of oleylamine, a weak reducing agent.[100] However, the nanoparticle growth took over 30 minutes, much longer than the aerosol droplet lifetime. It is also doubtful whether the aerosol droplet temperature will reach 160°C before total evaporation occurs, considering the much lower boiling point of methanol (65°C). It may be that the high solute concentration within the droplet sufficiently depresses the solvent vapour pressure to significantly extend the droplet lifetime, or that the surfactant or indeed the solvent acted as a reducing agent, enabling reaction of the precursor at a lower temperature. It may also be the case that nanoparticle growth can continue even after evaporation of the droplet, and is controlled by the adsorbed surfactant molecules. XPS analysis of films deposited from [$HAuCl_4$] + TOAB suggested that at least some surfactant molecules were present on the surface, which leaves the possibility open that

micellar growth continues in the gas phase, although no such mechanism has been previously reported for a nanoparticle system. Figure 3.38 shows a summary of the proposed nanoparticle formation mechanism discussed in this section. A less speculative determination of the nanoparticle formation mechanism is unfortunately not possible with the information available, and will probably require *in situ* measurements during the deposition process.

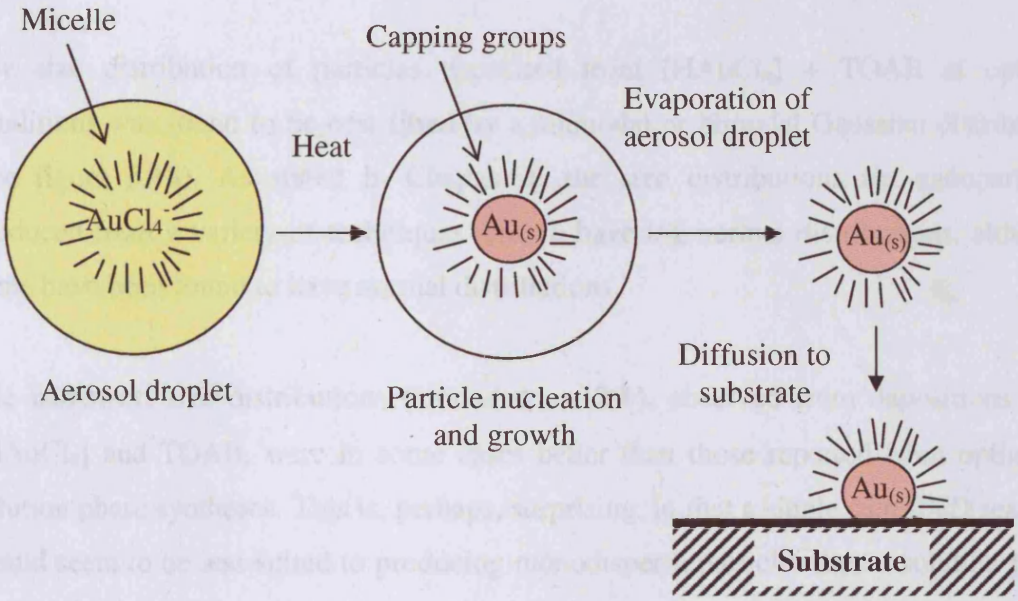

Figure 3.38. Suggested surfactant directed particle formation mechanism within the reactor.

A further issue is the apparent discontinuity in the size distributions of some of the films investigated. As can be seen in figure 3.18, some films contained apparently separate distributions of smaller (*circa* 10 nm) and larger (*circa* 100 nm) particles with very few particles of intermediate size. Bimodal Gaussian distributions were fitted to these experimental data. The presence of two seemingly distinct distributions of particles may correspond to the 'primary' and 'secondary' particles described in LaMer's model for particle nucleation and growth.[90] In this model, primary particles formed by initial rapid homogeneous reaction, while secondary particles formed through a slower process of heterogeneous growth, using a primary particle as a nucleus. Later work showed that in some cases, growth of secondary particles proceeds through agglomeration of primary particles.[89] The smaller particles observed in some films may be primary particles that were deposited onto the substrate before particle growth through agglomeration or

heterogeneous reaction could occur. Furthermore, XRD data showed that the crystallite size in these films was close to that of the small particles observed, meaning that these particles could be single crystals, which is expected of primary nucleated particles.[90] The reduction in number of these smaller particles along the length of the substrate would then represent the ongoing growth process within the reactor.

Nanoparticle Size Distributions

The size distribution of particles deposited from [$HAuCl_4$] + TOAB at optimal conditions was found to be best fitted by a unimodal or bimodal Gaussian distribution (see figure 3.18). As stated in Chapter 1, the size distributions for nanoparticles produced from a variety of techniques tend to have log-normal distributions, although some have been found to have normal distributions.

The narrowest size distributions (around σ = 12%), observed from depositions with [$HAuCl_4$] and TOAB, were in some cases better than those reported from optimised solution phase syntheses. This is, perhaps, surprising, in that a single step CVD reaction would seem to be less suited to producing monodisperse particles than a solution phase synthesis. To attempt to explain the narrow size distributions observed, a simple model of gas phase particle behaviour within the reactor was developed.

The deposition of particles from the gas phase depends on the balance of thermophoresis and diffusion (figure 1.3).[21, 24] Thermophoresis is almost size independent for nano-sized particles, whereas diffusion is strongly size dependent, and is greater for smaller particles. The process of particle deposition in the CVD reactor was modelled qualitatively by taking a population of particles with a log-normal size distribution and applying thermophobic thermophoresis and diffusion forces to them. A one dimensional reactor was used in the model, and any particles accelerated towards the substrate by the balance of forces acting on them were considered to be deposited onto the substrate. The log-normal probability density function was used as the size distribution of the gas phase particles, $f_{GP}(d_p)$, where d_p is the particle diameter. Thermophoresis was modelled as size independent, as observed experimentally[21, 24] and predicted by more detailed theoretical treatments.[9] Diffusion was modelled according to equation 1.2 (Chapter 1) as inversely proportional to particle size. The total force, F_P, and acceleration, a_P on each particle was calculated as follows:

$$F_P(d_p) = D(d_p) - S \tag{3.5}$$

$$m(d_p) \propto d_p^3 \tag{3.6}$$

$$a_p(d_p) = \frac{F_P(d_p)}{m(d_p)} \tag{3.7}$$

where $D(d_p)$ and S are the force due to diffusion and thermophoresis respectively and $m_p(d_p)$ is the mass of the particle. Since these are the two most important forces that act on a gas phase particle, other forces are not considered. Assuming uniform density of the particles, d_p^3 is proportional to $m_p(d_p)$. The size distribution of the particles adsorbed on the substrate, $f_{Ad}(d_p)$, was calculated as follows:

$$f_{Ad}(d_p) = f_{GP}(d_p) \times a_p(d_p) \tag{3.8}$$

For particle sizes where $D(d_p) < S$, the corresponding value of $f_{Ad}(d_p)$ will be negative. This shows that particles are repelled from the substrate due to thermophoresis. Therefore only the positive portion of $f_{Ad}(d_p)$ represents particles deposited on the substrate. Figure 3.39 shows the size distributions calculated for particles in the gas phase and adsorbed on the substrate, using the arbitrary constants chosen. If large values of S were used, then no particle reached the substrate due to strong thermophoresis. If constants were chosen giving large values of $D(d_p)$ then all the gas phase particles reached the substrate, so there was no difference in gas phase and adsorbed particle size distributions. The model shown in figure 3.39 illustrates the intermediate case where only a proportion of the gas phase particles are deposited.

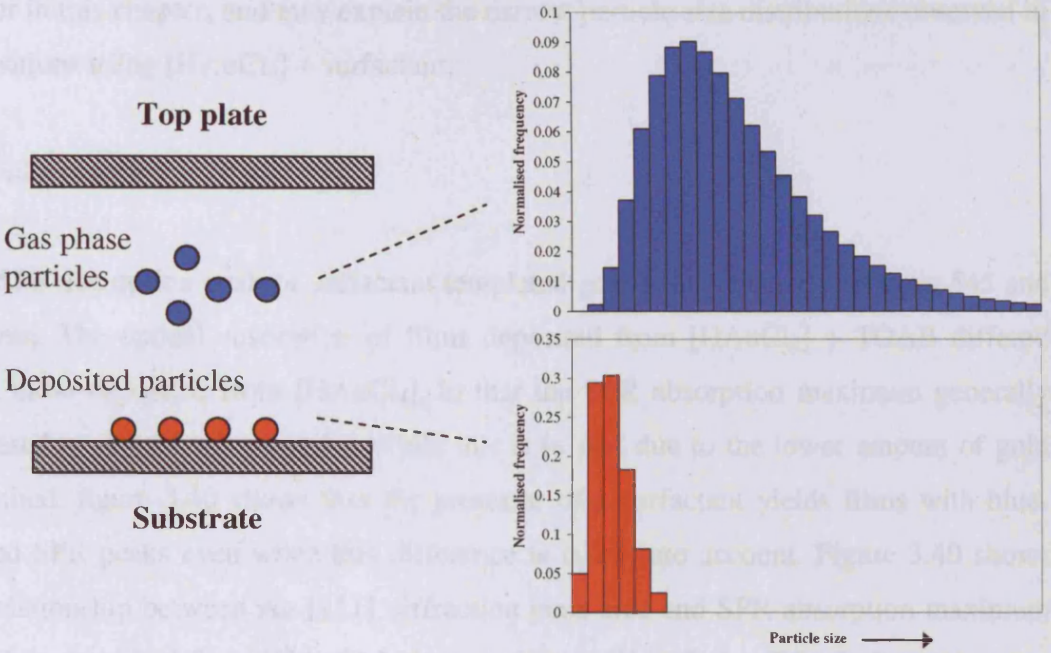

Figure 3.39. Model of particle deposition under the influence of thermophoresis and diffusion. Thermophoresis is assumed to be thermophobic and independent of size. Diffusion is modelled as inversely proportion to particle diameter in accord with equation 1.2. Right: Size distributions of particles in the gas phase (blue) and deposited onto the substrate (red). An initial log-normal size distribution is assumed in the gas phase. The size distribution of the deposited particles appears more like a Gaussian distribution.

As can be seen in figure 3.39, the inverse dependence of diffusion on particle size results in smaller particles experiencing higher diffusion forces, and arriving in greater quantity at the substrate. The size distribution of particles on the substrate is significantly different from that in the gas phase. The mean particle size is shifted to a lower value, and the arithmetic standard deviation is smaller. The size distribution of deposited particles also appears much more symmetric and Gaussian-like than the log-normal gas phase distribution. While it should be remembered that the magnitudes of the forces in this qualitative model are arbitrarily assigned, it is clear that in principle it is possible for a 'size focussing' effect to occur on particles in a cold wall CVD reactor, whereby a relatively broad gas phase particle size distribution is transformed to a much narrower distribution on the substrate, accompanied by a change from a log-normal to a Gaussian-like distribution. This correlates well with the experimental results presented

earlier in this chapter, and may explain the narrow particle size distributions observed in depositions using $[HAuCl_4]$ + surfactant.

Optical Absorption

The SPR absorption peak of surfactant templated gold films occurred between 545 and 800 nm. The optical absorption of films deposited from $[HAuCl_4]$ + TOAB differed from those deposited from $[HAuCl_4]$, in that the SPR absorption maximum generally appeared at shorter wavelengths. While this is in part due to the lower amount of gold deposited, figure 3.40 shows that the presence of a surfactant yields films with blue-shifted SPR peaks even when this difference is taken into account. Figure 3.40 shows the relationship between Au [111] diffraction peak area and SPR absorption maximum for films deposited from $[HAuCl_4]$ alone and from $[HAuCl_4]$ + TOAB. It can be seen that, in general, depositions using TOAB lead to a blue shifted SPR absorption peak, even when films with similar diffraction peak area are compared.

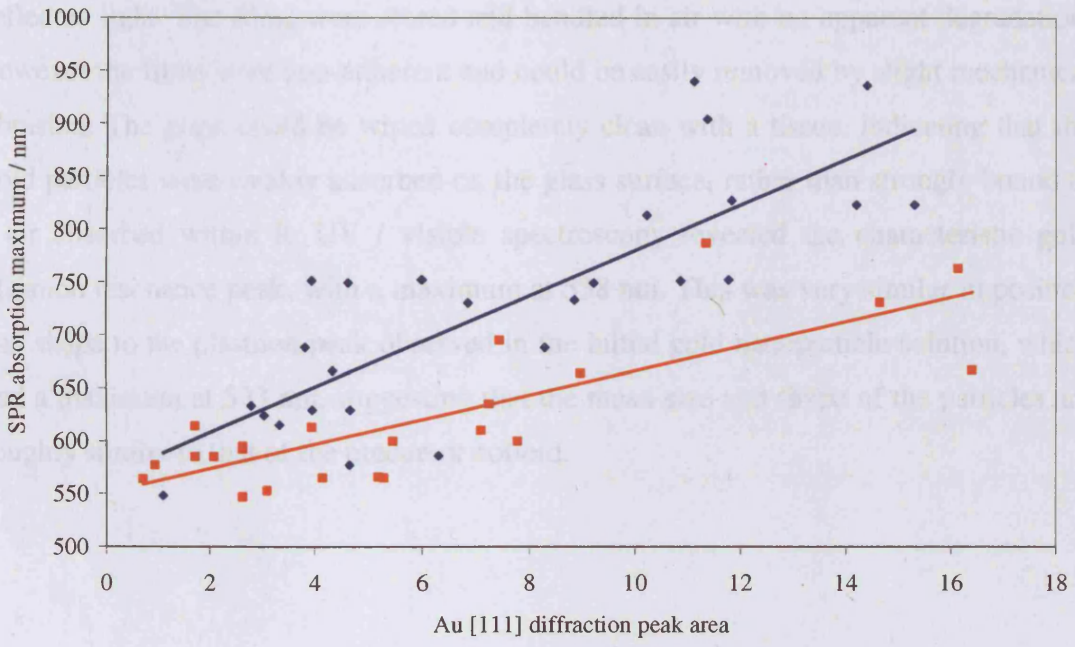

Figure 3.40. Relationship between Au [111] diffraction peak area and SPR absorption maximum for films deposited from $[HAuCl_4]$ alone (blue points) and from $[HAuCl_4]$ + TOAB (red points). Best linear fits to each data set are shown.

This apparent difference in optical absorption between surfactant and non-surfactant deposited films may be due to the nanostructure. SEM imaging shows that films deposited in the presence of TOAB are composed of seemingly un-agglomerated

spherical particles. It has been previously observed that assemblies of layered spherical gold nanoparticles show only a small red shift in SPR compared with a continuous gold film of similar thickness.[178]

3.5 Depositions using Gold Nanoparticle Solution

Films were deposited from toluene solutions of pre-formed gold nanoparticles, the synthesis of which is described at the beginning of this chapter. The deposition was carried out as follows. The precursor solution was made up of pre-formed gold nanoparticles in toluene (10 mL) diluted with toluene to 50 mL. It was found that if higher precursor concentrations were used, the gold particles precipitated under the action of the ultrasonic atomiser after a short time. A substrate temperature of 450°C and a flow rate of 0.8 L min^{-1} were found to give the best substrate coverage.

The resulting gold nanoparticle films appeared red to transmitted light and yellow to reflected light. The films were stored and handled in air with no apparent degradation, however the films were non-adherent and could be easily removed by slight mechanical abrasion. The glass could be wiped completely clean with a tissue, indicating that the gold particles were weakly adsorbed on the glass surface, rather than strongly bound to it or absorbed within it. UV / visible spectroscopy revealed the characteristic gold plasmon resonance peak, with a maximum at 538 nm. This was very similar in position and shape to the plasmon peak observed in the initial gold nanoparticle solution, which had a maximum at 533 nm, suggesting that the mean size and shape of the particles are roughly similar to that of the precursor colloid.

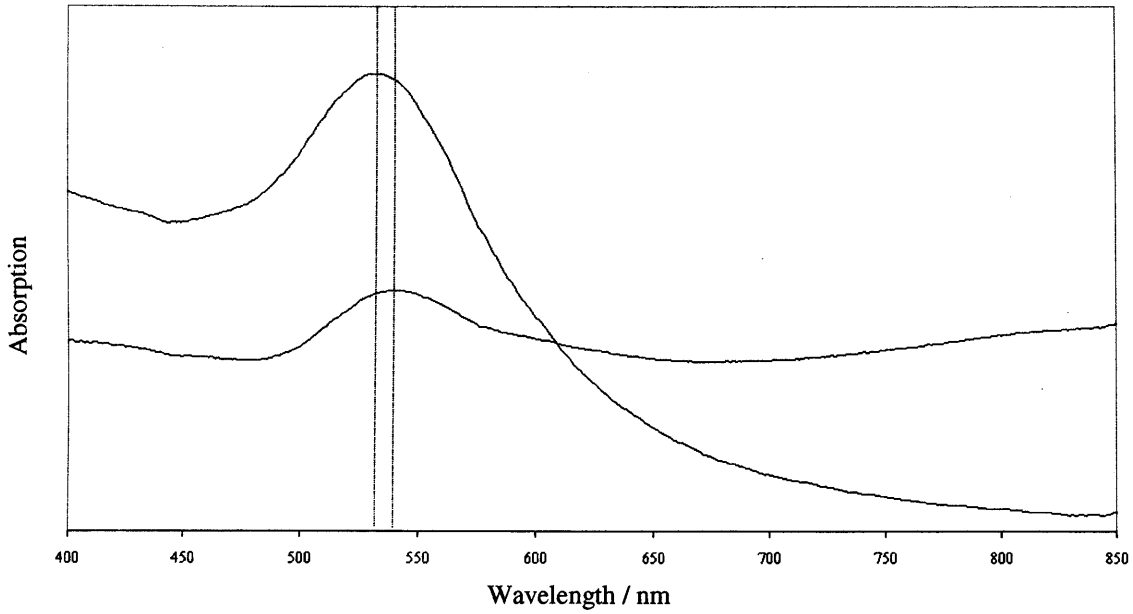

Figure 3.41. UV / visible spectra of pre formed gold nanoparticles in toluene (top) and a film deposited from these particles via AACVD (bottom). The positions of the SPR peak maxima are indicated by vertical lines.

XPS confirmed the presence of gold within the film. Au $4f_{5/2}$ and $4f_{7/2}$ photoelectron peaks appeared at binding energies of 87.5 eV and 83.7 eV respectively, corresponding to metallic gold.[163] SEM confirmed the presence of individual nanoparticles on the surface of the film. Some particles seem to be agglomerates of two, three or more smaller particles. A typical SEM image is shown in figure 3.42. In some cases, the particles appear unagglomerated. In other places, two or three particles can be observed in close proximity but not conjoined. Bare glass is visible between the particles, showing that less than one monolayer has been deposited. The particles appear randomly distributed and roughly spherical. The particle size distribution was measured manually, and is shown in figure 3.43.

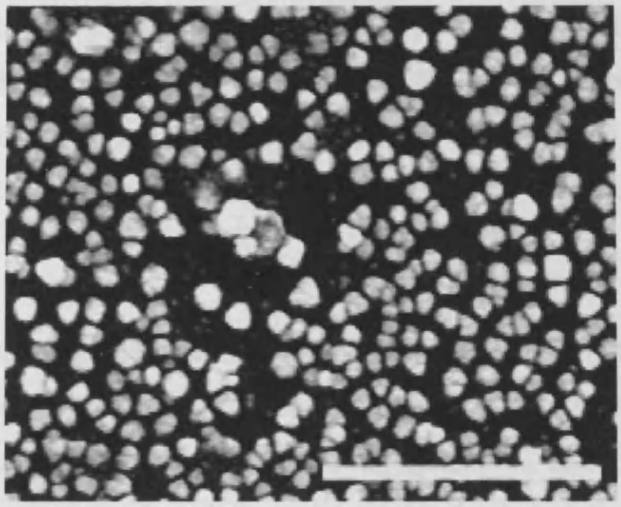

Figure 3.42. SEM (secondary electron image) of a film deposited from pre-formed gold particles in toluene. Scale bar measures 1 μm.

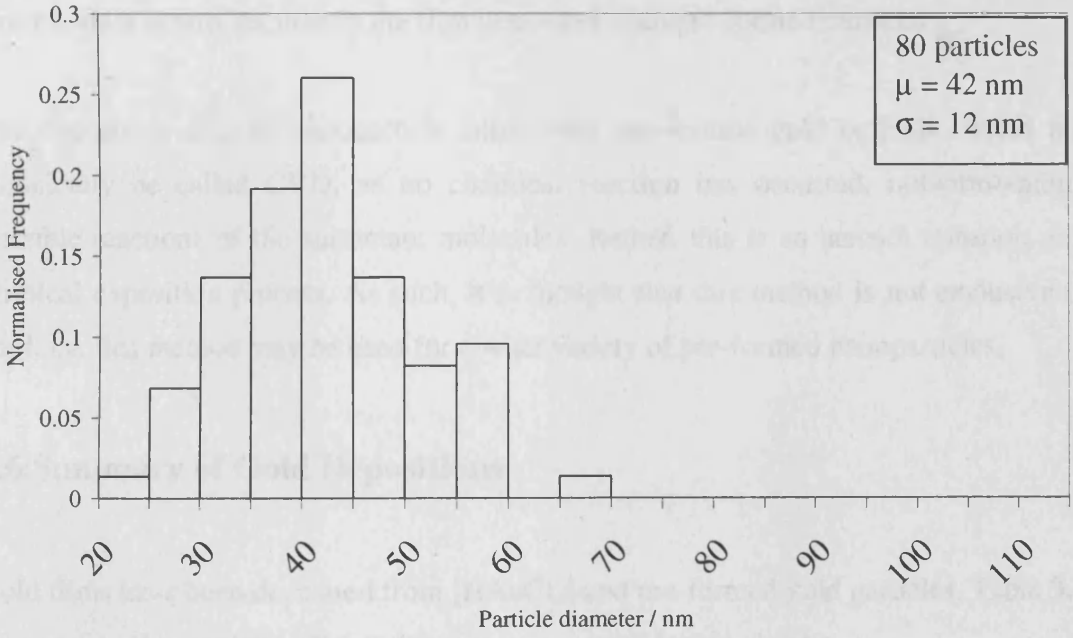

Figure 3.43. Size distribution for a gold nanoparticle film deposited from pre formed gold particles in toluene solution. The arithmetic mean and standard deviation are shown, inset.

3.5.1 Discussion

As already discussed in this chapter, the deposition of nanoparticles from the gas phase in a laminar flow cold wall CVD reactor depends on the balance of thermophoresis and diffusion. The deposition using pre-formed gold nanoparticles shows that for particles around 40 nm in size, deposition from the gas phase to a hot substrate is possible. The SPR wavelength of the gold nanoparticle film is very similar to that of the precursor

solution. The slight red-shift may be due to close spacing of the particles, slight agglomeration leading to increased particle size. The mean refractive index of the surroundings for particles supported on glass is very similar to the refractive index of toluene (n = 1.45), so a change in refractive index is probably not the reason for the red-shift.[179]

The mean size of the deposited particles is considerably smaller than that achievable using [$HAuCl_4$] and a surfactant, and hence this method may be suitable where very small particles are required. It is interesting to note, however, that the absolute standard deviation of particle sizes in films deposited from pre-formed particles and [$HAuCl_4$] + TOAB are very similar (12 nm and 18 nm) respectively. Because the particles deposited from [$HAuCl_4$] + TOAB were considerably larger, the relative standard deviation of particle sizes is smaller than in the film deposited from pre-formed particles.

The deposition of gold nanoparticle films from pre-formed gold colloids should not technically be called CVD, as no chemical reaction has occurred, notwithstanding possible reactions of the surfactant molecules. Rather, this is an aerosol transport and physical deposition process. As such, it is thought that this method is not exclusive to gold, *i.e.* this method may be used for a wide variety of pre-formed nanoparticles.

3.6 Summary of Gold Depositions

Gold films have been deposited from [$HAuCl_4$] and pre-formed gold particles. Table 3.2 summarises the more significant depositions reported in this chapter.

Gold precursor, amount	Second precursor, amount	Substrate Temperature / °C	Solvent volume / mL	SPR peak range / nm	Mean particle size / nm	Particle size standard deviation / nm	Mean particle aspect ratio	Substrate coverage
$[HAuCl_4]$, 0.080 g	none	500	50	830 - 630	*a*	*a*	*a*	0 – 60 mm
		500	12.5	1000 - 705	*a*	*a*	*a*	0 - 60 mm
		500	200	820 - 605	*a*	*a*	*a*	0 – 60 mm
$[HAuCl_4]$ 0.080 g	TOAB 1.0 g	500	50	610 - 550	95.0	14 (15 %)	*a*	20 – 60 mm
	TOAB 0.5 g	500	50	640 - 550	121	18 (15 %)	1.1	10 – 60 mm
	TOAB 0.25 g	500	50	640 - 560	77.0	10 (13 %)	*a*	0 – 60 mm
	TOAB 0.12 g	500	50	695 - 555	*a*	*a*	*a*	0 – 60 mm
	TOAB 0.06 g	500	50	800 - 605	*a*	*a*	*a*	0 – 60 mm

Table 3.2. Summary of depositions of gold films. *a* not measured

Gold precursor, amount	Second precursor, amount	Substrate Temperature / °C	Solvent volume / mL	SPR peak range / nm	Mean particle size / nm	Particle size standard deviation / nm	Mean particle aspect ratio	Substrate coverage
$[HAuCl_4]$, 0.080 g	TOAB 0.5 g	600	50	610 - 550	*a*	*a*	*a*	20 – 60 mm
	TOAB 0.5 g	400	50	572 - 533	97.9	26 (27 %)	*a*	30 – 90 mm
	TOAB 0.5 g	500	200	695 - 550	65.6	12 (18 %)	*a*	10 – 70 mm
	CTAB 0.5 g	500	50	650 - 554	136	28 (21 %)	1.3	10 – 60 mm
	TEAB 0.09 g	500	50		103	18 (17 %)	*a*	10 – 60 mm
Gold nanoparticles	-	500	50	535	42	12 (29 %)	1.0	5 – 30 mm

Table 3.2. Summary of depositions of gold films, continued. *a* not measured

3.7 Comparison with Previous Work

Deposition of gold films by CVD has been reported using organogold precursors, a survey of which is given in Chapter 1 (table 1.3). These depositions are usually carried out at reduced pressure, due to the poor volatility of the precursors.[147, 148] In comparison, [$HAuCl_4$] is a significantly cheaper and easier to prepare precursor, and is easier to handle than most organogold complexes.[1] Furthermore, the AACVD technique described in this chapter is performed at atmospheric pressure, which may be an advantage if applied in an industrial setting. Only very few reports of deposition of nanostructured gold films by CVD have been made. In one example, gold films were deposited from [$MeAuPMe_3$] onto a template made up of polymer spheres; when the template was removed, a macroporous film gold remained.[146] While only one diameter of polymer sphere was investigated (500 nm), presumably this method would work with a range of template sizes, allowing tailoring of the film structure. However, the formation of the template prior to deposition, and the post deposition annealing needed to remove the polymer compare unfavourably with the one step methods described here. Further investigations into the nanostructure of gold films deposited by CVD are not available, so it is impossible to compare the merit of the [$HAuCl_4$] + surfactant or pre-formed gold nanoparticle precursor systems with previous CVD studies. However, several other methods have been used to deposit nanostructured gold films. Thermal evaporation of gold at reduced pressure is a common method for the production of thin gold films.[69, 73] In some cases the substrate is modified to improve gold adhesion, especially for very thin films.[71] The films typically show island growth morphology. Suitably thin gold films show SPR absorption, with maxima occurring from 600 – 800 nm, depending on deposition time (see figure 1.14).[73] This range is comparable to the range of SPR peaks seen in films deposited by CVD from [$HAuCl_4$]. A drawback of the thermal evaporation method is the inability to control the island size, coverage and island separation independently. A common alternative strategy is the deposition of particles from aqueous or organic solution onto a suitably prepared substrate.[5, 180] Gold particles have been deposited onto glass pre-treated with $SnCl_2$ from a solution of [$HAuCl_4$] and hydrazine using this method.[179] Nucleation occurred heterogeneously on the substrate surface, followed by hydrazine induced particle growth. Particles have also been assembled on a substrate through alternate application of nanoparticle solution and dithiol spacer groups, which allows greater than one monolayer coverage.[178] These

methods offer better control over particle size and shape, and to some extent, film coverage, compared with thermal evaporation.

The CVD techniques for the deposition of gold described in this thesis hold several advantages over the other deposition techniques mentioned, namely rapid, single step deposition at atmospheric pressure, with the potential for facile industrial integration. It has also been shown that a range of particle sizes with narrow size distributions can be deposited using AACVD. An additional advantage, which will be explored in the next chapter, is the ability to combine the gold precursors discussed here with other CVD precursors to produce composite films.

3.8 Conclusion

Gold films have been deposited from two new CVD precursors. [$HAuCl_4$] is an excellent CVD precursor to metallic gold films, which has thus far been overlooked due to its poor volatility. In comparison with previously used gold CVD precursors, such as the organogold complexes listed in Table 1.3, [$HAuCl_4$] is cheap and easy to handle. Gold films with a variety of morphologies can be deposited. The optical absorption of the films, caused by SPR, is related to the amount of gold deposited and the nanostructure. Surfactants can be used in conjunction with [$HAuCl_4$] to deposit particulate films, and the size and shape of the gold particles can be controlled to some extent. It has been shown that the techniques developed for solution phase synthesis of nanoparticles can be adapted for AACVD. Furthermore, the results presented in this chapter are strong evidence that solution phase reactions do occur within the aerosol droplets in AACVD, despite the short lifetime of droplets within the reactor.

In addition AACVD is shown to be a versatile technique, able to deposit films from precursors quite unsuitable for almost any other variant of CVD. Pre formed gold particles are an example of this type of precursor. While the deposition of pre-formed particles is a physical rather than a chemical process, it is thought that many other types of pre-formed nanoparticles might be used in similar depositions to deposit a range of films unavailable through other CVD or PVD techniques.

Chapter 4: Deposition of Nanocomposite Films

4.1 Introduction

This chapter describes the deposition of nanocomposite films, *i.e.* films of transition metal oxides with incorporated gold nanoparticles, and their optical and other properties. In Chapter 3, films deposited from two novel gold precursors were reported. Nanocomposite films were deposited in a single step deposition using these gold precursors and a metal oxide precursor dissolved in the same precursor solution. Either [$HAuCl_4$] or pre-formed gold colloids were used as the gold precursor, and a variety of transition metal carbonyls, alkoxides and aryloxides were used as metal oxide precursors. In some cases, deposition parameters were altered and different solvents were used in order to accommodate the metal oxide precursors.

4.2 Precursors

4.2.1 Gold Precursors

The gold precursors used in the depositions described in this chapter ([$HAuCl_4$] and pre-formed gold nanoparticles) have already been described in Chapter 3, section 3.2.

4.2.2 Metal Oxide Precursors

$Ti(O^iPr)_4$

Titanium(IV) isopropoxide is a viscous liquid soluble in polar and non-polar solvents. It reacts rapidly with water and Brondstead acids eventually forming TiO_2 and isopropanol.[181] It has previously been used to deposit TiO_2 films using a variety of CVD methods, including APCVD and LPCVD.[182-184] $Ti(O^iPr)_4$ (97 %) was purchased from Aldrich Chemical Company and used as received.

$W(OPh)_6$

Tungsten hexaphenoxide is a dark red solid highly soluble in acetone and methanol, and somewhat soluble in other polar solvents. $W(OPh)_6$ was synthesised by the reaction of WCl_6 and phenol, as described by Cross *et al.*:[44]

$$WCl_6 + 6\ C_6H_5OH \rightarrow W(OPh)_6 + 6\ HCl$$

Tungsten hexachloride (10.0 g, 25 mmol) was dissolved in toluene (250 mL), and phenol (14.1 g, 150 mmol) was added. The reaction mixture was refluxed under nitrogen for 15 hours, and then the solvent was removed by vacuum leaving a dark red solid. This was heated for three hours to drive off unreacted phenol. The product was dissolved in ether and washed with dilute aqueous NaOH solution to remove unreacted HCl. The ether was removed by vacuum, yielding the product, a dark red solid.

Tungsten hexaphenoxide and its fluorinated derivatives has been used as an AACVD precursor to WO_3 and partially reduced WO_{3-x} films.[44]

$W(CO)_6$

Tungsten hexacarbonyl is a white solid somewhat soluble in methanol and ethanol. It is volatile and sublimes at 150°C, and has previously been used as an APCVD and LPCVD precursor to deposit tungsten metal and WO_{3-x}.[185, 186] Tungsten hexacarbonyl is thought to decompose at high temperature through loss of CO. The formal oxidation state of the metal (zero) and the lack of metal-oxygen bonds means that this precursor is capable of depositing tungsten metal. An oxygen source or post deposition annealing is required to obtain films of tungsten oxide.[187]

Tungsten hexacarbonyl (97%) was obtained from Aldrich Chemical Company and used as received.

$Mo(CO)_6$

Molybdenum hexacarbonyl is a white solid somewhat soluble in methanol and ethanol. Like its tungsten analogue, molybdenum hexacarbonyl is volatile and sublimes at

150°C. Molybdenum hexacarbonyl has been used as an APCVD precursor to molybdenum metal and MoO_3 films.[188, 189]

Molybdenum hexacarbonyl (97 %) was obtained from Aldrich Chemical Company and used as received.

4.2.3 Precursor Compatibility

It was found that successful depositions could not be carried out from mixtures containing $M(CO)_6$ (M = W, Mo) and either TOAB or preformed gold particles. It is thought that this is due to reaction between the metal carbonyl and the quaternary ammonium salt.[190]

$$M(CO)_6 + R_4N^+X^- \rightarrow R_4N^+[M(CO)_5X]^- + CO$$

4.3 Depositions using Gold Colloid + Metal Oxide Precursor

4.3.1 Gold Colloid + $Ti(O^iPr)_4$

Depositions were carried out using gold colloid solutions in toluene mixed with $Ti(O^iPr)_4$. Gold colloid stock solutions (4.3 mM Au) were prepared by the Brust-Schriffin method as described in Chapter 3.[82] As an initial investigation, 4.0 mL of this stock solution were taken and made up to 50 mL with toluene, then $Ti(O^iPr)_4$ (0.28 g, 1.0 mmol) was added. Thus the initial film was deposited from a precursor solution with Ti : Au ratio 60 : 1. A substrate temperature of 450°C and a gas flow rate of 2.0 L min^{-1} were used. The resulting film appeared pale blue in transmitted light, with a slight metallic lustre in reflected light. Interference fringes were present, which are caused by variable film thickness and have been previously been observed in titania films deposited by CVD.[191] The film was strongly adherent to the glass, such that it could not be removed by vigorous rubbing with tissue paper and was undamaged in routine handling.

UV / vis spectroscopy of the TiO_2 / Au composite film showed absorption peaks in the region of 580 nm which are assigned to the red shifted and broadened plasmon resonance of gold nanoparticles (Figure 4.1). The gold nanoparticles could not be

removed from the TiO_2 / Au composite film by immersion in common organic solvents or water, or by abrasion, as indicated by the persistence of the plasmon absorption peak after these treatments. Indeed, the gold particles could not be removed by any physical method that did not also remove the titania film, showing that the nanoparticles are either strongly bound to the film or firmly contained within it.

The visible absorption spectrum consisted of a single SPR peak with maximum at 580 nm. The SPR peak is considerably red-shifted compared to that observed in the precursor solution (λ_{max} = 533 nm); this can be explained by incorporation of the particles within a matrix of a high refractive index, but may also be due to an increase in particle size or interaction between closely spaced particles.[192]

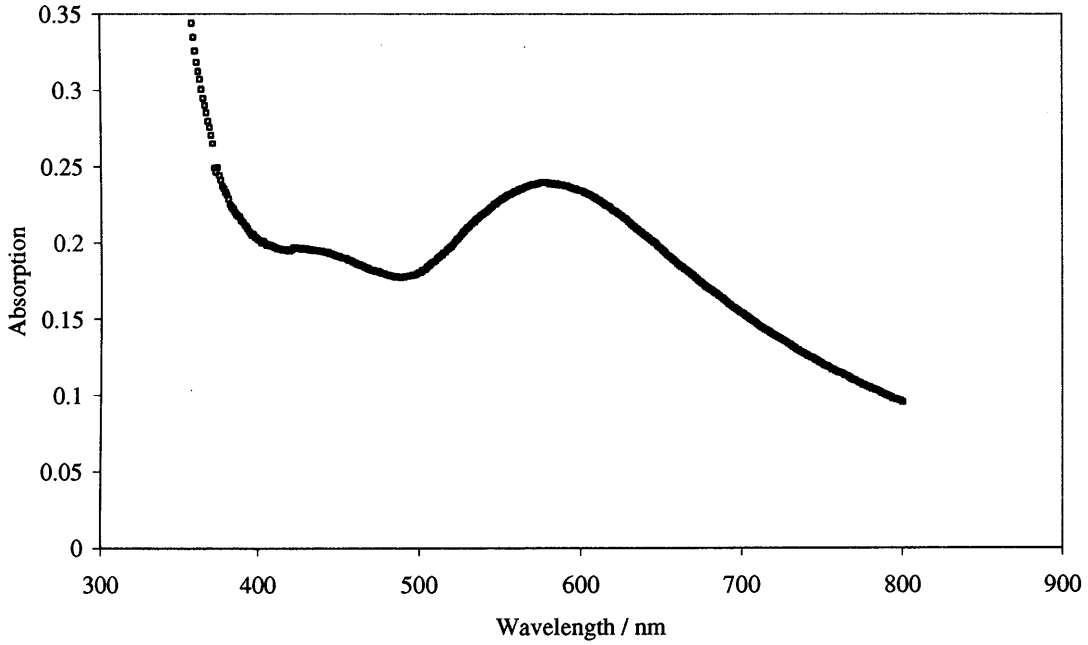

Figure 4.1. UV visible spectrum of a film deposited from $Ti(O^iPr)_4$ and pre formed gold nanoparticles. The high absorption below λ = 350 nm is caused by the substrate.

Powder XRD conducted at a glancing angle confirmed the presence of crystalline gold in the film. A typical diffraction pattern is shown in figure 4.2. Diffraction peaks can be seen corresponding to cubic Au [111] and [200] at 2θ values of 38.7° and 44.9° respectively ($\lambda = 1.540 \times 10^{-10}$ m).[133] These are the only cubic gold peaks expected to appear in the angle range that the diffraction patterns were taken. The unit cell constant for fcc Au lattice was calculated from these peaks to be a = 4.07 Å. Peaks at 54.6° and 57.6° correspond to the [211] and [105] peaks of anatase TiO_2,[193] although other peaks

expected for anatase titania at lower 2θ values are absent. The very broad peak centred on 2θ = 27° arises from the amorphous substrate.

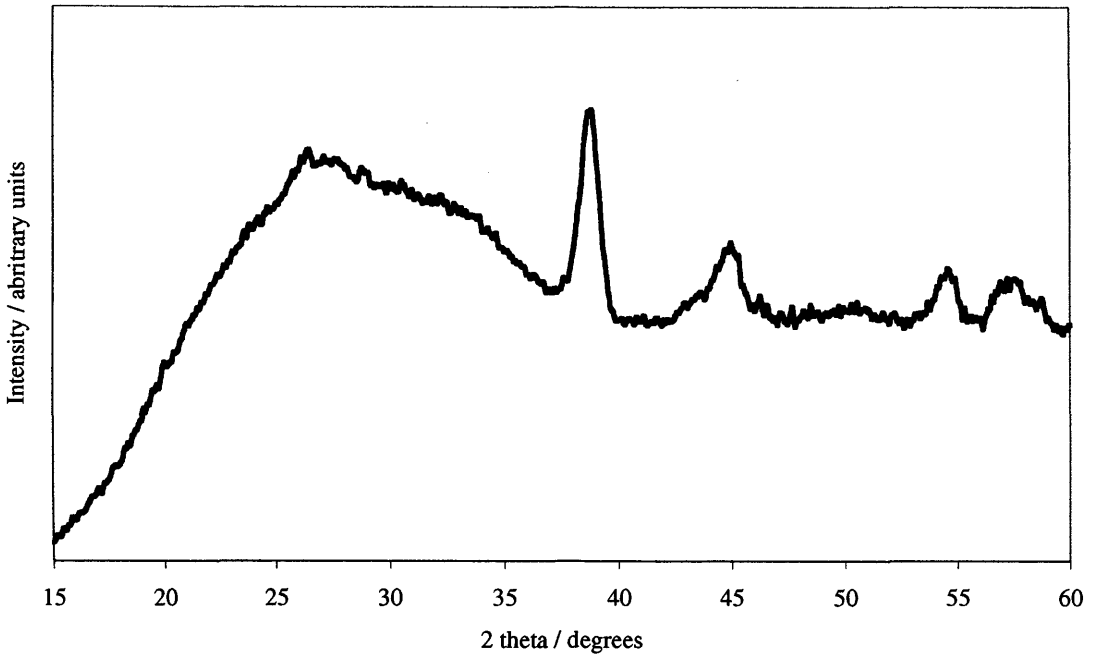

Figure 4.2. XRD pattern obtained from a gold film deposited on glass from gold colloid and Ti(O^{i}Pr)$_4$. The peaks at 38.7° and 44.9° are assigned to the [111] and [200] planes of cubic Au as indicated. Peaks at 54.6° and 57.6° correspond to the [211] and [105] planes of anatase TiO_2.

XPS was performed, confirming the presence of gold and titanium in the film; a single gold environment was observed with Au $4f_{7/2}$ and $4f_{5/2}$ peaks at binding energies of 83.4 eV and 87.2 eV respectively, corresponding to Au metal.[194, 195] The low intensity of the gold peaks prevented meaningful peak fitting, so it is unclear whether there are multiple gold environments present. Ti $2p_{1/2}$ and $2p_{3/2}$ binding energies were observed at 458.8 eV and 464.9 eV, as shown in figure 4.3. Each peak was successfully fitted with a unimodal Gaussian-Lorentzian fit, showing that only a single environment of Ti was present. The binding energies of these peaks corresponds to Ti^{4+} in TiO_2.[196] Quantification using peak areas determined by the Shirley method and empirical sensitivity factors gave a gold to titania atomic ratio of around 1:100 at the surface.[160] Nitrogen was also detected, with N 1s peaks appearing at binding energies of 407.3 eV and 399.8 eV. Since a singlet is expected for N1s photoelectrons, the two peaks correspond to different nitrogen environments. The peak at 399.8 eV is typical of nitrogen in amines,[169] suggesting the presence of TOAB on the film surface. The peak

at 407.3 eV corresponds to oxides of nitrogen,[197] which could be the result of TOAB combustion.

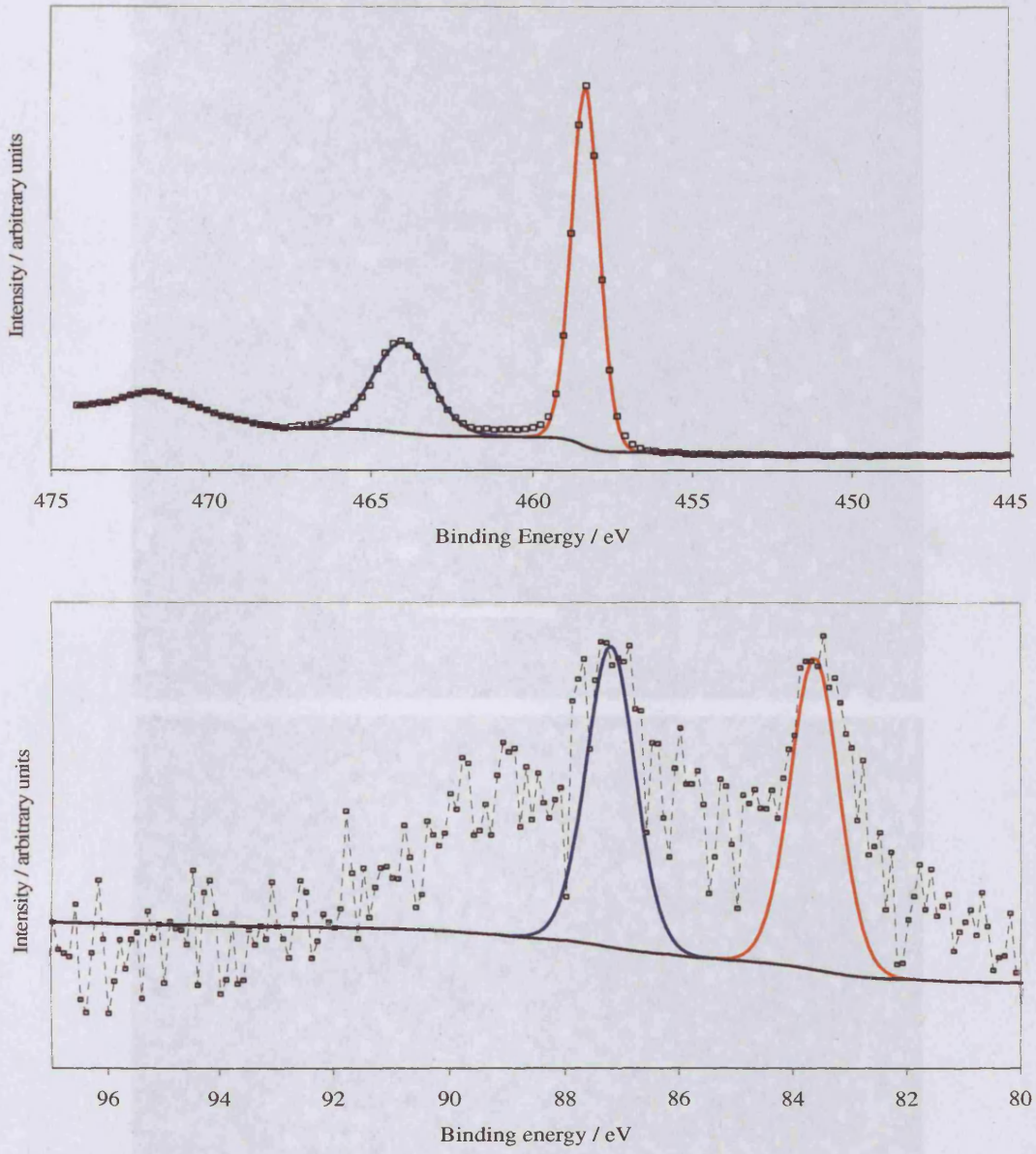

Figure 4.3. XPS spectra taken from a TiO_2 / Au composite film. *Top*: Ti region. *Bottom*: Au region. Experimental data is shown by points. Red and blue lines are unimodal Gaussian-Lorentzian fits. The black line is the background, calculated using the Shirley method.

SEM imaging conducted in secondary electron mode revealed a somewhat particulate structure to the composite film (figure 4.4, top). The underlying film appears to consist of small closely packed grains, around 5 nm in size. Larger, 100 nm particles appeared randomly positioned on the surface. The particles are not present in a film deposited from $Ti(O^iPr)_4$ alone (figure 4.4, bottom).

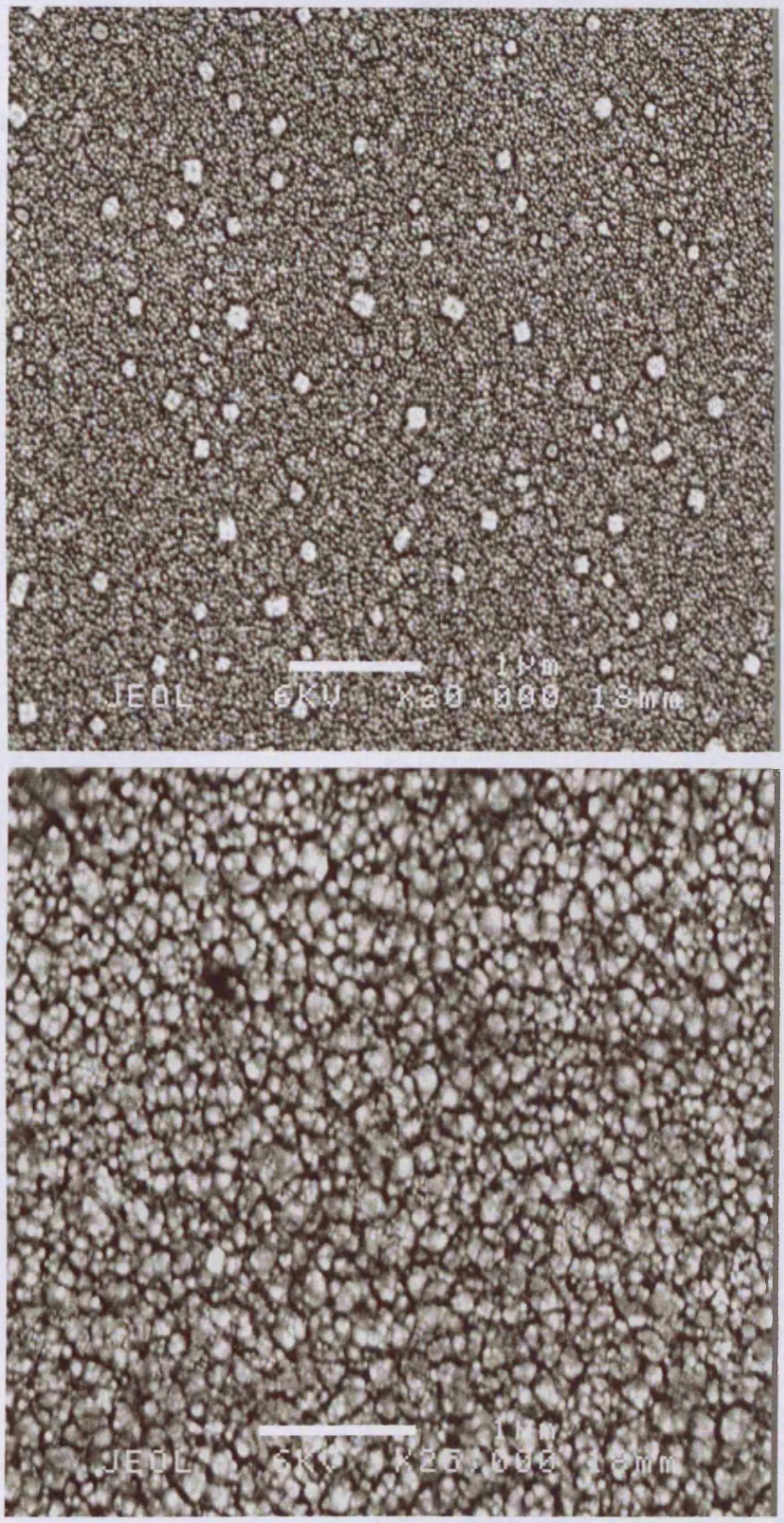

Figure 4.4. Secondary electron SEM images of a film deposited from *top*: $Ti(O^iPr)_4$ and preformed gold nanoparticles and *bottom*: $Ti(O^iPr)_4$ alone. Scale bars measure 1 μm

Effect of Annealing

It has been reported that heat treatment causes changes in the optical properties of gold composite films.[133, 140, 198] Therefore, the effect of annealing the titania / gold composite film at 550°C in air was investigated.

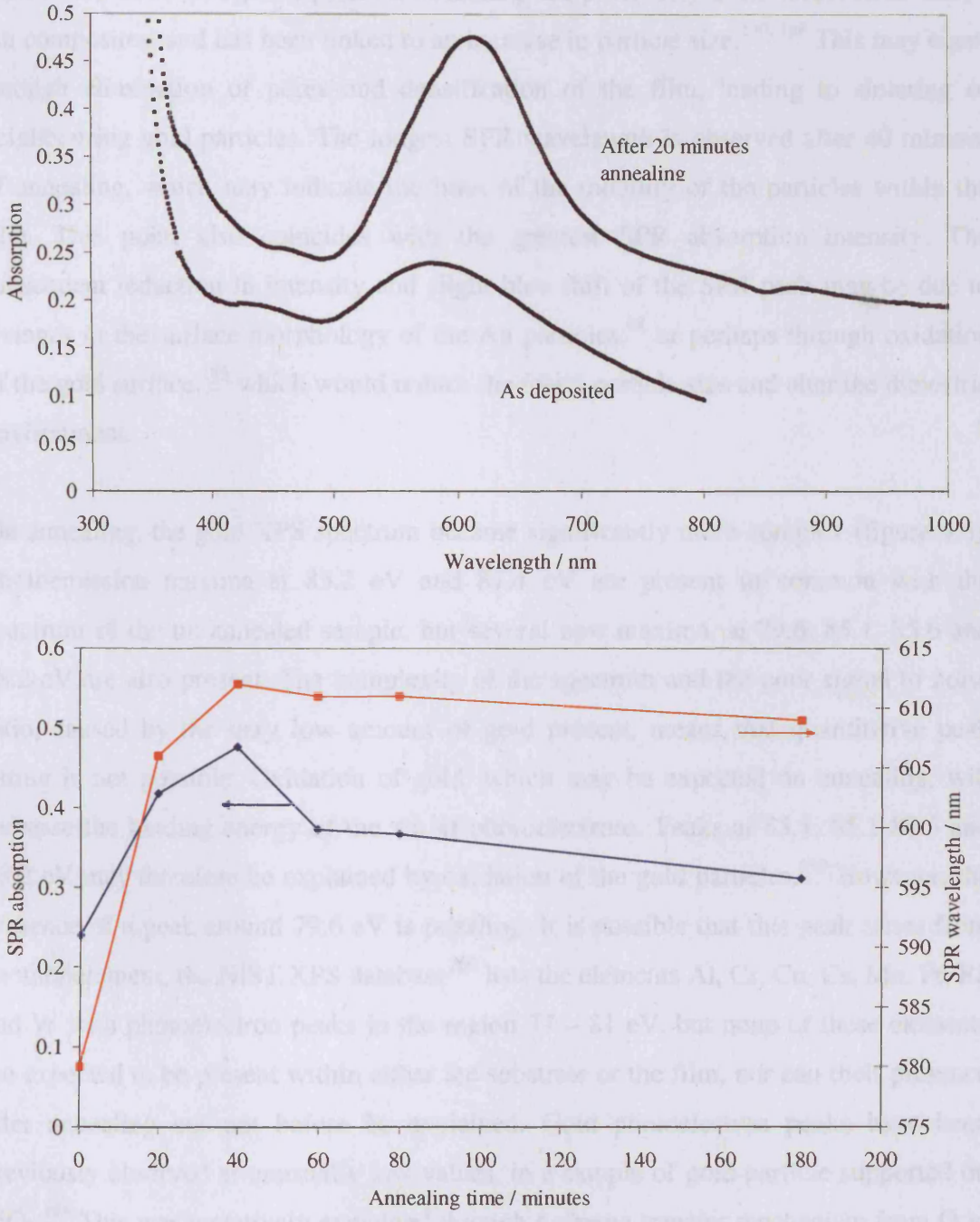

Figure 4.5. Effect of annealing at 550°C in air on a TiO_2 / Au composite film. *Top:* UV / visible absorption spectra taken at 0 and 40 minutes of annealing. *Bottom:* change in SPR absorption and wavelength with annealing.

The first 20 minutes of annealing resulted in a red shift in the SPR absorption peak maximum from 580 to 605 nm, accompanied by an increase in absorption peak intensity. After 40 minutes of annealing, a further red-shift and increase in absorption intensity occurred. At longer annealing times, the SPR peak showed a slight blue-shift and a decrease in absorption intensity. These changes are shown in figure 4.5. A red shift of the SPR absorption peak on annealing has previously been observed in TiO_2 / Au composites, and has been linked to an increase in particle size.[140, 198] This may occur through elimination of pores and densification of the film, leading to sintering of neighbouring gold particles. The longest SPR wavelength is observed after 40 minutes of annealing, which may indicate the limit of the mobility of the particles within the film. This point also coincides with the greatest SPR absorption intensity. The subsequent reduction in intensity and slight blue shift of the SPR peak may be due to changes in the surface morphology of the Au particles,[68] or perhaps through oxidation of the gold surface,[195] which would reduce the metal particle size and alter the dielectric environment.

On annealing, the gold XPS spectrum became significantly more complex (figure 4.6). Photoemission maxima at 83.2 eV and 87.4 eV are present in common with the spectrum of the un-annealed sample, but several new maxima, at 79.6, 85.1, 85.6 and 88.2 eV are also present. The complexity of the spectrum and the poor signal to noise ratio, caused by the very low amount of gold present, means that quantitative peak fitting is not possible. Oxidation of gold, which may be expected on annealing, will increase the binding energy of the Au 4f photoelectrons. Peaks at 85.1, 85.1 87.5 and 88.2 eV may therefore be explained by oxidation of the gold particles.[199] However, the presence of a peak around 79.6 eV is puzzling. It is possible that this peak arises from another element; the NIST XPS database[200] lists the elements Al, Cr, Cu, Cs, Mn, Pt, Rh and W with photoelectron peaks in the region 77 – 81 eV, but none of these elements are expected to be present within either the substrate or the film, nor can their presence after annealing but not before be explained. Gold photoelectron peaks have been previously observed at unusually low values, in a sample of gold particle supported on TiO_2.[195] This was tentatively explained through a charge transfer mechanism from O to Au, resulting in $Au^{\delta-}$. This may be the reason for the appearance of the peak at 79.6 eV after annealing, and may indicate better contact between the titania and the gold phase than in the un-annealed sample, allowing this charge transfer to take place.

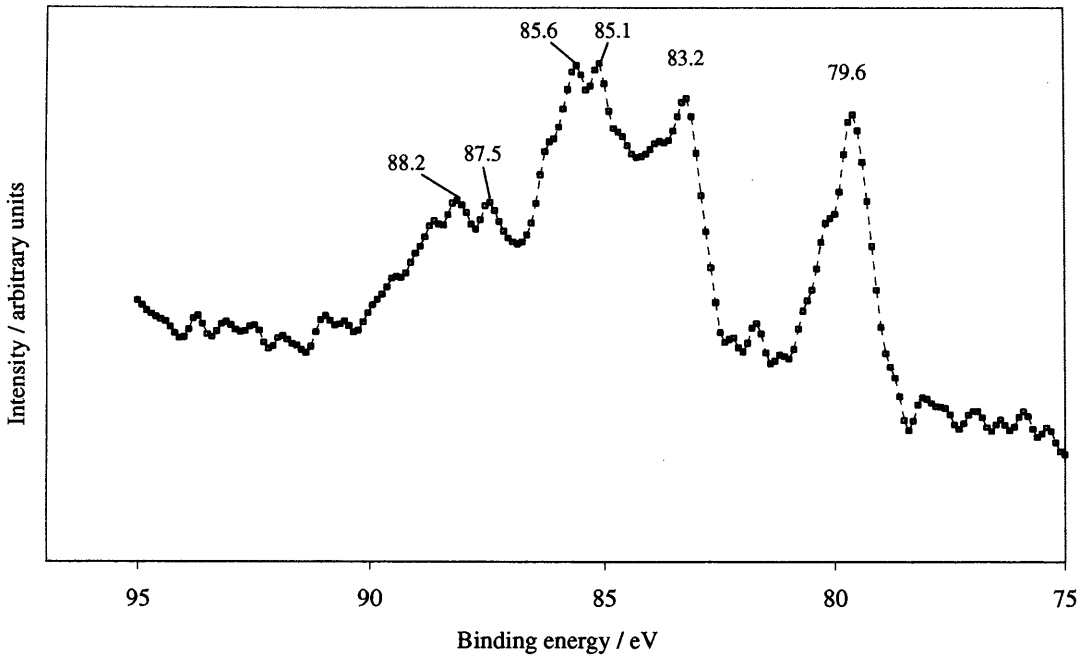

Figure 4.6. XPS spectrum, Au 4f region, of a titania / gold composite film after annealing.

Photoelectron peaks in the N 1s region also changed upon annealing. The peak at 407.3 eV was no longer present, possibly indicating removal of the oxides of nitrogen from the film surface. A peak at 400.0 eV remained, thought to correspond to TOAB, showing that at least some surfactant survives the annealing process.

Annealing also caused changes in the XRD pattern of the titania / gold composite film. After annealing, diffraction peaks corresponding to anatase TiO_2 emerged (Figure 4.7). No peaks corresponding to rutile phase TiO_2, expected principally at 2θ values of 28°, 36° and 42° were seen.[163] The FWHM of the gold diffraction peaks decreased slightly, indicating an increase in crystallite size.

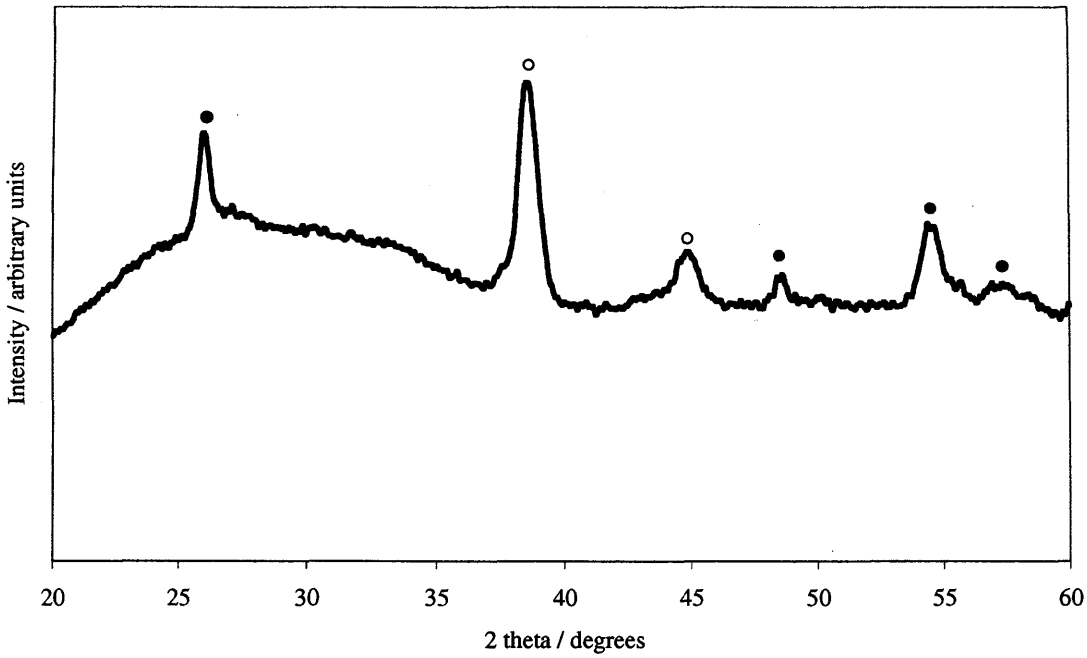

Figure 4.7. Powder XRD pattern of a titania / gold composite film after 180 minutes of annealing at 550°C in air. Black circles indicate peaks assigned to anatase TiO_2. White circles indicate cubic Au diffraction peaks, which are largely unchanged by annealing.

4.3.2 Gold Colloid + $W(OPh)_6$

Depositions were carried out using a precursor solution of $W(OPh)_6$ (1.0 g, 1.5 mmol) and stock pre-formed gold nanoparticle solution (5 mL), the synthesis of which is described in Chapter 3, in toluene (20 mL). A substrate temperature of 450°C and a flow rate of 1.0 L min^{-1} were used. The resulting film was very dark blue in colour. The front 50 mm of the substrate was covered. The strong blue colour is characteristic of partially reduced tungsten (VI) oxide, commonly written as WO_{3-x}. The strong colouration masked the SPR absorption peak, if present, so the position could not be determined. However, as shown in figure 4.8, XRD indicated the presence of cubic Au within the film. Au [111] and [200] diffraction peaks appeared at 2θ values of 38.8° and 45.1° respectively ($\lambda = 1.540 \times 10^{-10}$ m).[133] The unit cell constant for fcc Au lattice was calculated from these peaks to be a = 4.07 Å, in common with all other gold films reported thus far. Tungsten oxide peaks appear at 28.9° and 48.5°, and are assigned to [020] and [040] diffraction peaks of monoclinic WO_3 respectively.[44] The presence of only two WO_3 peaks shows strong preferred orientation in the [020] direction, as

previously well documented in a variety of WO_3 films.[44, 201, 202] Calculation of lattice constants of the tungsten oxide phase was not possible using these data.

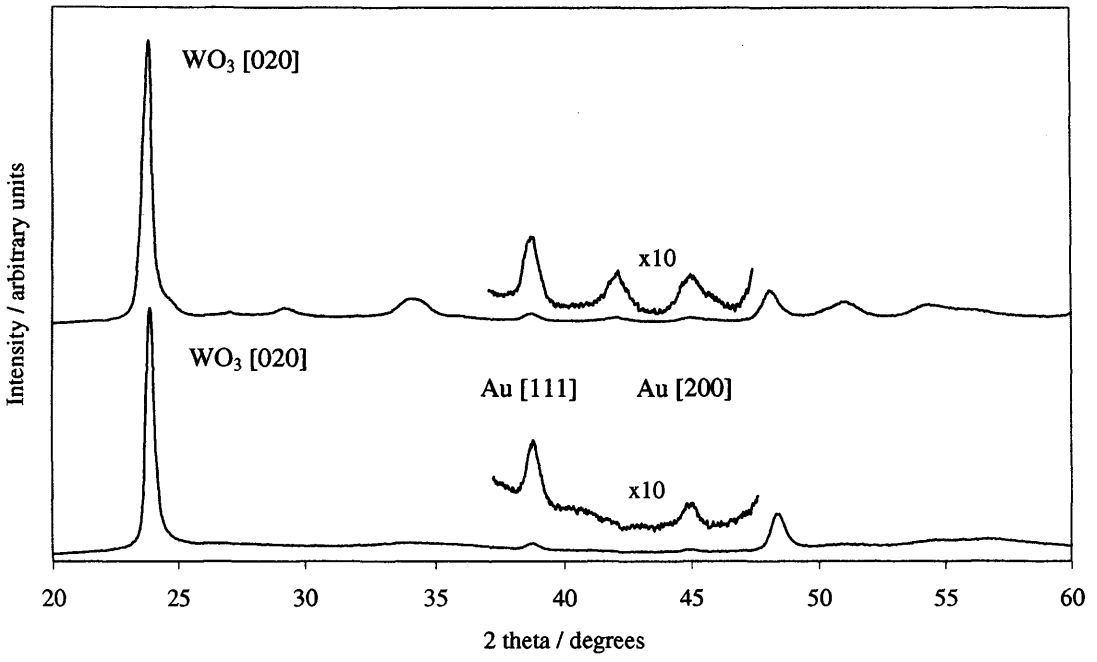

Figure 4.8 XRD pattern of WO_3 : Au composite film. *Bottom:* As deposited, *Top:* after annealing at 550°C. Magnified sections show the Au [111] and [200] diffraction peaks.

SEM imaging conducted in secondary electron mode showed an underlying fibre like morphology with roughly spherical particles around 100 nm in diameter. Figure 4.9 shows a typical SEM image of this WO_3 : Au film. A wide variety of WO_3 morphologies have been reported in films deposited by CVD, including a fiberous mesh as seen in this case.[203]

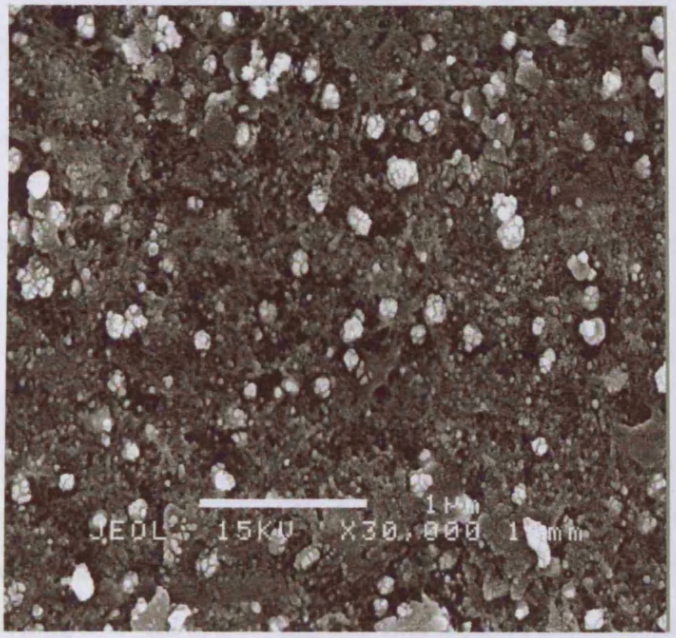

Figure 4.9. SEM (secondary electron) image of a WO_3 : Au composite film. Scale bar measures 1 μm.

The film was annealed at 550°C for 1 hour, in an attempt to oxidise the film to stoichiometric WO_3. Fully oxidised WO_3 is pale yellow in colour, and it was thought that the SPR peak maximum would be discernable. This was not the case, and the absorption remained very high throughout the visible region, masking any SPR absorption that may have been present. The XRD of the annealed film is shown in figure 4.8. The emergence of low intensity diffraction peaks at 24.8°, 34.2°, 42.1°, 51.2° and 54.5° is thought to be due to slight randomization of the crystallite orientation, although the very low intensity of these peaks compared with the [020] and [040] peaks shows that strong preferred orientation remains

XPS of WO_3 : Au composite confirmed the presence of tungsten and gold, showing Au 4f peaks at binding energies of 84.3 eV and 88.0 eV, within the range expected for Au metal. After annealing, W 4f peaks were observed at 35.9 eV and 38.1 eV, indicating WO_3. The ratio of gold to tungsten was calculated by measuring photoelectron peak areas using a Shirley background. The ratio of tungsten to gold was calculated as 7 : 1.

4.3.3 Discussion

Optical absorption

The SPR absorption peak of the TiO_2 : Au composite film appeared at 580 nm, red-shifted from that of the original starting solution. This is comparable to SPR peaks observed in thin films of TiO_2 : Au composite prepared through alternative means, which have been reported from 580 – 640 nm.[113, 198] The red shift is due to the higher refractive index of the titania host matrix compared with the toluene in the precursor solution. However, a Mie theory analysis shows that small non-interacting gold nanoparticles encased in titania should show a SPR peak at 650 nm.[113] The fact that a much shorter wavelength is observed suggests that contact between the titania and gold phases is not good, or that the refractive index of the titania is lower than expected. The latter hypothesis is supported by the XRD data, which shows an amorphous host matrix in the as deposited film. Annealing lead to a shift in the SPR peak towards that expected from Mie theory. This may be due to crystallisation of the host matrix, as confirmed by XRD, leading to a higher refractive index, and hence a greater red-shift. Annealing may also reduce the porosity of the film, and so create better contact between the gold and titania phases. These processes seem to reach a limit after 40 minutes of annealing at 550 °C, after which a slight blue shift occurs in the SPR absorption peak. It has been previously observed that gold particles in TiO_2 : Au composites increase in size on annealing,[198] therefore this may also be a contributing factor to the SPR red-shift.

4.4 Depositions using [$HAuCl_4$] + Metal Oxide Precursor

4.4.1 [$HAuCl_4$] + $W(CO)_6$

Depositions were carried out using $W(CO)_6$ (0.52 g, 1.5 mmol) and [$HAuCl_4$] (0.160, 0.080, 0.040 and 0.020 g) in acetone (80 mL). Initial investigations showed that the best coverage of the substrate using this combination of precursors occurred using relatively low substrate temperatures and high flow rates. A substrate temperature of 200°C and a flow rate of 3.5 L min^{-1} were used. In all cases the film covered the entire substrate, and the colour appeared uniform throughout. The colour changed from pink to purple in transmission with increasing gold content. Films were poorly adherent, and could be wiped from the substrate with a tissue.

UV / visible spectroscopy showed SPR absorption peaks in all films. In the film deposited from the lowest precursor concentration of gold, the SPR absorption maximum appeared at 550 nm. The SPR peak is red shifted and increases in intensity with increasing concentration of $[HAuCl_4]$, reaching 580 nm in the film with highest gold concentration (figure 4.10). This red shift is consistent with larger or more closely spaced gold particles, as discussed in Chapter 1.

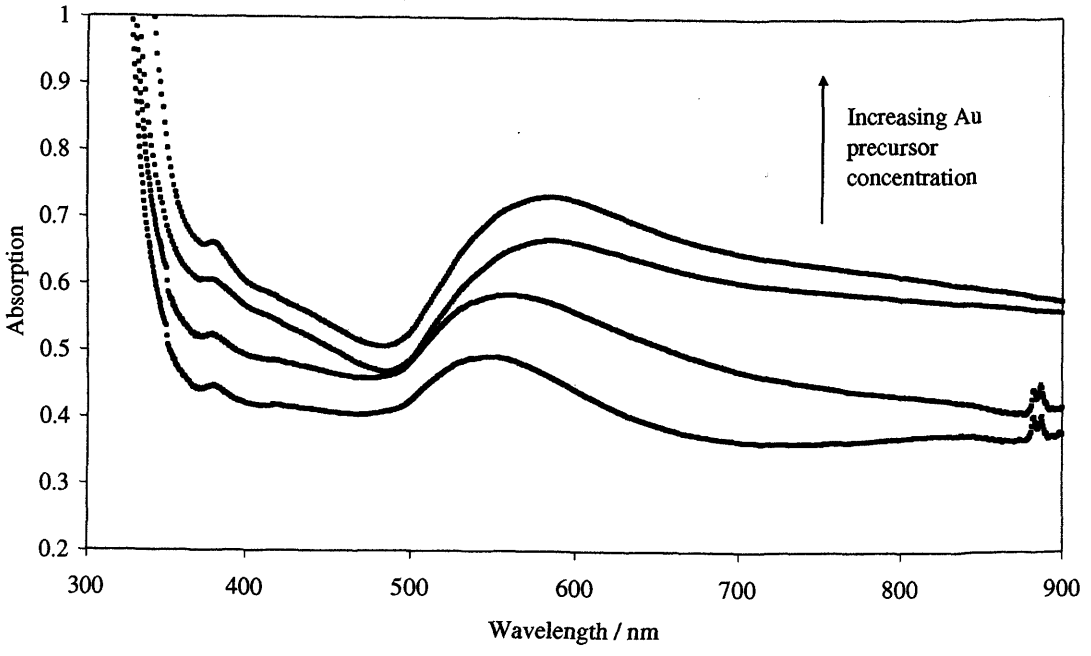

Figure 4.10. UV / visible absorption spectra of WO_3 : Au composite films with varying gold content. The feature at 890 nm in two of the spectra is an instrumental artefact.

XPS indicated the presence of W and Au within the films. Figure 4.11 shows the W4f photoelectron spectrum for a composite film deposited from a low concentration of gold. The W 4f spectrum was fitted with Gaussian-Lorentzian peaks using a background calculated using the Shirley method. W $4f_{7/2}$ and $4f_{5/2}$ peaks were fitted at 35.4 and 37.5 eV respectively. This is in agreement with published data from WO_3.[204] No additional peaks corresponding to W^{5+} or W^{4+} were observed.

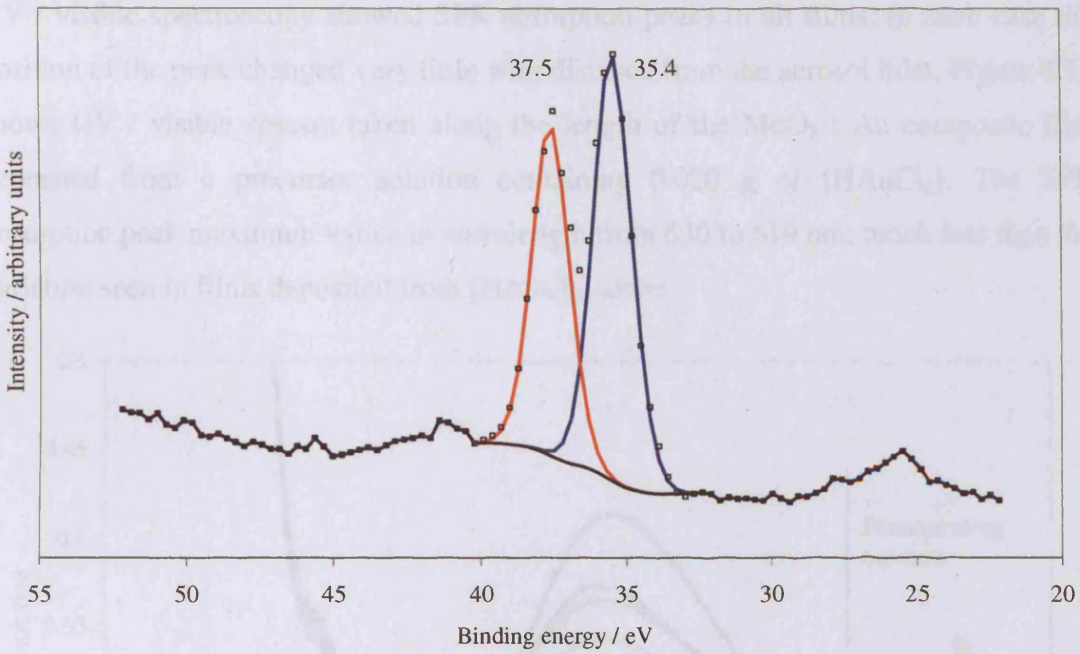

Figure 4.11. X-ray photoelectron spectrum of a WO_3 : Au composite, showing the W 4f region. Experimental data is shown by points. Red and blue lines are unimodal Gaussian-Lorentzian fits. The black line is the background, calculated using the Shirley method. Peaks at 35.4 and 37.5 eV correspond to W^{6+}.

The Au 4f photoelectron spectra was similarly fitted with Gaussian-Lorentzian peaks. Peaks assigned to Au $4f_{7/2}$ and $4f_{5/2}$ with binding energies of at 83.9 and 87.6 eV and FWHM of 1.41 and 1.42 eV respectively were observed. These binding energies and FWHM correspond closely to those observed for metallic gold.[199, 205]

4.4.2 $[HAuCl_4]$ + $Mo(CO)_6$

Depositions were carried out using $Mo(CO)_6$ (0.30 g, 1.1 mmol) and $[HAuCl_4]$ (0.080, 0.040, 0.020 and 0.010 g) in acetone (80 mL). As in the case of depositions using $W(CO)_6$, the best coverage of the substrate using this combination of precursors occurred using low substrate temperatures and high flow rates. A substrate temperature of 200°C and a flow rate of 3.5 L min^{-1} were used. In all cases the film covered the entire substrate. The colour of the films in transmission varied from red nearest the to brown. Films were more adherent than the films deposited from $W(CO)_6$, and were somewhat resistant to mechanical abrasion.

UV / visible spectroscopy showed SPR absorption peaks in all films. In each case the position of the peak changed very little with distance from the aerosol inlet. Figure 4.12 shows UV / visible spectra taken along the length of the MoO_3 : Au composite film deposited from a precursor solution containing 0.020 g of [$HAuCl_4$]. The SPR absorption peak maximum varies in wavelength from 630 to 619 nm: much less than the variation seen in films deposited from [$HAuCl_4$] alone.

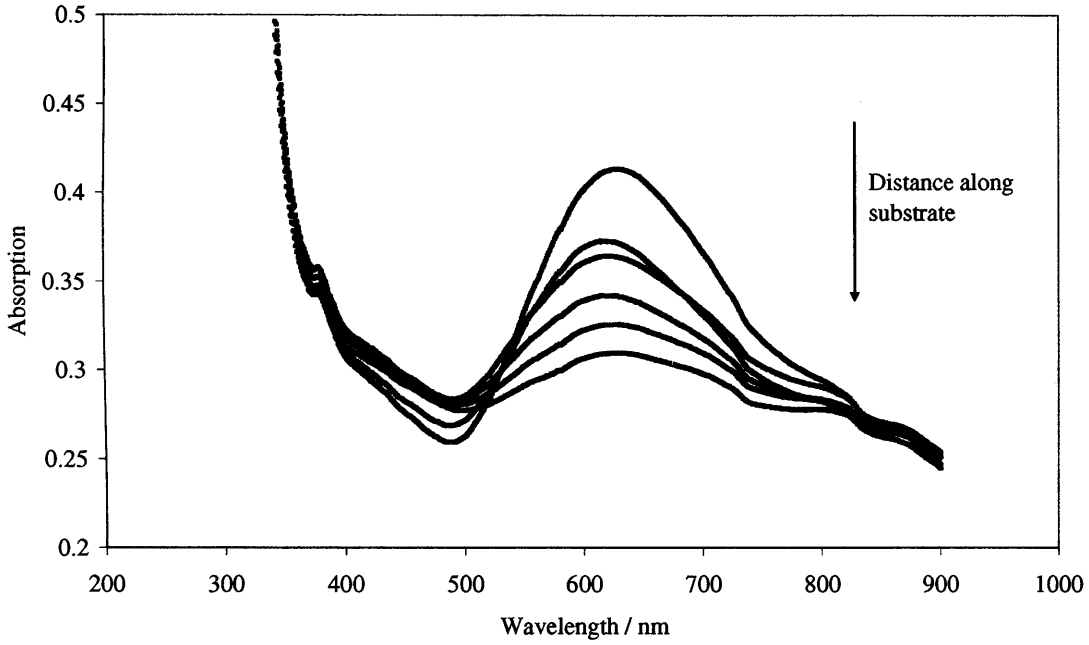

Figure 4.12. UV / visible absorption spectra of a MoO_3 / Au composite taken at regular intervals along the substrate.

XPS showed the presence of Mo and Au within all the composite films. The Mo 3d region was fitted with Gaussian-Lorentzian peaks using a background calculated using the Shirley method. Mo $3d_{5/2}$ and $3d_{3/2}$ peaks were fitted at 232.7 and 235.7 eV respectively (figure 4.13). This is in agreement with published data from MoO_3.[204] In each film, a single gold environment with Au $4f_{7/2}$ and $4f_{5/2}$ peaks from 83.9 – 84.0 and 87.6 – 87.8 eV respectively was observed. These correspond closely to metallic gold,[199, 205] and show that no Au^{3+} ions remain, and that no oxidation of the nanoparticles has occurred.

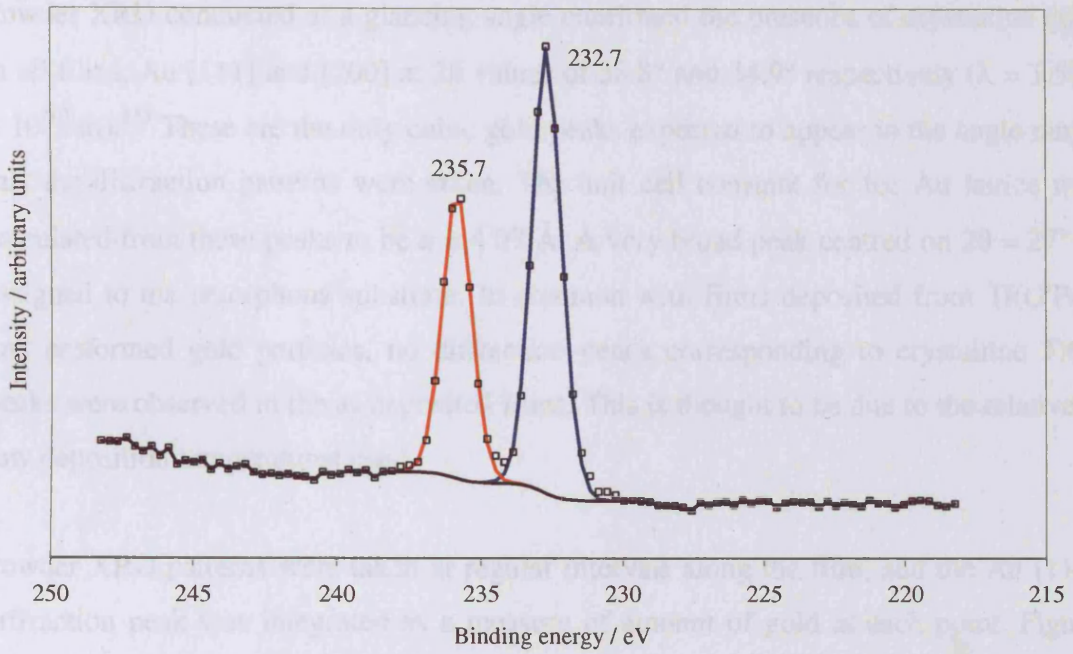

Figure 4.13. X-ray photoelectron spectrum of a MoO_3 : Au composite, showing the Mo 3d region. Experimental data is shown by points. Red and blue lines are unimodal Gaussian-Lorentzian fits. The black line is the background, calculated using the Shirley method. Peaks at 232.7 and 235.7 eV correspond to Mo^{6+}.

4.4.3 $[HAuCl_4]$ + TOAB + $Ti(OiPr)_4$

Depositions were carried out using a precursor solution containing $Ti(O^iPr)_4$, TOAB and $[HAuCl_4]$. Precursor solutions were prepared by first dissolving $[HAuCl_4]$ (0.080 g, 0.020 g, 0.010 g) in distilled water (20 mL) and TOAB (1.00 g) in toluene (40 mL). The two solutions were mixed vigorously in a glass beaker to affect the phase transfer of Au^{3+} to the organic phase. After 5 minutes of stirring, the aqueous phase was separated and discarded. The organic phase was made up to 40 mL with toluene, then dried over anhydrous Na_2SO_3. $Ti(O^iPr)_4$ (0.56 g, 2.0 mmol) was added. The solution remained transparent, indicating that hydrolysis of $Ti(O^iPr)_4$ and formation of TiO_2 did not occur.

Depositions were carried out using the precursor solution prepared as described, a substrate temperature of 400°C and a flow rate of 2.0 L min^{-1}. In all cases films consisted of a strip of deposition 30 - 80 mm from the aerosol inlet. Films were adherent and unaffected by routine handling or rubbing with a tissue. Films were pale blue in colour, the colour becoming more intense in films deposited from a higher concentration of $[HAuCl_4]$.

Powder XRD conducted at a glancing angle confirmed the presence of crystalline gold in all films. Au [111] and [200] at 2θ values of 38.8° and 44.9° respectively (λ = 1.540 × 10^{-10} m).[133] These are the only cubic gold peaks expected to appear in the angle range that the diffraction patterns were taken. The unit cell constant for fcc Au lattice was calculated from these peaks to be a = 4.07 Å. A very broad peak centred on 2θ = 27° is assigned to the amorphous substrate. In common with films deposited from $Ti(O^iPr)_4$ and preformed gold particles, no diffraction peaks corresponding to crystalline TiO_2 peaks were observed in the as deposited films. This is thought to be due to the relatively low deposition temperatures used.

Powder XRD patterns were taken at regular intervals along the film, and the Au [111] diffraction peak was integrated as a measure of amount of gold at each point. Figure 4.14 shows the results of this analysis for films deposited from different amounts of $[HAuCl_4]$.

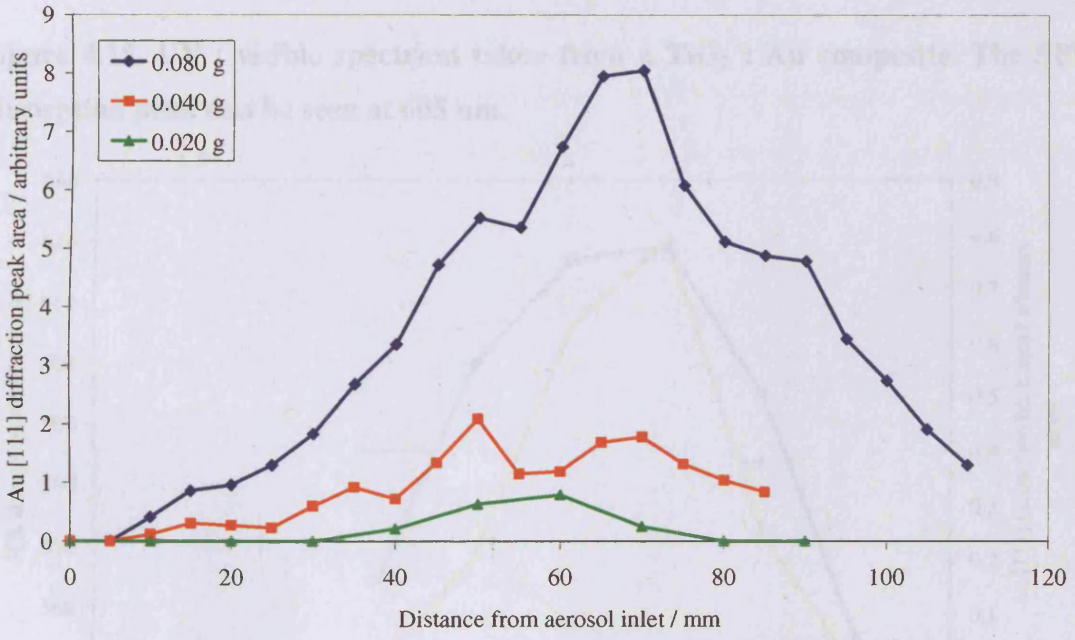

Figure 4.14. Variation in Au [111] diffraction peak area along the length of TiO_2 : Au composite films deposited from various amounts of $[HAuCl_4]$, as indicated inset.

The deposition profiles obtained from the XRD data show that in each case the deposition maximum occurs between 50 and 65 mm from the aerosol inlet. As expected, a greater precursor concentration of gold leads to a greater amount of gold within the composite film.

UV / visible absorption spectroscopy showed SPR absorption peaks in each film, indicating the presence of nanoscale gold. Figure 4.15 shows a typical spectrum, taken from the film deposited from 0.040 g [$HAuCl_4$]. A single SPR absorption peak can be seen at 605 nm.

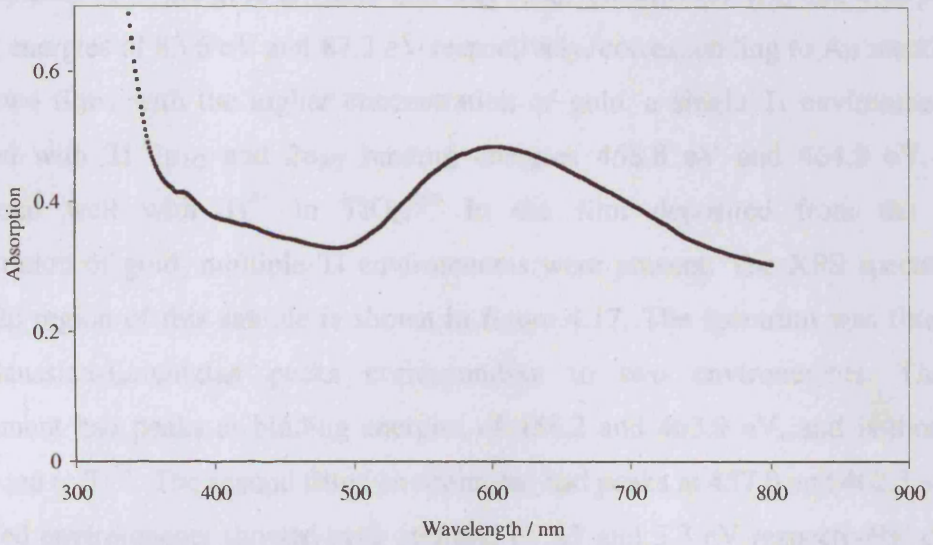

Figure 4.15. UV / visible spectrum taken from a TiO_2 : Au composite. The SPR absorption peak can be seen at 605 nm.

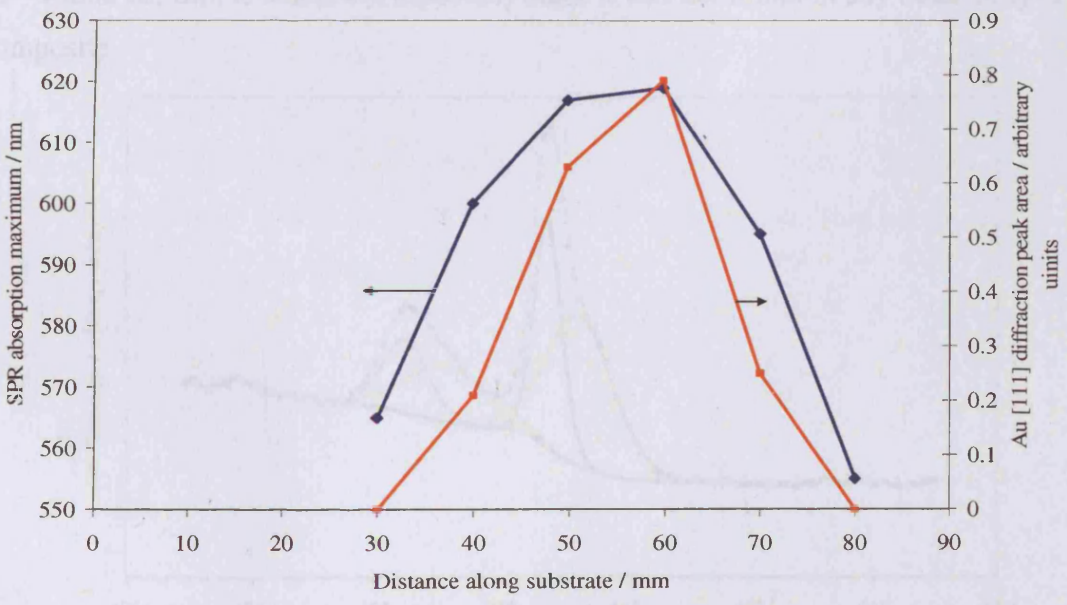

Figure 4.16. Variation in SPR absorption peak maximum and Au [111] diffraction peak area along the length of a TiO_2 : Au composite film deposited from the lowest precursor concentration of Au.

Figure 4.16 shows a comparison between the SPR absorption wavelength and the Au [111] diffraction peak area along the length of a TiO_2 : Au composite film. It can be

seen that the SPR and XRD profiles are similar in shape, and that the maximum SPR wavelength coincides with the Au [111] peak area maximum.

XPS was performed on each sample, confirming the presence of gold and titanium in the composite. A single gold environment was observed with Au $4f_{7/2}$ and $4f_{5/2}$ peaks at binding energies of 83.6 eV and 87.3 eV respectively, corresponding to Au metal.[194, 195] In the two films with the higher concentration of gold, a single Ti environment was observed with Ti $2p_{1/2}$ and $2p_{3/2}$ binding energies 458.8 eV and 464.9 eV. These correspond well with Ti^{4+} in TiO_2.[196] In the film deposited from the lowest concentration of gold, multiple Ti environments were present. The XPS spectrum for the Ti 2p region of this sample is shown in figure 4.17. The spectrum was fitted with four Gaussian-Lorentzian peaks corresponding to two environments. The first environment had peaks at binding energies of 458.2 and 463.9 eV, and is thought to correspond to Ti^{4+}. The second fitted environment had peaks at 457.0 and 462.3 eV. The two fitted environments showed peak splitting of 5.7 and 5.3 eV respectively, close to that expected for Ti $2p_{1/2}$ and $2p_{3/2}$ peaks. It is thought this second environment, appearing at a lower binding energy, corresponds to Ti^{3+}. The reason for the presence of Ti^{3+} within the film is unknown, especially since it was not found in any other TiO_2 : Au composite.

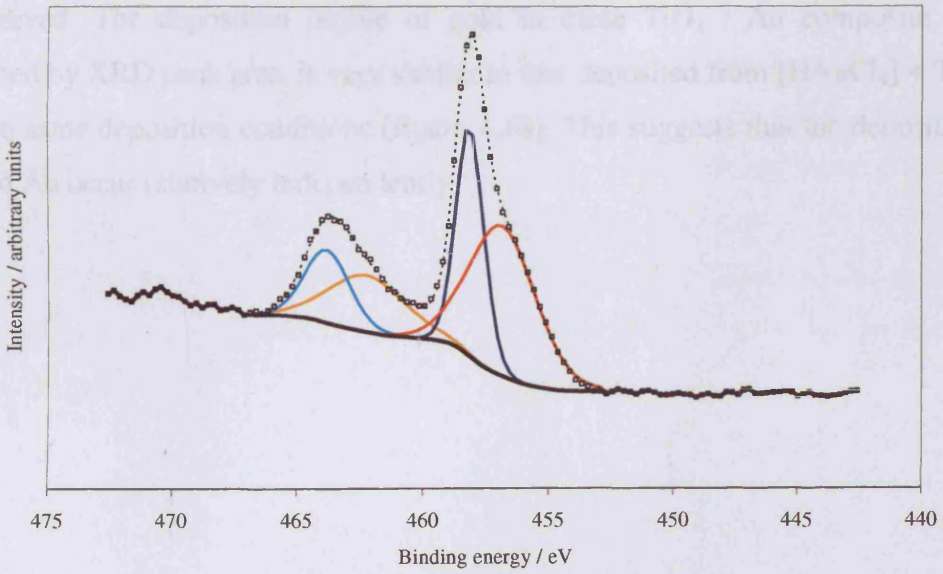

Figure 4.17. Photoelectron spectrum of Ti 2p region of a TiO_2 : Au composite film. Experimental data is shown by points. Red, orange, blue and light blue lines are unimodal Gaussian-Lorentzian fits corresponding to two Ti environments. The dashed line is the sum of the fitted peaks. The black line is the background, calculated using the Shirley method.

4.4.4 Discussion

Deposition mechanism

Both the metal carbonyl precursors investigated, $W(CO)_6$ and $Mo(CO)_6$ have been previously used as CVD precursors, to deposit tungsten oxide and molybdenum oxide films respectively.[187, 188, 206, 207] Both precursors react at relatively low temperatures; preliminary work showed that deposition temperatures of 250 - 400°C can be used to give good substrate coverage. In contrast, $[HAuCl_4]$ alone gives no appreciable coating below 350°C. It is interesting to note, therefore, that gold is easily incorporated into the tungsten oxide and molybdenum oxide films at temperatures as low as 200°C. Indeed, even at this low substrate temperature a relatively fast flow rate had to be employed (3.5 L min^{-1} compared to 1.0 – 2.0 L min^{-1} for the other precursors used in this work) so that the film was not highly localised at the front of the substrate. This may be due to the different solvent used; acetone was used to deposit composite films due to the better solubility of the carbonyl precursor, while methanol was used to deposit films of gold alone.

In the case of the films deposited from $Ti(OiPr)_4$ + TOAB + $[HAuCl_4]$ a similar effect is not observed. The deposition profile of gold in these TiO_2 : Au composite films, determined by XRD peak area, is very similar to that deposited from $[HAuCl_4]$ + TOAB using the same deposition conditions (figure 4.18). This suggests that the deposition of TiO_2 and Au occur relatively independently.

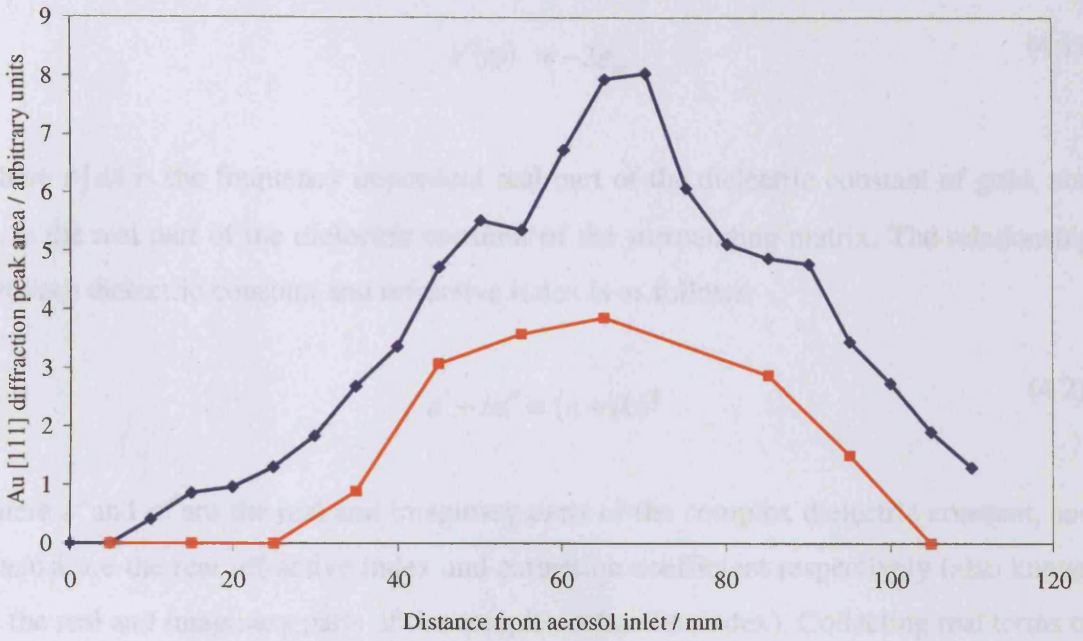

Figure 4.18. Variation in Au [111] diffraction peak area along the length of TiO_2 : Au composite film (blue) and a gold film (red) deposited using identical substrate temperatures, flow rates and gold precursor concentrations.

The enhancement in deposition of both precursors when [$HAuCl_4$] and $M(CO)_6$ (M = W, Mo) are deposited together may indicate a reaction occurs between the two precursors, although this may also be an effect of using a different solvent. Tungsten carbonyl and molybdenum carbonyl undergo reaction with Cl_2 to give dinuclear metal halide carbonyl complexes.[190] Cl_2 is expected to be present in the reactor due to decomposition of [$HAuCl_4$], so this reaction may occur. Gold carbonyl chloride (ClAuCO) is also known, and could form from the free CO present from the metal carbonyl decomposition.[208] However, gold carbonyl chloride does not decompose at lower temperature than [$HAuCl_4$], so this reaction would probably not increase the deposition rate.

Optical absorption

The optical properties of all the composite films discussed in this chapter are dominated by SPR absorption. The wavelength of the SPR absorption peak of gold particles is dependent on the refractive index of the surrounding medium. In Chapter 1, the Mie theory was discussed as a theoretical approach to SPR absorption. For small, non-interacting gold particles, the resonance condition is given by the following equation:

$$\varepsilon'(\omega) = -2\varepsilon_m \tag{4.1}$$

where $\varepsilon'(\omega)$ is the frequency dependent real part of the dielectric constant of gold, and ε_m is the real part of the dielectric constant of the surrounding matrix. The relationship between dielectric constant and refractive index is as follows:

$$\varepsilon' + i\varepsilon'' \equiv (n + ik)^2 \tag{4.2}$$

where ε' and ε'' are the real and imaginary parts of the complex dielectric constant, and n and k are the real refractive index and extinction coefficient respectively (also known as the real and imaginary parts of the complex refractive index). Collecting real terms of equation 4.2 gives:

$$\varepsilon' \equiv n^2 + k^2 \tag{4.3}$$

For semiconductors at photon energies below the band gap energy, it can be assumed that k = 0.[209] Therefore:

$$\varepsilon' \equiv \varepsilon_m \equiv n^2 \tag{4.4}$$

and the Mie resonance condition becomes:

$$\varepsilon'(\omega) = -2n^2 \tag{4.5}$$

The resonance condition was calculated for matrices of different refractive index using bulk (size independent) values of $\varepsilon'(\omega)$. Bulk optical constants for gold were values were obtained from literature measurements on polycrystalline gold films.[210] Figure 4.19 shows these calculated Mie values of the SPR wavelength for matrices of different refractive index, and the experimental values for the composite films reported in this chapter. The experimental SPR peak positions are plotted as points using the refractive index of the matrix material, which were taken from literature measurements on bulk anatase-TiO_2, MoO_3 and WO_3 to be 2.4, 2.2 and 1.8 respectively.[211-213]

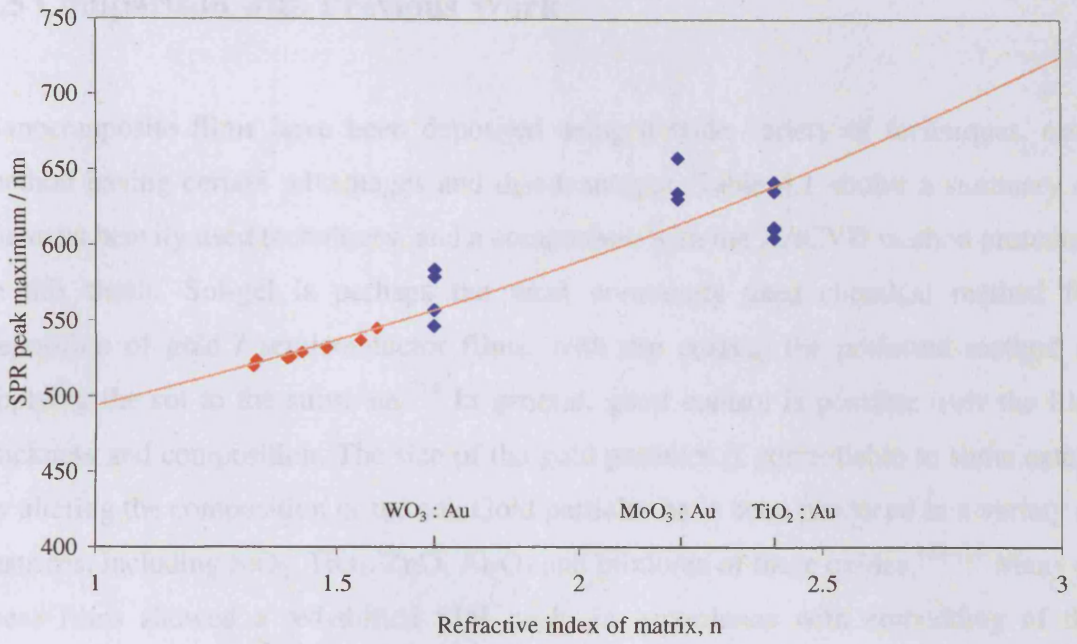

Figure 4.19. Variation in SPR with refractive index of the surrounding matrix. The red line shows values calculated using Mie theory, assuming small, non-interacting gold particles. The red points are literature experimental values for small gold particles dissolved in a variety of solvents.[60] Blue points refer to experimental values of composite films deposited in this work, plotted at the refractive index of the appropriate bulk semiconductor.

Figure 4.19 shows that the SPR values obtained for the composite films produced in this work are similar to those expected from Mie theory. In the case of WO_3 : Au and MoO_3 : Au films, some or all of the recorded SPR wavelengths were longer than expected. This red-shift could be due to interaction between particles or a large particle size, since Mie theory assumes small, non-interacting particles. In the case of TiO_2 : Au films, some showed SPR wavelengths shorter than expected. As already discussed, this may be due to low crystallinity of the titania matrix, or poor contact between the semiconductor and metal phase.

4.5 Comparison with Previous Work

Nanocomposite films have been deposited using a wide variety of techniques, each method having certain advantages and disadvantages. Table 4.1 shows a summary of the most heavily used techniques, and a comparison with the AACVD method presented in this thesis. Sol-gel is perhaps the most commonly used chemical method for deposition of gold / semiconductor films, with dip coating the preferred method of applying the sol to the substrate.[214] In general, good control is possible over the film thickness and composition. The size of the gold particles is controllable to some extent by altering the composition of the sol. Gold particles have been produced in a variety of matrices, including SiO_2, TiO_2, ZnO, Al_2O_3 and mixtures of these oxides.[135-139] Many of these films showed a red-shifted SPR peak, in accordance with embedding of the particles into a high refractive index matrix.[214] Sol gel routes are available to many other transition metal oxides, and it is expected that these too could be impregnated with gold particles by use of an appropriate gold precursor.

Spin coating of gold particles or precursors onto a pre-formed porous semiconductor oxide, followed by annealing has also been used to form nanocomposites.[130, 131] A porous semiconductor film can be produced by any suitable method, and as such a wide variety of semiconductor films can be used in this method.

Sputtering is a PVD technique in which gold and semiconductor targets are sputtered using an ion beam. The resulting material is deposited onto a substrate. The deposition is carried out under high vacuum, and the conditions must be carefully controlled to deposit the desired film.[141, 142]

Layer by layer deposition involves the deposition of preformed particles which are adhered to the substrate by chemical means, usually using a polymer. Deposition of core shell gold / semiconductor particles leads to composite films with highly tunable inter particle separation. [76, 192] This method offers excellent control over the film optical properties and composition. It is limited in that the core-shell particles must be synthesised before deposition, and the deposition can be slow, depending on how many layers are required. Also, the substrate size is limited by the dip coating apparatus used to apply each layer.

Method, references	Size of substrate	Range of Au loading possible	Preparation time	Range of matrix materials	Operating Pressure
AACVD	Large, possibly unlimited using online deposition	Wide range possible	10 – 30 minutes	CVD precursors available for many metal oxides, nitrides and sulfides	Atmospheric
Sol-gel, [132-139]	Limited by dip coating mechanism	Limited by gel formation	Several hours	Many oxide precursors available	Atmospheric
Spin coating, [130,131]	Small, substrate must be spun	Depends on porosity of semiconductor film	Variable, depends on semiconductor deposition step	Wide range possible	Atmospheric
Sputtering, [141, 142]	Limited by size of vacuum system	Wide range possible	1 – 2 hours	Wide range possible	High vacuum
Layer by layer deposition, [76, 192]	Limited by dipping / coating mechanism	Wide range possible, excellent control of composition	Depends on number of layers, around 15 minutes / layer	Wide range possible	Atmospheric

Table 4.1. Comparison of gold / semiconductor composite film deposition techniques.

The AACVD technique presented here is able to deposit coatings on larger substrates than some of the other techniques discussed in this section. In fact, if successfully adapted to online coating, as APCVD has been, then the substrate size becomes unlimited. Additionally, a wide range of gold loading is possible, and the technique, in its current form, is relatively fast, especially as no significant substrate preparation is required.

4.6 Conclusions

Gold has been incorporated into semiconductor films by combining [$HAuCl_4$] or preformed gold nanoparticles with transition metal carbonyl, alkoxide or aryloxide precursors. Composite films showed SPR absorption, this and XPS and XRD results confirmed the presence of nano-scale metallic gold particles and the semiconductor phase within the films. A shift in SPR absorption maximum occurred on incorporation of the particles within a matrix. This is due to the increase in refractive index of the surrounding medium, and correlates reasonably well with predictions from Mie theory.

Chapter 5: Conclusions

5.1 Summary of Results

In this thesis a new approach to the formation of gold nanoparticle and nanoparticle / semiconductor composite films has been developed. AACVD, a variant of CVD which requires soluble precursors rather than volatile ones, was used to deposit films from two new gold CVD precursors:

- Hydrogen tetrachloroaurate, [$HAuCl_4$], proved to be an excellent precursor to metallic gold, avoiding many of the difficulties encountered with previous gold CVD precursors, such as air-sensitivity and high cost. Surfactants can be used to regulate the growth of particles from [$HAuCl_4$] within the reactor.

- Pre-formed gold nanoparticles may appear to be the antithesis of a traditional CVD precursor, but it was shown that pre-formed gold nanoparticles can be transported in an aerosol generated ultrasonically and can therefore be deposited by AACVD.

Neither of these precursors could be deposited using conventional APCVD, but both show promise as routes to films with controlled nanostructures.

Gold films deposited from [$HAuCl_4$] alone, using substrate temperatures of 350 - 500°C, showed SPR absorption maxima ranging from 1000 – 600 nm. No unreacted precursor remained on the substrate, and neither was there any chlorine contamination, as determined by XPS. Films were composed of particles with a wide range of sizes and shapes, and of regions of apparent island growth morphology. At low precursor concentrations of [$HAuCl_4$], the deposition profile showed an exponential decrease in growth rate with distance along the substrate, possibly suggesting a diffusion limited reaction. Higher concentrations of [$HAuCl_4$] caused a change in deposition profile, caused by more extensive gas phase nucleation of metallic gold particles.

The optical and structural properties of the gold films were related. Across all films produced, the SPR absorption maxima showed an approximate correlation with the Au

[111] diffraction peak area, which in turn is related to the amount of gold at a particular point. In some cases the crystallite size also correlated very well with the SPR absorption maxima.

The inclusion of surfactants in the precursor solution along with [$HAuCl_4$] strongly affected the morphology of the deposited films. Quaternary ammonium bromide compounds were used, due to their previous successful use in solution phase gold particle synthesis. The result was films of gold nanoparticles, in most cases with very narrow size distributions, certainly comparable to the best current solution phase methods. The size of the particles was remarkably constant over the length of the each particular substrate. TOAB gave the particles with the narrowest size distributions. Changing the Au : TOAB ratio, substrate temperature and solvent volume altered the size of the particles deposited; spherical particles from 66 – 121 nm in diameter, with standard deviations less than 20% could be deposited by varying these parameters. CTAB offered some control over the shape of the particles, although significantly less so than in syntheses in solution phase. Films of elongated particles with aspect ratios up to 2.0 were deposited, although a significant number of spherical particles remained. Unlike solution methods, there is no way to purify the nanorods by removing the spheres from the film surface. TEAB produced particles with a variety of shapes, including relatively high aspect ratio nanorods.

Preformed gold particles were used to deposit a film of particles with similar size distribution and optical properties. This process is not strictly CVD, as no chemical change to the precursor occurs. These particles were smaller than those achieved with [$HAuCl_4$] + surfactant.

The new gold precursors were combined with conventional transition metal oxide precursors to produce nanocomposite films of gold within a semiconductor matrix. Using this single step methodology, gold particles were incorporated into TiO_2, MoO_3 and WO_3. These matrices were chosen because of their technological significance as photocatalysts or electrochromic materials. The gold content of the composite films could be varied by changing the gold concentration in the precursor solution. Incorporation of gold particles within the matrix caused a shift in the SPR maximum, which was interpreted in terms of Mie theory.

In the introduction of their 2006 review of metal / semiconductor nanocomposite coatings, Tondello *et al.* wrote:[101]

> "An open challenge in the field of nanotechnology is the development of versatile synthetic strategies to control the nucleation of the material building blocks and their subsequent assembly on the nanometric scale... As a matter of fact, tailoring of nucleation/growth processes is a key step to improve specific system characteristics, thus allowing the design of new and more efficient functional devices"

The methods presented in this thesis have combined facets of solution phase gold nanoparticle synthesis and CVD in an attempt meet this challenge. The versatility and usefulness of the AACVD technique has been demonstrated through the deposition of a variety of films with controllable nanostructure, and the facile combination of precursors to achieve composite films in a single step. CVD is already an industry standard technique, and the incorporation of AACVD into a production line, such as a glass float line, while not as easy as in the case of APCVD, should not prove impossible.

5.2 Future Perspectives

Further investigations into involatile CVD precursors designed specifically for AACVD may result in new methods for depositing films with useful properties. Other transition metals, Cu and Ag, show SPR absorption in the visible region. Deposition of these metals from involatile inorganic precursors might also be possible. Bimetallic particles might be deposited from a mixture of metal precursors. Other methodology used in solution phase nanoparticle synthesis might be attempted in a CVD setting, such as the use of seed particles to control particle growth. There are many other growth directing molecules, especially organic polymers, which might be included in a precursor solution. Finally, a very wide range of nanoparticles can be produced in solution, not only metal particles but semiconductors and organic polymers. Any of these might be deposited using AACVD analogously to the preformed gold particles deposited in this work. They might also be incorporated into composite films in a single step deposition.

References

1. F. Jansen and T. Kruck, *Advanced Materials*, 1995, **7**, 297-300.
2. S. Link and M. A. El-Sayed, *Journal of Physical Chemistry B*, 1999, **103**, 4212-4217.
3. A. T. Bell, *Science*, 2003, **299**, 1688-1691.
4. Y. W. C. Cao, R. C. Jin and C. A. Mirkin, *Science*, 2002, **297**, 1536-1540.
5. R. G. Freeman, K. C. Grabar, K. J. Allison, R. M. Bright, J. A. Davis, A. P. Guthrie, M. B. Hommer, M. A. Jackson, P. C. Smith, D. G. Walter and M. J. Natan, *Science*, 1995, **267**, 1629-1632.
6. R. Gordon, *Journal of Non-Crystalline Solids*, 1997, **218**, 81-91.
7. P. Moriarty, *Reports On Progress In Physics*, 2001, **64**, 297-381.
8. H. O. Pierson, Handbook of Chemical Vapour Deposition, Noyles Publishing, New York, 1992.
9. R. Y. Chein and W. Y. Liao, *Heat And Mass Transfer*, 2005, **42**, 71-79.
10. C. Housiadas and Y. Drossinos, *Aerosol Science And Technology*, 2005, **39**, 304-318.
11. C. J. Tsai, J. S. Lin, S. G. Aggarwal and D. R. Chen, *Aerosol Science And Technology*, 2004, **38**, 131-139.
12. M. C. Weinberg, *Journal of The American Ceramic Society*, 1983, **66**, 439-443.
13. W. Bai, K. L. Choy, N. H. J. Stelzer and J. Schoonman, *Solid State Ionics*, 1999, **116**, 225-228.
14. R. Piazza, *Journal of Physics-Condensed Matter*, 2004, **16**, S4195-S4211.
15. H. Ning, J. Buitenhuis, J. K. G. Dhont and S. Wiegand, *Journal of Chemical Physics*, 2006, **125**.
16. H. Ning, R. Kita, H. Kriegs, J. Luettmer-Strathmann and S. Wiegand, *Journal of Physical Chemistry B*, 2006, **110**, 10746-10756.
17. S. Duhr and D. Braun, *Proceedings of The National Academy of Sciences of The United States of America*, 2006, **103**, 19678-19682.
18. T. J. Krinke, K. Deppert, M. H. Magnusson, F. Schmidt and H. Fissan, *Journal of Aerosol Science*, 2002, **33**, 1341-1359.
19. R. H. Hurt and M. D. Allendorf, *Aiche Journal*, 1991, **37**, 1485-1496.

20. T. T. Kodas, E. M. Engler and V. Y. Lee, *Applied Physics Letters*, 1989, **54**, 1923-1925.
21. M. G. Nolan, M. E. Pemble, D. W. Sheel, H. M. Yates and H. M. Yates, *Thin Solid Films*, 2006, **515**, 1956-1962.
22. M. C. Barnes, D. Y. Kim, H. S. Ahn, C. O. Lee and N. M. Hwang, *Journal of Crystal Growth*, 2000, **213**, 83-92.
23. N. M. Hwang and D. Y. Kim, *International Materials Reviews*, 2004, **49**, 171-190.
24. U. Backman, A. Auvinen and J. K. Jokiniemi, *Surface & Coatings Technology*, 2005, **192**, 81-87.
25. S. Y. Lu, H. C. Lin and C. H. Lin, *Journal of Crystal Growth*, 1999, **200**, 527-542.
26. M. L. Hitchman and K. F. Jensen, Chemical Vapor Depositon: Principles and Applications, Academic Press, London, 1993.
27. P. Tandon and M. Murtagh, *Chemical Engineering Science*, 2005, **60**, 1685-1699.
28. G. Y. Zhao, J. J. Thiart, D. Orlicki and V. Hlavacek, *Chemical Engineering Science*, 1994, **49**, 4917-4938.
29. K. L. Choy, *Progress In Materials Science*, 2003, **48**, 57-170.
30. W. C. Hinds, Aerosol Technology, John Wiley & Sons, 1999.
31. S. M. Gates and S. K. Kulkarni, *Applied Physics Letters*, 1991, **58**, 2963-2965.
32. X. H. Hou and K. L. Choy, *Chemical Vapor Deposition*, 2006, **12**, 583-596.
33. R. J. Lang, *Journal of The Acoustical Society of America*, 1962, **34**, 6-&.
34. F. Barreras, H. Amaveda and A. Lozano, *Experiments In Fluids*, 2002, **33**, 405-413.
35. R. C. Weast, Handbook of Chemistry and Physics, Chemical Rubber Company, Cleveland, 1974.
36. F. E. Kruis, H. Fissan and A. Peled, *Journal of Aerosol Science*, 1998, **29**, 511-535.
37. A. Gurav, T. Kodas, T. Pluym and Y. Xiong, *Aerosol Science And Technology*, 1993, **19**, 411-452.
38. T. T. Kodas and M. Hampden-Smith, The Chemistry of Metal CVD, VCH, New York, 1994.
39. T. T. Kodas, *Angewandte Chemie-International Edition In English*, 1989, **28**, 794-806.

40. R. R. Chamberlin and J. S. Skarman, *Journal of The Electrochemical Society*, 1966, **113**, 86-&.

41. M. Langlet, *Thin Solid Films*, 2001, **398**, 71-77.

42. D. A. Edwards, R. M. Harker, M. F. Mahon and K. C. Molloy, *Journal of Materials Chemistry*, 1999, **9**, 1771-1780.

43. C. Y. Xu, M. J. Hampdensmith and T. T. Kodas, *Advanced Materials*, 1994, **6**, 746-748.

44. W. B. Cross, I. P. Parkin, S. A. O'Neill, P. A. Williams, M. F. Mahon and K. C. Molloy, *Chemistry of Materials*, 2003, **15**, 2786-2796.

45. M. C. Daniel and D. Astruc, *Chemical Reviews*, 2004, **104**, 293-346.

46. G. Schmid, R. Pfeil, R. Boese, F. Bandermann, S. Meyer, G. H. M. Calis and W. A. Vandervelden, *Chemische Berichte-Recueil*, 1981, **114**, 3634-3642.

47. U. Simon, G. Schon and G. Schmid, *Angewandte Chemie-International Edition In English*, 1993, **32**, 250-254.

48. C. N. R. Rao, G. U. Kulkarni, P. J. Thomas and P. P. Edwards, *Chemical Society Reviews*, 2000, **29**, 27-35.

49. W. Vogel, B. Rosner and B. Tesche, *Journal of Physical Chemistry*, 1993, **97**, 11611-11616.

50. L. M. Liz-Marzan, *Langmuir*, 2006, **22**, 32-41.

51. W. L. Barnes, A. Dereux and T. W. Ebbesen, *Nature*, 2003, **424**, 824-830.

52. R. H. Ritchie, *Physical Review*, 1957, **1**, 874-881.

53. S. Link and M. A. El-Sayed, *International Reviews In Physical Chemistry*, 2000, **19**, 409-453.

54. J. Rodriguez-Fernandez, J. Perez-Juste, F. J. G. de Abajo and L. M. Liz-Marzan, *Langmuir*, 2006, **22**, 7007-7010.

55. J. A. Creighton and D. G. Eadon, *Journal of The Chemical Society-Faraday Transactions*, 1991, **87**, 3881-3891.

56. T. Klar, M. Perner, S. Grosse, G. von Plessen, W. Spirkl and J. Feldmann, *Physical Review Letters*, 1998, **80**, 4249-4252.

57. K. R. Brown and M. J. Natan, *Langmuir*, 1998, **14**, 726-728.

58. S. L. Goodman, G. M. Hodges, L. K. Trejdosiewicz and D. C. Livingston, *Journal of Microscopy-Oxford*, 1981, **123**, 201-213.

59. K. Nakamura, T. Kawabata and Y. Mori, *Powder Technology*, 2003, **131**, 120-128.

60. S. Underwood and P. Mulvaney, *Langmuir*, 1994, **10**, 3427-3430.

61. P. Mulvaney, *Langmuir*, 1996, **12**, 788-800.

62. J. Perez-Juste, I. Pastoriza-Santos, L. M. Liz-Marzan and P. Mulvaney, *Coordination Chemistry Reviews*, 2005, **249**, 1870-1901.

63. J. Perez-Juste, M. A. Correa-Duarte and L. M. Liz-Marzan, *Applied Surface Science*, 2004, **226**, 137-143.

64. J. Perez-Juste, B. Rodriguez-Gonzalez, P. Mulvaney and L. M. Liz-Marzan, *Advanced Functional Materials*, 2005, **15**, 1065-1071.

65. J. Perez-Juste, L. M. Liz-Marzan, S. Carnie, D. Y. C. Chan and P. Mulvaney, *Advanced Functional Materials*, 2004, **14**, 571-579.

66. S. Link, M. B. Mohamed and M. A. El-Sayed, *Journal of Physical Chemistry B*, 1999, **103**, 3073-3077.

67. N. Irit, T. A. Bendikov, I. Doron-Mor, Z. Barkay, A. Vaskevich and I. Rubinstein, *Journal of The American Chemical Society*, 2007, **129**, 84-92.

68. Y. Luo, J. Ruff, R. Ray, Y. L. Gu, H. J. Ploehn and W. A. Scrivens, *Chemistry of Materials*, 2005, **17**, 5014-5023.

69. S. Norrman, T. Andersson, C. G. Granqvist and O. Hunderi, *Physical Review B*, 1978, **18**, 674-695.

70. S. Yamaguchi, *Journal of The Physical Society of Japan*, 1960, **15**, 1577-1585.

71. I. Doron-Mor, Z. Barkay, N. Filip-Granit, A. Vaskevich and I. Rubinstein, *Chemistry of Materials*, 2004, **16**, 3476-3483.

72. R. Gupta, M. J. Dyer and W. A. Weimer, *Journal of Applied Physics*, 2002, **92**, 5264-5271.

73. D. N. Jarrett and L. Ward, *Journal of Physics D-Applied Physics*, 1976, **9**, 1515-1527.

74. J. M. Gerardy and M. Ausloos, *Physical Review B*, 1982, **25**, 4204-4229.

75. H. Du, *Applied Optics*, 2004, **43**, 1951-1956.

76. T. Ung, L. M. Liz-Marzan and P. Mulvaney, *Colloids And Surfaces A-Physicochemical And Engineering Aspects*, 2002, **202**, 119-126.

77. N. R. Jana, L. Gearheart and C. J. Murphy, *Journal of Physical Chemistry B*, 2001, **105**, 4065-4067.

78. D. J. Barber and I. C. Freestone, *Archaeometry*, 1990, **32**, 33-45.

79. M. Faraday, *Philospohical Transactions of the Royal Society of London*, 1857, **147**, 145.

80. B. L. Cushing, V. L. Kolesnichenko and C. J. O'Connor, *Chemical Reviews*, 2004, **104**, 3893-3946.

81. J. Turkevich, P. C. Stevenson and J. Hillier, *Discussions of The Faraday Society*, 1951, 55-&.

82. M. Brust, M. Walker, D. Bethell, D. J. Schiffrin and R. Whyman, *Journal of The Chemical Society-Chemical Communications*, 1994, 801-802.

83. H. Bonnemann and R. M. Richards, *European Journal of Inorganic Chemistry*, 2001, 2455-2480.

84. Z. X. Wang, B. E. Tan, I. Hussain, N. Schaeffer, M. F. Wyatt, M. Brust and A. I. Cooper, *Langmuir*, 2007, **23**, 885-895.

85. M. C. Plante, J. Garrett, S. C. Ghosh, P. Kruse, H. Schriemer, T. Hall and R. R. LaPierre, *Applied Surface Science*, 2006, **253**, 2348-2354.

86. C. J. Kiely, J. Fink, M. Brust, D. Bethell and D. J. Schiffrin, *Nature*, 1998, **396**, 444-446.

87. R. Seshadri, G. N. Subbanna, V. Vijayakrishnan, G. U. Kulkarni, G. Ananthakrishna and C. N. R. Rao, *Journal of Physical Chemistry*, 1995, **99**, 5639-5644.

88. M. J. Hostetler, J. E. Wingate, C. J. Zhong, J. E. Harris, R. W. Vachet, M. R. Clark, J. D. Londono, S. J. Green, J. J. Stokes, G. D. Wignall, G. L. Glish, M. D. Porter, N. D. Evans and R. W. Murray, *Langmuir*, 1998, **14**, 17-30.

89. V. Privman, D. V. Goia, J. Park and E. Matijevic, *Journal of Colloid And Interface Science*, 1999, **213**, 36-45.

90. V. K. Lamer and R. H. Dinegar, *Journal of The American Chemical Society*, 1950, **72**, 4847-4854.

91. X. Y. Liu, *Journal of Chemical Physics*, 2000, **112**, 9949-9955.

92. J. Kimling, M. Maier, B. Okenve, V. Kotaidis, H. Ballot and A. Plech, *Journal of Physical Chemistry B*, 2006, **110**, 15700-15707.

93. G. Frens, *Nature-Physical Science*, 1973, **241**, 20-22.

94. I. Hussain, M. Brust, A. J. Papworth and A. I. Cooper, *Langmuir*, 2003, **19**, 4831-4835.

95. S. H. Chen and K. Kimura, *Langmuir*, 1999, **15**, 1075-1082.

96. N. R. Jana, L. Gearheart and C. J. Murphy, *Chemistry of Materials*, 2001, **13**, 2313-2322.

97. C. Note, S. Kosmella and J. Koetz, *Colloids And Surfaces A-Physicochemical And Engineering Aspects*, 2006, **290**, 150-156.

98. C. Note, J. Ruffin, B. Tiersch and J. Koetz, *Journal of Dispersion Science And Technology*, 2007, **28**, 155-164.

99. F. X. Chen, G. Q. Xu and T. S. A. Hor, *Materials Letters*, 2003, **57**, 3282-3286.

100. B. Mukherjee and N. Ravishankar, *Nanotechnology*, 2007, **18**.

101. L. Armelao, D. Barreca, G. Bottaro, A. Gasparotto, S. Gross, C. Maragno and E. Tondello, *Coordination Chemistry Reviews*, 2006, **250**, 1294-1314.

102. S. Jain, D. J. Skamser and T. T. Kodas, *Aerosol Science And Technology*, 1997, **27**, 575-590.

103. G. V. Jayanthi, S. C. Zhang and G. L. Messing, *Aerosol Science And Technology*, 1993, **19**, 478-490.

104. S. Hannemann, J. D. Grunwaldt, F. Krumeich, P. Kappen and A. Baiker, *Applied Surface Science*, 2006, **252**, 7862-7873.

105. N. Iida, H. Naito, H. Ito, K. Nakayama, I. W. Lenggoro and K. Okuyama, *Journal of The Ceramic Society of Japan*, 2004, **112**, 405-408.

106. F. Schulz, S. Franzka and G. Schmid, *Advanced Functional Materials*, 2002, **12**, 532-536.

107. S. Rauschenbach, F. L. Stadler, E. Lunedei, N. Malinowski, S. Koltsov, G. Costantini and K. Kern, *Small*, 2006, **2**, 540-547.

108. J. B. Fenn, M. Mann, C. K. Meng, S. F. Wong and C. M. Whitehouse, *Science*, 1989, **246**, 64-71.

109. I. W. Lenggoro, B. Xia, K. Okuyama and J. F. de la Mora, *Langmuir*, 2002, **18**, 4584-4591.

110. J. Therrien, A. Dindar and D. Smith, *Microscopy Research And Technique*, 2007, **70**, 530-533.

111. P. H. M. Bottger, Z. Bi, D. Adolph, K. A. Dick, L. S. Karlsson, M. N. A. Karlsson, B. A. Wacaser and K. Deppert, *Nanotechnology*, 2007, **18**.

112. I. W. Lenggoro, H. M. Lee and K. Okuyama, *Journal of Colloid And Interface Science*, 2006, **303**, 124-130.

113. D. Buso, J. Pacifico, A. Martucci and P. Mulvaney, *Advanced Functional Materials*, 2007, **17**, 347-354.

114. G. T. De and C. N. R. Rao, *Journal of Materials Chemistry*, 2005, **15**, 891-894.

115. V. Subramanian, E. E. Wolf and P. V. Kamat, *Journal of The American Chemical Society*, 2004, **126**, 4943-4950.

116. A. Orlov, D. A. Jefferson, M. Tikhov and R. M. Lambert, *Catalysis Communications*, 2007, **8**, 821-824.

117. V. Iliev, D. Tomova, L. Bilyarska and G. Tyuliev, *Journal of Molecular Catalysis A-Chemical*, 2007, **263**, 32-38.

118. V. Subramanian, E. Wolf and P. V. Kamat, *Journal of Physical Chemistry B*, 2001, **105**, 11439-11446.

119. T. He, Y. Ma, Y. Cao, W. S. Yang and J. N. Yao, *Journal of Electroanalytical Chemistry*, 2001, **514**, 129-132.

120. T. He, Y. Ma, Y. A. Cao, W. S. Yang and J. N. Yao, *Physical Chemistry Chemical Physics*, 2002, **4**, 1637-1639.

121. K. W. Park, *Electrochimica Acta*, 2005, **50**, 4690-4693.

122. T. He, Y. Ma, Y. Cao, Y. H. Yin, W. S. Yang and J. N. Yao, *Applied Surface Science*, 2001, **180**, 336-340.

123. T. He, Y. Ma, Y. A. Cao, P. Jiang, X. T. Zhang, W. S. Yang and J. N. Yao, *Langmuir*, 2001, **17**, 8024-8027.

124. T. He, Y. H. Yin, Y. Ma, P. Jiang, Y. A. Cao and J. N. Yao, *Chemical Journal of Chinese Universities*, 2001, **22**, 824-826.

125. J. N. Yao, Y. A. Yang and B. H. Loo, *Journal of Physical Chemistry B*, 1998, **102**, 1856-1860.

126. Y. Tian and T. Tatsuma, *Chemical Communications*, 2004, 1810-1811.

127. Z. X. Liu, H. H. Wang, H. Li and X. M. Wang, *Applied Physics Letters*, 1998, **72**, 1823-1825.

128. A. L. Stepanov and V. N. Popok, *Technical Physics Letters*, 2003, **29**, 977-979.

129. K. Fukumi, A. Chayahara, K. Kadono, T. Sakaguchi, Y. Horino, M. Miya, K. Fujii, J. Hayakawa and M. Satou, *Journal of Applied Physics*, 1994, **75**, 3075-3080.

130. K. Naoi, Y. Ohko and T. Tatsuma, *Journal of The American Chemical Society*, 2004, **126**, 3664-3668.

131. E. Stathatos and P. Lianos, *Langmuir*, 2000, **16**, 2398-2400.

132. Y. Hida and H. Kozuka, *Thin Solid Films*, 2005, **476**, 264-271.

133. Y. Yang, J. L. Shi, W. M. Huang, S. G. Dai and L. Wang, *Journal of Materials Science*, 2003, **38**, 1243-1248.

134. M. Epifani, C. Giannini, L. Tapfer and L. Vasanelli, *Journal of The American Ceramic Society*, 2000, **83**, 2385-2393.

135. E. Mine, A. Yamada, Y. Kobayashi, M. Konno and L. M. Liz-Marzan, *Journal of Colloid And Interface Science*, 2003, **264**, 385-390.

136. S. Sayen and A. Walcarius, *Electrochemistry Communications*, 2003, **5**, 341-348.

137. T. Ishizaka, S. Muto and Y. Kurokawa, *Optics Communications*, 2001, **190**, 385-389.

138. H. Yanagi, S. Mashiko, L. A. Nagahara and H. Tokumoto, *Chemistry of Materials*, 1998, **10**, 1258-1264.

139. X. H. Wang, H. L. Shi, S. G. Dai and Y. Yang, *Thin Solid Films*, 2003, **429**, 102-107.

140. S. Deki, Y. Aoi, H. Yanagimoto, K. Ishii, K. Akamatsu, M. Mizuhata and A. Kajinami, *Journal of Materials Chemistry*, 1996, **6**, 1879-1882.

141. W. Qian, L. Lin, Y. J. Deng, Z. J. Xia, Y. H. Zou and G. K. L. Wong, *Journal of Applied Physics*, 2000, **87**, 612-614.

142. H. B. Liao, R. F. Xiao, J. S. Fu, P. Yu, G. K. L. Wong and P. Sheng, *Applied Physics Letters*, 1997, **70**, 1-3.

143. E. Flahaut, F. Agnoli, J. Sloan, C. O'Connor and M. L. H. Green, *Chemistry of Materials*, 2002, **14**, 2553-2558.

144. D. Li, C. J. Choi, B. K. Kim and Z. D. Zhang, *Journal of Magnetism And Magnetic Materials*, 2004, **277**, 64-70.

145. W. T. Wang, L. S. Qu, G. Yang and Z. G. Chen, *Applied Surface Science*, 2003, **218**, 24-28.

146. R. H. W. Au and R. J. Puddephatt, *Chemical Vapor Deposition*, 2007, **13**, 20.

147. C. E. Larson, T. H. Baum and R. L. Jackson, *Journal of The Electrochemical Society*, 1987, **134**, 266-266.

148. M. Okumura, S. Nakamura, S. Tsubota, T. Nakamura, M. Azuma and M. Haruta, *Catalysis Letters*, 1998, **51**, 53-58.

149. T. H. Baum and C. R. Jones, *Applied Physics Letters*, 1985, **47**, 538-540.

150. Y. Morishige and S. Kishida, *Applied Physics A-Materials Science & Processing*, 1994, **59**, 395-399.

151. M. Okumura, S. Nakamura, S. Tsubota, T. Nakamura and M. Haruta, in *Preparation of Catalysts Vii*, 1998, **118**, 277-284.

152. P. B. Comita, P. E. Price and T. T. Kodas, *Applied Physics Letters*, 1990, **56**, 2693-2695.

153. N. H. Dryden, J. G. Shapter, L. L. Coatsworth, P. R. North and R. J. Puddephatt, *Chemistry of Materials*, 1992, **4**, 979-981.

154. M. M. B. Holl, P. F. Seidler, S. P. Kowalczyk and F. R. McFeely, *Inorganic Chemistry*, 1994, **33**, 510-517.

155. E. Szlyk, P. Piszczek, I. Lakomska, A. Grodzicki, J. Szatkowski and T. Blaszczyk, *Chemical Vapor Deposition*, 2000, **6**, 105-108.

156. T. H. Baum, *Journal of The Electrochemical Society*, 1987, **134**, 2616-2619.

157. E. Feurer and H. Suhr, *Applied Physics A-Materials Science & Processing*, 1987, **44**, 171-175.

158. X. Li, P. Goring, E. Pippel, M. Steinhart, D. H. Kim and W. Knoll, *Macromolecular Rapid Communications*, 2005, **26**, 1173-1178.

159. S. Jain, S. Gu, M. Hampden-Smith and T. T. Kodas, *Chemical Vapor Deposition*, 1998, **4**, 253-257.

160. D. Briggs and M. P. Seah, Practical Surface Analysis, Wiley, London, 1990.

161. G. Will, Powder Diffraction: The Rietveld Method and the Two-Stage Method, Springer, Berlin, 2006.

162. G. Hyett, M. Green and I. P. Parkin, *Journal of The American Chemical Society*, 2006, **128**, 12147-12155.

163. J. W. Yoon, T. Sasaki, N. Koshizaki and E. Traversa, *Scripta Materialia*, 2001, **44**, 1865-1868.

164. P. W. Atkins, Physical Chemistry, Oxford University Press, Oxford, 1986.

165. A. I. Maaroof, M. B. Cortie and G. B. Smith, *Journal of Optics A-Pure And Applied Optics*, 2005, **7**, 303-309.

166. K. Nakaso, M. Shimada, K. Okuyama and K. Deppert, *Journal of Aerosol Science*, 2002, **33**, 1061-1074.

167. I. Pastoriza-Santos, J. Perez-Juste and L. M. Liz-Marzan, *Chemistry of Materials*, 2006, **18**, 2465-2467.

168. S. W. Prescott and P. Mulvaney, *Journal of Applied Physics*, 2006, **99**.

169. R. S. Deinhammer, M. Ho, J. W. Anderegg and M. D. Porter, *Langmuir*, 1994, **10**, 1306-1313.

170. T. Sakai and P. Alexandridis, *Langmuir*, 2004, **20**, 8426-8430.

171. S. Chen, C. Guo, G. H. Hu, J. Wang, J. H. Ma, X. F. Liang, L. Zheng and H. Z. Liu, *Langmuir*, 2006, **22**, 9704-9711.

172. M. P. Pileni, *Advances In Colloid And Interface Science*, 1993, **46**, 139-163.

173. H. Song, D. L. Chen and R. F. Ismagilov, *Angewandte Chemie-International Edition*, 2006, **45**, 7336-7356.

174. T. C. Pluym, Q. H. Powell, A. S. Gurav, T. L. Ward, T. T. Kodas, L. M. Wang and H. D. Glicksman, *Journal of Aerosol Science*, 1993, **24**, 383-392.

175. G. L. Messing, S. C. Zhang and G. V. Jayanthi, *Journal of The American Ceramic Society*, 1993, **76**, 2707-2726.

176. K. H. Leong, *Journal of Aerosol Science*, 1987, **18**, 511-524.

177. K. H. Leong, *Journal of Aerosol Science*, 1987, **18**, 525.

178. M. Brust, D. Bethell, C. J. Kiely and D. J. Schiffrin, *Langmuir*, 1998, **14**, 5425-5429.

179. X. D. Xu, M. Stevens and M. B. Cortie, *Chemistry of Materials*, 2004, **16**, 2259-2266.

180. D. I. Gittins, A. S. Susha, B. Schoeler and F. Caruso, *Advanced Materials*, 2002, **14**, 508.

181. A. Rampaul, I. P. Parkin, S. A. O'Neill, J. DeSouza, A. Mills and N. Elliott, *Polyhedron*, 2003, **22**, 35-44.

182. H. Saitoh, H. Sunayama, N. Tanaka and S. Ohshio, *Journal of The Ceramic Society of Japan*, 1998, **106**, 1051-1055.

183. D. C. Gilmer, D. G. Colombo, C. J. Taylor, J. Roberts, G. Haugstad, S. A. Campbell, H. S. Kim, G. D. Wilk, M. Gribelyuk and W. L. Gladfelter, *Chemical Vapor Deposition*, 1998, **4**, 9-11.

184. N. Tanaka, S. Ohshio and H. Saitoh, *Journal of The Ceramic Society of Japan*, 1997, **105**, 551-554.

185. O. Bohnke, C. Bohnke, A. Donnadieu and D. Davazoglou, *Journal of Applied Electrochemistry*, 1988, **18**, 447-453.

186. R. U. Kirss and L. Meda, *Applied Organometallic Chemistry*, 1998, **12**, 155-160.

187. D. Gogova, K. Gesheva, A. Szekeres and M. Sendova-Vassileva, *Physica Status Solidi A-Applied Research*, 1999, **176**, 969-984.

188. K. A. Gesheva, T. Ivanova, G. Popkirov and F. Hamelmann, *Journal of Optoelectronics And Advanced Materials*, 2005, **7**, 169-175.

189. T. Ivanova, M. Surtchev and K. Gesheva, *Materials Letters*, 2002, **53**, 250-257.

190. F. A. Cotton and G. W. Wilkinson, Advanced Inorganic Chemistry, Wiley, New York, 1980.

191. A. Mills, G. Hill, S. Bhopal, I. P. Parkin and S. A. O'Neill, *Journal of Photochemistry And Photobiology A-Chemistry*, 2003, **160**, 185-194.

192. T. Ung, L. M. Liz-Marzan and P. Mulvaney, *Journal of Physical Chemistry B*, 2001, **105**, 3441-3452.

193. A. Chemseddine and T. Moritz, *European Journal of Inorganic Chemistry*, 1999, 235-245.

194. M. C. Bourg, A. Badia and R. B. Lennox, *Journal of Physical Chemistry B*, 2000, **104**, 6562-6567.

195. A. Zwijnenburg, A. Goossens, W. G. Sloof, M. W. J. Craje, A. M. van der Kraan, L. J. de Jongh, M. Makkee and J. A. Moulijn, *Journal of Physical Chemistry B*, 2002, **106**, 9853-9862.

196. Y. J. Liu, A. B. Wang and R. Claus, *Journal of Physical Chemistry B*, 1997, **101**, 1385-1388.

197. A. Pashutski and M. Folman, *Surface Science*, 1989, **216**, 395-408.

198. M. Lee, L. Chae and K. C. Lee, *Nanostructured Materials*, 1999, **11**, 195-201.

199. K. Juodkazis, J. Juodkazyte, V. Jasulaitiene, A. Lukinskas and B. Sebeka, *Electrochemistry Communications*, 2000, **2**, 503-507.

200. C. J. Powell, A. Jablonski, A. Naumkin, A. Kraut-Vass, J. M. Conny and J. R. Rumble, *Journal of Electron Spectroscopy And Related Phenomena*, 2001, **114**, 1097-1102.

201. S. O'Neill, I. P. Parkin, R. J. H. Clark, A. Mills and N. Elliott, *Chemical Vapor Deposition*, 2004, **10**, 136.

202. D. Davazoglou, G. Leveque and A. Donnadieu, *Solar Energy Materials*, 1988, **17**, 379-390.

203. C. S. Blackman and I. P. Parkin, *Chemistry of Materials*, 2005, **17**, 1583-1590.

204. T. H. Fleisch and G. J. Mains, *Journal of Chemical Physics*, 1982, **76**, 780-786.

205. X. Z. Li and F. B. Li, *Environmental Science & Technology*, 2001, **35**, 2381-2387.

206. D. Gogova, A. Iossifova, T. Ivanova, Z. Dimitrova and K. Gesheva, *Journal of Crystal Growth*, 1999, **199**, 1230-1234.

207. A. Abdellaoui, G. Leveque, A. Donnadieu, A. Bath and B. Bouchikhi, *Thin Solid Films*, 1997, **304**, 39-44.

208. I. Antes, S. Dapprich, G. Frenking and P. Schwerdtfeger, *Inorganic Chemistry*, 1996, **35**, 2089-2096.

209. A. R. West, Solid State Chemistry and its Applications, Wiley, New York, 1984.

210. P. B. Johnson and R. W. Christy, *Physical Review B*, 1972, **6**, 4370-4379.

211. Z. Hussain, *Journal of Electronic Materials*, 2002, **31**, 615-630.

212. Z. Hussain, *Journal of Materials Research*, 2001, **16**, 2695-2708.

213. Z. Hussain, *Applied Optics*, 1999, **38**, 7112-7127.

214. M. A. Garcia, J. Llopis and S. E. Paje, *Chemical Physics Letters*, 1999, **315**, 313-320.